UNIVERSITY OF CALIFORNIA SAN DIEGO

Ultrafast Nonlinear Vibrational Microscopy and Applications in Study of Self-Assembled Materials

A dissertation submitted in partial satisfaction of the requirements for the degree

Doctor of Philosophy

in

Chemistry

by

Haoyuan Wang

Committee in charge:

Professor Wei Xiong, Chair

Professor Robert Continetti

Professor David Kleinfeld

Professor Zhaowei Liu

Professor Jeffrey Rinehart

Professor Mark Thiemens

2021

This dissertation of Haoyuan Wang is approved, and it is acceptable in quality and form for publication on microfilm and electronically:

University of California San Diego

2021

TABLE OF CONTENTS

LIST OF FIGURES

LIST OF TABLES

ACKNOWLEDGEMENTS

First, I would like to acknowledge Professor Wei Xiong for his guidance and support as my advisor and committee chair. I could not finish the work and achieve so much without him. I would also like to thank all my lab-mates for their kind help, both inside and outside the lab. Special thanks to all the coauthors, including Jackson Wagner, Wenfan Chen, Chenglai Wang, Tian Gao and Wei Xiong.

Chapter 1 and 2, in part, are reprints of the material as it appears in Annual Review of Physical Chemistry, 2021. Haoyuan Wang; Wei Xiong. Annual Reviews, 2021. The dissertation author was the primary investigator and author of this paper.

Chapter 3, in full, is a reprint of the material as it appears in ACS Photonics, 2017. Haoyuan Wang; Tian Gao; Wei Xiong. American Chemistry Society, 2017. The dissertation author was the primary investigator and author of this paper.

Chapter 4, in full, is a reprint of the material as it appears in The Journal of Physical Chemistry B, 2019. Haoyuan Wang; Wenfan Chen; Jackson Wagner; Wei Xiong. American Chemistry Society, 2019. The dissertation author was the primary investigator and author of this paper.

Chapter 5, in full, is a reprint of the material as it appears in Proceedings of the National Academy of Sciences of the United States of America, 2020. Haoyuan Wang; Jackson Wagner; Wenfan Chen; Chenglai Wang; Wei Xiong. United States National Academy of Sciences, 2020. The dissertation author was the primary investigator and author of this paper.

Chapter 6, in full, is still under development. The dissertation author was one of the primary investigators.

VITA

2015	B. S. in Chemistry with minor in Physics, Peking University, China
2015-2016	Graduate Teaching Assistant, University of California San Diego
2017	M. S. in Chemistry, University of California San Diego
2017-2021	Graduate Research Assistant, University of California San Diego
2021	Ph. D. in Chemistry, University of California San Diego

PUBLICATIONS

H. Wang, T. Gao, W. Xiong; "Self-Phase-Stabilized Heterodyne Vibrational Sum Frequency Generation Microscopy", *ACS Photonics*, 4, pp 1839-1845, 2017.

H. Wang, W. Chen, J. Wagner, W. Xiong; "Local Ordering of Lattice Self-Assembled SDS@2β-CD Materials and Adsorbed Water Revealed by Vibrational Sum Frequency Generation Microscope", *The Journal of Physical Chemistry B*, 123, pp 6212-6221, 2019.

H. Wang, J. Wagner, W. Chen, C. Wang, W. Xiong; "Spatially Dependent H-bond Dynamics at Interfaces of Water/biomimetic Self-Assembled Lattice Materials", *Proceedings of the National Academy of Science*, 117, pp 23385-23392, 2020.

H. Wang, W. Xiong; "Vibrational Sum-Frequency Generation Hyperspectral Microscopy for Molecular Self-Assembled Systems", *Annual Review of Physical Chemistry*, 72, pp 279-306, 2021.

ABSTRACT OF THE DISSERTATION

Ultrafast Nonlinear Vibrational Microscopy and Applications in Study of Self-Assembled Materials

by

Haoyuan Wang

Doctor of Philosophy in Chemistry

University of California San Diego, 2021

Professor Wei Xiong, Chair

Vibrational sum frequency generation (VSFG) microscopy is a powerful technique to study molecular vibrational modes at non-centrosymmetric surfaces, interfaces and structures. However, most of the existing VSFG microscopes have 2 limitations: lack of molecular orientation information and lack of ultrafast dynamics information. In this thesis, we report the newly developed VSFG microscopy in our lab, as well as their applications in the study of self-assembly.

First, we developed the self-phase-stabilized heterodyne-detected VSFG microscope that can reveal spectral phase and molecular orientations. In our geometry, the VSFG signal and local oscillator are generated using the same beam path. Therefore, comparing to traditional Michelson interferometric geometry, our phase stability is improved by 9 times. Using this heterodyne VSFG microscope to study a self-assembled material SDS@2β-CD, we successfully identified two molecular domains with different

molecular orientations, which is not possible to extract from an ensemble-averaged VSFG spectrum or homodyne-detected VSFG images.

In addition, we extended the spectral coverage and further studied the self-assembled material. We found because of strong hydrogen-bond interactions between water and the self-assembly, water molecules are template to adopt the local mesoscopic ordering of the self-assembly, which allows VSFG to probe water on non-flat interfaces. We also showed that the origin of the VSFG signal from the self-assembly is the result of combination between individual molecular chirality and highly coordinated ordering, which gives rise of anisotropy. Furthermore, we found heterogeneity among different domains, which can be attributed to variations in the local hydration level. Since the SDS@2β-CD system is a synthetic lattice self-assembly, such heterogeneity could also exist in other natural lattice self-assemblies such as virus and tubulin.

We further developed the first infrared pump, VSFG probe microscope and applied it to study the ultrafast dynamics in the self-assembly. We found that the primary and secondary OH of β-CD exhibit markedly different dynamics, suggesting distinct hydrogen bond environments, despite being separated by only a few angstroms. Another ultrafast dynamic is assigned to weakening and restoration of hydrogen bond between strongly bound water and secondary OH of β-CD, which exhibit spatial uniformity within self-assembled domains but heterogeneity between domains. The ultrafast nature and meso- and microscopic ordering of hydrogen bond dynamics could contribute to the flexibility and crystallinity of the material- two critically important factors for crystalline lattice self-assemblies, shedding light on engineering intermolecular interactions for self-assembled lattice materials.

Chapter 1

Introduction

Molecular self-assembling activities are ubiquitous in nature and are central to chemistry (1–3), biology (4, 5), and materials science (6, 7). Small particles, such as atoms, ions, and molecules, spontaneously aggregate and congregate into structurally well-defined and ordered architectures, such as J-aggregates (8), self-assembled monolayers (2, 9), membranes (10), and vesicles (11). These architectures further assemble into higher-order structures that are essential for life, such as living cells (4, 11) and light harvesting centers (12), or energy applications, such as photovoltaics (13) and solar fuels (14). Thus, understanding molecular self-assemblies and being able to control them is crucial for advancing our knowledge of and developing innovations in the chemical, materials, and life sciences. Important scientific properties of self-assembled systems include their structures, e.g., molecular orientation (15–17), intermolecular distances (18), and mesoscopic morphology (19, 20), as well as the physical and chemical self-assembling driving forces (21, 22) between molecules at interfaces.

Despite their importance, the challenges of studying self-assembled systems lie in how to selectively probe them in surroundings that are often disordered. The first scenario is molecules at metal or semiconductor surfaces that form self-assembled monolayers (SAMs) (2, 9, 17, 23–31), on which the molecules experience distinct environments and have different properties than do bulk molecules (32–34).

Because the number of surface molecules is much smaller than the number of bulk molecules, their signals are overwhelmed by the bulk response in techniques such as Fourier transform infrared and Raman spectroscopy. The second scenario is the investigation of self-assembled structures, which usually contain well-ordered parts and disordered parts with similar components. For example, when studying cellulose in plants (18, 35–38), it could be difficult to distinguish the signals from hemicellulose, which has very similar composition with cellulose but has random structure. Another example is strongly bound water in self-assembling, which is highly ordered. The signal could be overwhelmed by signal from random oriented water (39).

To collect this type of information, there are several surface/interface specific techniques to consider (40, 41). Electronic state-based techniques, such as X-ray photoelectron spectroscopy (XPS), ultraviolet photoelectron spectroscopy (UPS) and Auger electron spectroscopy (AES) are commonly used and can give element specific information at the sufaces/interfaces. However, these techniques do not include much molecular information and do not have spatially specific information. Photoemission electron microscopy (PEEM) can provide spatial information; however, the technique requires ultra-high vacuum system, which limits the application.

Secondary ion mass spectrometry (SIMS) is another surface specific technique that gives molecular information. However, the spatial information is still lacking for this technique. Scanning tunneling microscopy (STM) has excellent spatial resolution, but the molecular information is limited.

As for atomic force microscopy (AFM), traditional AFM does not offer molecular information. AFM-IR can provide some surface specific molecular information with spatial resolution, however, AFM and all the techniques mentioned above, as well as other linear optical techniques such as reflection-

absorption IR spectroscopy (RAIRS), cannot resolve the second scenario, in which well-ordered and disordered molecules needs to be distinguished. The reason is that these surface/interface techniques are based on the penetration depth, which only applies for the first scenario.

Fortunately, the sum-frequency generation (SFG) imaging technique overcomes these challenges (32, 42–45). SFG is a surface/interface technique due to its selection rule but not penetration depth. Based on the unique selection rule, only molecules or structures with noncentrosymmetry are SFG-active. This includes molecular configurations at surfaces/interfaces and noncentrosymmetric materials. By adding imaging capability to SFG can bring spatial visualization of the noncentrosymmetric materials. The theory of SFG will be discussed in Chapter 2.

SFG was developed by Shen and co-authors in 1987 (46, 47). The first VSFG microscope was demonstrated with the wide-field illumination geometry by Florsheimer et al. in 1999 (48). After that, Kuhnke et al. and Baldelli et al. further advanced the designs (49–51). The wide-field illumination microscope (Fig. 1.1 A) arranges an IR and an upconversion pulse to spatially and temporally overlapped onto the samples. The IR beam excites molecular vibrational resonances and the upconversion pulse converts the vibrational coherences into a higher frequency polarization which subsequently generate a free-induction decay signal at the sum of the two incoming beams' frequency, and therefore is named sum frequency generation. The VSFG signals are second-order nonlinear signal, and only exist in noncentrosymmetric systems, as explained more in section 3, ideal to probe interfaces and self-assembled materials with no inversion centers. The VSFG signal is distortion-corrected by a grating and projected onto the CCD detector (49). Because the 2D images occupy the CCD, it is necessary to scan the 1D spectral information. The most straightforward way is to scan the frequency of a narrow-band IR beam (17, 27, 28,

49, 50, 52–55), which works best for measurements that only need sparse data points in the frequency domain.

The confocal point-scanning geometry uses the IR and the upconversion beams that are aligned collinear onto the sample (15, 16, 56–58). A spectrograph measures the VSFG signals of each illuminated spot, and the samples are rastered in the 2D spatial dimension to acquire the images. A crucial optical component is the reflective Schwarzschild objective, which removes optical aberrations due to the refractive index mismatch between various wavelengths of lights.

While the point-scanning geometry is relatively slow in data acquisition, its optical arrangement is similar to ensemble-averaged VSFG spectroscopy, making it easy to adopt developments in VSFG spectroscopy. One of these developments is heterodyne detection (HD) to resolve VSFG phase that reveals orientation or chirality of the molecules (15, 16). HD-VSFGM has been demonstrated in both Michelson interferometric geometry and collinear geometry. Yang et al. showed that Michelson interferometric geometry allows arbitrary control of the time delay between the LO and the VSFG signal (16). Wang et al. developed a fully collinear HD-VSFG microscope (Fig. 1.1 B): a CaF2 window was used to generate a time delay among the VSFG signal, upconversion, and mid-IR pulses, which were focused on a nonlinear crystal (e.g., LiNbO3) to generate a LO. LO was spatially collinearly overlapped but was delayed temporally relative to the VSFG signal. Because all beams traveled the same path, it maximized the phase stability, and the phase was insensitive to sample height change (Fig. 1.1 B) (15).

Another example of combining techniques developed in VSFG spectroscopy with VSFGM is the first mid-IR pump VSFG probe hyperspectral microscope (Fig. 1.1 B). Wang et al. focused a mid-IR pump pulse to excite vibrational modes of the samples from off-axis and used the VSFGM to probe the transient

change induced at certain time delays (39). The pump-probe was measured in a quasi-shot-to-shot fashion by placing a chopper on the pump beam and a synchronized galvo-mirror on the VSFG probe beam, which displaced the VSFG spectra vertically to separate the signals being pumped from the rest. This setup allowed full hyperspectral imaging in spatial, temporal, and spectral domains to further characterize the heterogeneity of systems of interests.

Chapter 1, in part, is a reprint of the material as it appears in Annual Review of Physical Chemistry, 2021. Haoyuan Wang; Wei Xiong. Annual Reviews, 2021. The dissertation author was the primary investigator and author of this paper.

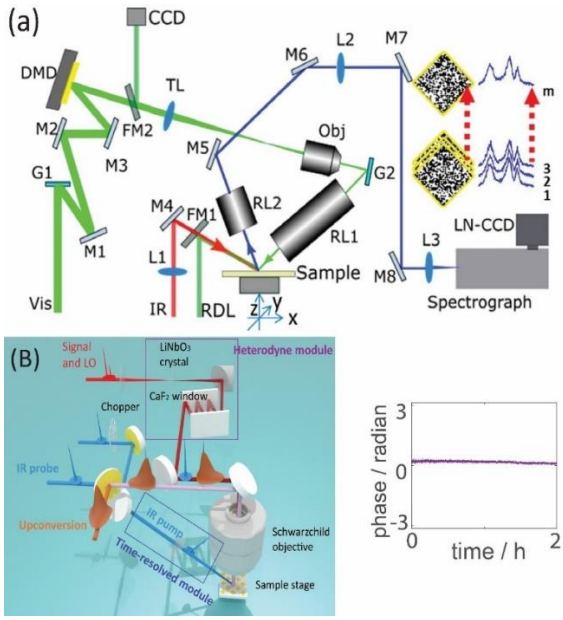

Figure 1.1. Experimental setups of VSFGM. (A) A broadband VSFGM combined with compressive sensing. A digital micromirror device (DMD) is used to generate randomly structured illumination patterns, and a compressive sensing algorithm reconstructs the spectra information. The blazed grating (G1) in the upconversion beam path is used to improve the signal-to-noise ratio. (B) Confocal point-scanning VSFGM. IR probe and upconversion beam are recombined by a dichroic optic and aligned collinearly. A Schwarzschild objective focuses them onto the sample. The emitted VSFG signal along with the residual IR probe and upconversion pulses are all collected by the objective and sent into the heterodyne module to generate a local oscillator (LO). The LO and signal are further sent to the spectrograph and CCD detector. An IR pump pulse in the time-resolved module is added to perform transient VSFGM.

Chapter 2

Theory and Experimentation

VSFG, pioneered by Shen and co-workers in 1987 (46, 47), is a second order coherent optical process, which can only be generated by non-centrosymmetric symmetry systems. The detailed theory of VSFG can be found in the literature (32, 42–45, 59, 60). Briefly, the electric field of VSFG signal $E_i^{(2)}(\omega)$ is driven by the second-order polarization $P^{(2)}$,

$$E_i^{(2)}(\omega) = P_i^{(2)} \propto \chi_{ijk}^{(2)} E_j(\omega;\omega_k) \otimes E_k(\omega;\omega_k) \quad \text{Eq. 1.}$$

Where $\chi_{ijk}^{(2)}$ is the second-order nonlinear susceptibility, and the subscripts denote the coordination axis; $E(\omega)$ is the input laser electromagnetic field, with $E_k(\omega;\omega_k)$ being an infrared (IR) laser that is on resonant with molecular vibrational modes, $E_j(\omega;\omega_j)$ being an upconversion beam that promotes the vibrational coherence into virtual states, and $\otimes$ represents convolution.

The symmetry selectivity of VSFG can be shown in the following way: under electric dipole approximation, applying an inversion operation to a centrosymmetric system makes $\chi_{-i-j-k}^{(2)} = -\chi_{ijk}^{(2)}$. However, for any centrosymmetric system, its property after inversion should remain unchanged, e.g., $\chi_{-i-j-k}^{(2)} = \chi_{ijk}^{(2)}$. Thus, $\chi_{ijk}^{(2)} = -\chi_{ijk}^{(2)} = 0$, which means only non-centrosymmetric systems, such as surfaces, interfaces, and any structures without inversion centers, can generate VSFG signals. For surface and interfaces, their symmetry breaks at the boundary between two phases. Most surface and interfaces

assume a $C_{\infty v}$ symmetry, with the surface normal as the symmetry axis. Thus, there are a total of 7 non-zero VSFG $\chi^{(2)}$ for $C_{\infty v}$ symmetry: $\chi^{(2)}_{xxz} = \chi^{(2)}_{yyz}$, $\chi^{(2)}_{xzx} = \chi^{(2)}_{yzy} = \chi^{(2)}_{zxx} = \chi^{(2)}_{zyy}$, $\chi^{(2)}_{zzz}$.

Another set of systems that can be selectively measured by VSFG but have received less attention are non-centrosymmetric self-assembled systems. Many self-assembled systems do not have inversion symmetry, e.g., Type I collagen (16, 61), cellulose (35, 62), and certain metal-organic-frameworks (MOFs) (63, 64). Unlike surface or interfaces, the symmetry of self-assembled materials is structure-dependent, which governs the non-zero $\chi^{(2)}$. For example, collagen fibers have cylindrical symmetry C_{∞}, and therefore collagen fiber lying at the interface has non-zero tensor elements: $\chi^{(2)}_{yyy}$, $\chi^{(2)}_{yzz} = \chi^{(2)}_{yxx} = \chi^{(2)}_{zyz} = \chi^{(2)}_{xyx}$, $\chi^{(2)}_{zzy} = \chi^{(2)}_{xxy}$, $\chi^{(2)}_{xyz} = \chi^{(2)}_{yxz} = -\chi^{(2)}_{yzx} = -\chi^{(2)}_{zyx}$, with the y axis defined as being in the collagen fiber longitudinal direction. (61)

2.1 Transformation between molecular and lab frames

The lab frame second-order nonlinear susceptibilities $\chi^{(2)}$ are further related to the molecular hyperpolarizability $\beta^{(2)}$ by Euler rotations (43, 65).

$$\chi^{(2)}_{ijk} = N < R_{ii'} R_{jj'} R_{kk'} > \beta^{(2)}_{i'j'k'} \quad \text{Eq. 2}$$

where $\beta^{(2)}_{i'j'k'}$ can be estimated by calculation or linear spectroscopy, R is the rotational matrix, N is the total number of molecules and <…> represents integrations overall angular coordinates that are isotropic. For a complete list of symmetry-allowed $\chi^{(2)}$ and $\beta^{(2)}$, we refer the reader to the work by Moad and Simpson (66), and the work by Hirose, Akamatsu, and Domen (65). This relationship is the key to obtaining an ensemble-averaged molecular orientation on surfaces or interfaces. However, it assumes a delta angular distribution. To quantify both mean orientation and then orientational distributions, one needs to measure

higher-order VSFG signals (67).

2.2 Polarization and surface symmetry of SFG process

For a surface/interface, if it does not have any symmetry, i.e., it is C_1 symmetry, there would be 27 non-zero terms for second-order susceptibilities. If it has certain symmetry, some of the second-order susceptibilities must be zero. For example, if the surface/interface has mirror plane or rotation symmetry, the XXX or YYY components would be 0. Nevertheless, if there is any XXX or YYY polarization SFG signal, it indicates the surface/interface has no symmetry.

When doing the experiment, the polarization of light is defined as P or S. If the light has an electric field polarized parallel to the plane of incidence, it is called P-polarized; while if the light has an electric field perpendicular to the plane of incidence, it is called S-polarized. If the incident light is P polarized, it contains both Y and Z components for the surface. While S polarization only contains X component. Therefore, if there is SSS polarization SFG signal, it indicates the surface/interface has no symmetry.

2.3 Homodyne versus heterodyne detections

The classical detection scheme is homodyne detection, which measures the intensity of the signal fields as follows:

$$I_{homo}(\omega) = |E_i^{(2)}(\omega)|^2 \qquad \text{Eq. 3}$$

A recent development is heterodyne detection (HD), which mixes the signal with a reference beam with a known phase (23, 24, 31, 32, 45, 68–74). In this case, the measured heterodyne signals are

$$I_{hetero}(\omega) = |E_i^{(2)}(\omega) + \mathrm{LO}|^2 = \left|E_i^{(2)}(\omega)\right|^2 + 2\mathcal{R}\left[E_i^{(2)}(\omega) \cdot \mathrm{LO}\right] + |\mathrm{LO}|^2 \qquad \text{Eq. 4}$$

LO is the local oscillator. By applying Fourier filters, the cross-term (red term of Eq. 4) can be extracted, which reveals the phase of the VSFG signal.

2.4 Transient VSFG

In Time-resolved VSFG experiments, the sample is vibrationally excited by irradiation of the IR pump pulse (75, 76). After a time delay (Δt), the change of VSFG signal is measured. In a time-resolved experiment, one would expect to see at least ground state bleach (GSB) and excited state absorption (ESA). However, in homodyne detected VSFG experiment, the ESA is usually not detectable since it is too small due to the nature of homodyne detection. For example, if 10% of vibrational modes are excited to 1st excited state (which is a fair assumption), in homodyne detection the ESA VSFG signal is about 2*10%*10% = 2% of the original signal and would easily be overwhelmed by the noise level. (76)

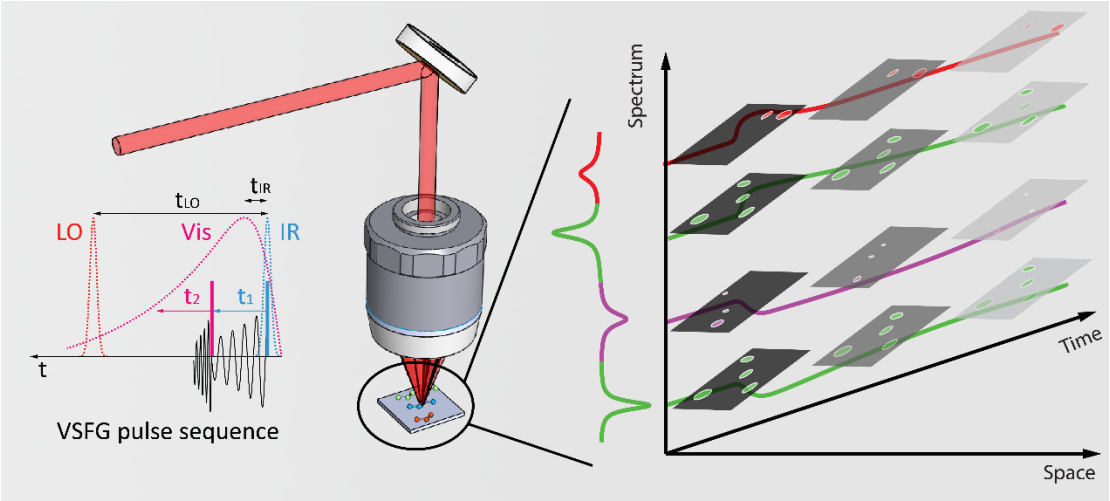

Figure 2.1. Schematic of VSFG hyperspectral microscopy and how hyper-dimensional information (e.g., frequency, spatial and temporal) can be disentangled in complex systems. Left: pulse sequence of VSFG. The IR pulse excites vibrational coherences on the molecular systems, which oscillate during t_1 and are upconverted by the visible pulse at t_2 to a higher frequency polarization and subsequent emit the signal. The signal is heterodyne detected by the local oscillator (LO). Middle: A cartoon of VSFG microscope setup. Right: time-dependent hyperspectral image from VSFGM. The different colors in the spectrum represent the peak from different molecular compound, while the signs of the peaks represent the phases measured by heterodyne-detection. The colored domains in the parallelogram map represent the spatial distribution of corresponding peaks, while their changes in time axis represent the dynamic of each spectral feature.

2.5 Relationship Between Spectroscopy, Microscopy, and Hyperspectral Imaging

Many self-assembled systems are heterogenous in spatial, temporal, and chemical spaces. While VSFG can, to some level, distinguish different chemical species by probing their vibrational fingerprints, it integrates all other dimensions and only displays the spectral information on one frequency dimension. For complex chemical systems, knowledge in the spatial and temporal dimensions can be vital molecular-level insights and useful to selectively probe the systems.

To see this, we consider the measured signals of a system X_N that is composed of a collection of N molecular absorber or emitters M_i,

$$X_N\{M_1(\omega, r, t; R_1, \omega_1, A_1, \Gamma_1), M_2(\omega, r, t; R_2, \omega_2, A_2, \Gamma_2), \dots, M_N(\omega, r, t; R_N, \omega_N, A_N, \Gamma_N)\}$$

Eq. 5a

with

$$M_i(\omega, r, t; R_i, \omega_i, A_i, \Gamma_i) = (\sum_a L_{i,a}(\omega, t)) \cdot \delta(r - R_i(t)) = (\sum_a \frac{A_{i,a}(t)}{(\omega - \omega_{i,a}(t)) + i \cdot \Gamma_{i,a}(t)}) \cdot \delta(r - R_i(t))$$

Eq. 5b,

where $\delta(r - R_i(t))$ is the spatial distribution function of molecule *i* at a specific time t, with R_i being the center positions of the molecules, and $L_{i,a}$ represents the spectral feature *a* of molecule i, with $A_{i,a}$, $\omega_{i,a}$, $\Gamma_{i,a}$ being the amplitude, center frequency and linewidth of the specific spectral feature. The summation in the front includes all degrees of freedom (electronic, vibrational, and rotational) of molecules. The temporal dependence is included implicitly, because $A_{i,a}$, $\omega_{i,a}$, $\Gamma_{i,a}$ and R_i are functions of time.

An ultimate measurement should determine the spectral features of every molecule as functions of time and space. However, such a task is not only daunting, but also unnecessary. In principle, it is sufficient to measure each sub-ensemble, within which the molecules behave the same but among which the molecules could have different properties. A bottom-up approach to achieve this goal is single-molecule imaging (77–79): Single molecular emitters M_i are measured, and a collection of measurements reveals the statistics of the systems. The challenge is that single-molecule microscopy is primarily fluorescence-based, and only specific fluorophores are strong enough emitters for single-molecule detection and not all degrees of freedom of molecular motions are reflected by fluorescence.

A top-down approach is to measure the molecular system with all irrelevant dimensions fully

integrated and to record the molecular properties with only the relevant dimensions.

2.5.1 Ensembled spectroscopy

For example, for a static and spatially homogeneous system, both temporal and spatial domains become irrelevant. By fully integrating the spatial (r) and temporal (t) coordinates of $M_i(\omega, r, t;\ R_i, \omega_i, A_i, \Gamma_i)$, it results in the spectra of molecule i, $\sum_a\ L_{i,a}(\omega; \overline{\omega_{\iota,a}}, \overline{A_{\iota,a}}, \overline{\Gamma_{\iota,a}})$, and ensemble averaging all molecules leads to the classical spectroscopy (S):

$S = \sum_i \sum_a\ L_{i,a}(\omega; \overline{\omega_{\iota,a}}, \overline{A_{\iota,a}}, \overline{\Gamma_{\iota,a}})$ Eq.6

In this way, spectra of molecules in a homogeneous system can be measured with no information on their spatial location or temporal dynamics.

2.5.2 Intensity-based microscopy

More information can be learned when fewer dimensions are integrated. For example, any intensity-based microscopy integrates the spectral coordinates, making $M_i(\omega, r, t;\ R_i, \omega_i, A_i, \Gamma_i) = M_i(r, t; R_i, A_i) \propto \sum_a A_{i,a}(t) \cdot \delta(r - R_i(t))$, and, therefore, the measurement is an image (I) composed of time-dependent spatial point-spread functions (77–87):

$I = \sum_i \sum_a A_{i,a}(t) \cdot \delta(r - R_i(t))$ Eq. 7

The images contain only spatial-dependent intensity information and convolute molecular structures, conformations, and local environments together. The time dependence of R and $A_{i,a}$ means the microscopies are time-resolved. The time resolution is set by Δt, the time duration for capturing one image. If Δt is significantly longer than the time scale of motion of interests, then the microscopy measures the static

images. Typically, millisecond to second dynamics, such as rheology, can be time-resolved by the frame rate of the microscope; picosecond or femtosecond ultrafast dynamics, such as energy and charge transfers in molecules, requires ultrashort pulses to snapshot the dynamics, in conjunction with triggering the dynamics by ultrafast pump pulses (88–90).

2.5.3 Full hyperspectral imaging

When characterizing the systems simultaneously along spatial and spectral (and sometimes temporal) dimensions, hyperspectral imaging is obtained, e.g., fully characterizing $M_i(\omega, r, t; R_i, \omega_i, A_i, \Gamma_i)$. The hyperspectral image can be expressed as

$$HSI = \sum_i M_i(\omega, r, t; R_i, \omega_i, A_i, \Gamma_i) = \sum_i (\sum_a \frac{A_{i,a}(t)}{(\omega - \omega_{i,a}(t)) + i \cdot \Gamma_{i,a}(t)}) \cdot \delta(r - R_i(t)) \quad \text{Eq. 8.}$$

Thus, in principle, it records the full dimensions of molecular information (Fig. 2.1). In practice, spectral coverage is chosen based on interests, e.g., the mid-IR spectra are measured if molecular structures and vibrational energy dynamics are of interest. The resolutions of hyperspectral imaging depend on the instrumental resolution: the time resolution is constrained by the instrumental response time, and the spatial resolution depends on the point spread function under diffraction limits (in theory, super-resolution techniques (82, 91) can be applied here to overcome the Abbey diffraction limit).

Under the instrumental resolution limits, molecules are characterized in all three dimensions. Thus, they can be better differentiated and categorized. For example, when two different molecules occupy the same location, but have different spectral features and temporal behaviors, they can be distinguished. Now, the collection of molecules X_N is categorized into many subensembles, within which the molecules share the same spatial, temporal, and spectral characters. Thus, when the hyperspectral microscopy is set to the

proper spectral range, data acquisition duration, and field of view, with the appropriate resolutions, it probes a complete set of optical knowledge of the molecular systems.

2.6 Combining VSFG with hyperspectral imaging

VSFG, acted as a spectral symmetry-selectivity filter, can further refine hyperspectral imaging to make it probe only molecules that satisfy non-centrosymmetric conditions, which is a unique approach that can study molecules in complex environments. Although combining VSFG with hyperspectral imaging sounds like an appealing solution for studying self-assembled systems, there are challenges in data collection and analysis. With 2D spatial information, 1D in the time and spectral domains, respectively, VSFGM has difficulty effectively collecting and extracting information in 4D (3D for static VSFGM). How to efficiently use the 2D of a charge-coupled device (CCD) camera and collect a 3D or 4D data cube is still a topic under development, and various schemes were developed on a case-by-case basis.

2.7 Femtosecond Laser and Optical Parametric Amplifier

Titanium-sapphire (Ti:Sapphire) laser system (Coherent) is used as initial light source. The laser outputs laser pulses center at 800 nm with repetition rate of 1 kHz. The output power is about 7 W with pulse duration of 35 fs.

About 60% of the initial laser power is used to pump the TOPAS (Light Conversion). TOPAS is the femtosecond optical parametric amplifier (OPA) for Ti:Sapphire lasers. The model used in this dissertation is TOPAS-Prime, which splits one 800 nm photon into two near infrared (NIR) photons. The

total power of these two NIR pulses are about 1 W.

The TOPAS is followed by a home-built difference frequency generation (DFG) setup, which generates mid-IR through DFG process of the two NIR photons. Nonlinear crystals such as KTA, AGS or BBO are usually used for the media of DFG process. In our experiment, when generating mid-IR around CH region, we used AGS crystal ($\Theta = 50°,\ \Phi = 0°$); when generating mid-IR around CH and OH region, we used KTA crystal ($\Theta = 47°,\ \Phi = 0°$); when generating mid-IR around OD region, we used AGS crystal ($\Theta = 39°,\ \Phi = 45°$).

The residual 800 nm (1.12 mJ) after TOPAS is sent into a 4f geometry pulse shaper to generate a spectrally narrowed upconversion pulse (output energy is 1.2 μJ, fwhm is 3.8 cm^{-1}, and the pulse shape is Gaussian with a pulse duration of 4 ps). The mode of the upconversion pulse is optimized by passing through a spatial filter.

Chapter 2, in part, is a reprint of the material as it appears in Annual Review of Physical Chemistry, 2021. Haoyuan Wang; Wei Xiong. Annual Reviews, 2021. The dissertation author was the primary investigator and author of this paper.

Chapter 3

Self-Phase-Stabilized Heterodyne Vibrational Sum Frequency Generation Microscopy

3.1 Heterodyne VSFG microscopy to study self-assembly

As discussed in Chapter 1, the classical detection scheme is homodyne detection, which measures the intensity of the signal fields as follows:

$I_{homo}(\omega) = |E_i^{(2)}(\omega)|^2$

Therefore, the phase information which represents the orientation of molecules, is missing. In heterodyne-detection VSFG, a local oscillator (LO) pulse that is at the same frequency as the VSFG signals will be generated collinearly aligned with the VSFG signals with certain time delay. Therefore, these two pulses will generate interference fringes on the CCD detector (in frequency domain). To extract the phase information, the heterodyne interference fringes are Fourier transformed into time domain, where an apodizing filter is applied to remove any dc signal (23, 69, 92). The time domain data are inverse Fourier transformed back to the frequency domain. The frequency domain molecular VSFG spectral phases are calibrated by non-resonance SFG spectra of z-cut quartz (92), which results in imaginary and real parts of molecular VSFG spectra.

3.2 Traditional heterodyne VSFG microscopy setup

The traditional heterodyne VSFG microscopy setup uses a Michelson interferometric geometry (16). In this geometry, an LO is generated in one of the Michelson interferometer arms and combined with VSFG signals in the other arm. Because LO and VSFG signals are generated in two separated beam paths, mechanical stability is extremely important to eliminate any phase drift. Furthermore, an interferometric geometry also presents challenges in alignment and maintenance.

3.3 Self-phase-stabilized heterodyne VSFG microscopy setup

Therefore, we present the first fully collinear HD VSFG microscope, which demonstrates excellent phase stability and circumvents technical challenges in spectrometer alignments. To further extract comprehensive molecular knowledge from VSFG images, we developed a spectral pattern recognition code based on a greedy algorithm. Using this code, we can differentiate domains with various molecular conformations, which would otherwise be difficult to distinguish using optical imaging techniques (93) or homodyne VSFG microscopes (27, 48, 57, 94–99). We implemented this phase-stable collinear HD VSFG microscope to study a host-guest molecular self-assembly spin-coated on gold. We found that the self-assembly contains non-centrosymmetric domains at sizes from about 20 to 100 μm^2, and there are mainly two types of domains, which have opposite molecular alignment relative to each other, or they could have different chirality. This microscope development should pave the way for implementing HD VSFG imaging in a broad range of applications in biophysics (100) and materials (101) and surface sciences. (102, 103)

The core experimental setup of the HD VSFG microscopy is illustrated below. The 800 nm (upconversion) and mid-IR pulses are combined by a customized dichroic optics (Newport), which passes

mid-IR and reflects 800 nm light. After the dichroic optics, both mid-IR and 800 nm pulses are collinear and overlapped temporally, and then they are focused together by a Schwarzchild (Edmund Optics, 15×/0.28 NA) reflective objective lens onto samples. The Schwarzchild objective lens is used to circumvent optical aberrations caused by refractive index differences of light at various frequencies. The generated VSFG signals, along with incident mid-IR and upconversion pulses, are reflected off a sample and are collected by the same objective lens. Because the incident beams are sent through one side of the objective entrance, the reflected beams are offset relative to incident beams after exiting the objective lens.

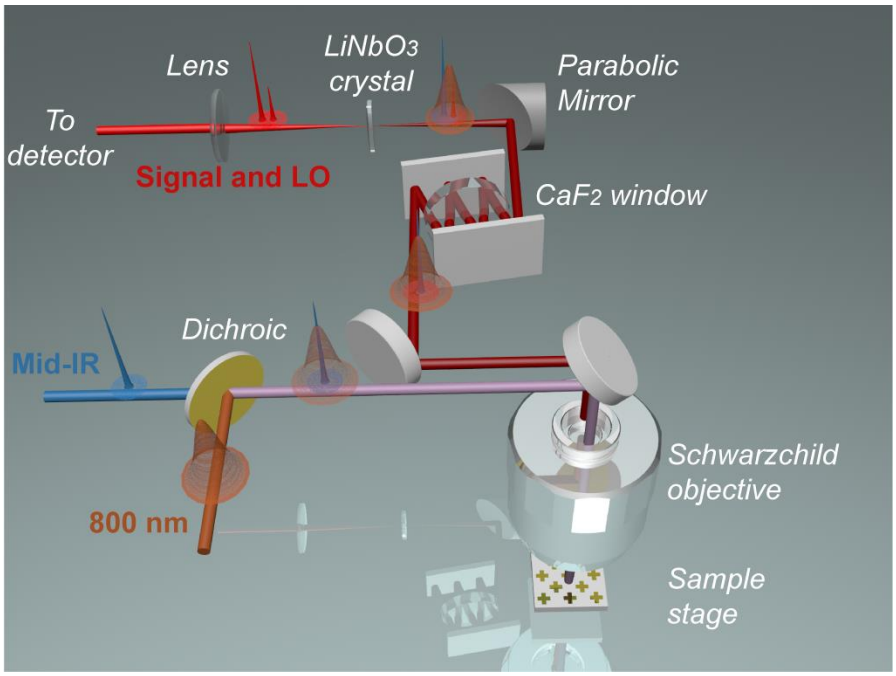

Figure 3.1. Schematic of the collinear heterodyne SFG microscopy system. Mid-IR and upconversion pulses are combined collinearly and overlapped temporally by a customized dichroic optic. These incident beams are sent through one side of a Schwarzchild objective lens to be focused on the sample. The reflected beams are offset relative to incident beams and picked up by a mirror. After the pick-up mirror, the VSDG signal, mid-IR and upconversion pulses are overlapped spatially and temporally. These three pulses are passed through a CaF_2 window to generate a time delay between VSFG signal and mid-IR and are then focused on a $LiNbO_3$ crystal to generate a local oscillator that is spatially collinear overlapped but temporally delayed relative to the VSFG signal.

The reflected VSFG signal, mid-IR, and upconversion pulses are picked up by a mirror, and all three pulses spatially and temporally overlap with each other. These three pulses are passed through an optical media to create relative time delays between the pulses (72). The time delay is necessary to ensure interference fringes between LO and SFG signals for heterodyne detection. In our setup, these pulses are bounced between two parallel mirrors and passed through a 7 mm CaF_2 window four times to generate a ~2 ps time delay between the SFG signal and mid-IR pulse. It is possible to generate the time delay, because there are non-negligible differences between refractive indices of the VSFG signal and mid-IR pulse. The upconversion 800 nm pulse has a similar refractive index to a visible pulse, so it is delayed by a similar amount as the SFG signal. The 2 ps time delay is a "sweet spot" for LO generation. Because the time duration of the upconversion pulse is 4 ps, the mid-IR pulse temporally overlaps with the front tail of the delayed 800 nm upconversion pulse, which ensures LO generation and creates the largest amount of time delay and therefore more interference fringes for extracting spectral phases. One pass through a 3 cm rod would perform the same function. After generating time delays, the beams are focused into a LiNbO3 crystal (MTI Corp., optical grade, X-cut, 10 × 10 × 0.5 mm) to create an LO, through an SFG process. Because SFG on the crystal is impulsive, an LO is generated only when mid-IR and upconversion 800 nm pulses overlap temporarily. Thus, LO duplicates the temporal profile of mid- IR and is delayed relative to the SFG signal. The LO and SFG signals are then sent through a few bandpass filters to remove any residual upconversion pulses and are focused into a spectrograph and detected on a charged coupled device (CCD) camera. The LO and SFG signals interfere with each other on the camera to generate heterodyned signals, an interference fringe pattern. The fringe space ($\Delta\omega$) and time delay between LO and VSFG signals (t) satisfy the relation $\Delta\omega \cdot\cdot t = 1$.

Chirps originated from GVD/TOD of CaF_2 in our setup are negligible since the IR has relatively narrow bandwidth (section 3.5). To obtain an HD VSFG image, the sample is scanned spatially by an automated stage. The exposure time for each pixel is 2 s, and for a typical 100 μm × 100 μm image, the scanning time is about 2 h. The heterodyne interference fringes are Fourier transformed into time domain, where an apodizing filter is applied to remove any DC signal (23, 69, 92). The time domain data are inverse Fourier transformed back to the frequency domain. The frequency domain molecular VSFG spectral phases are calibrated by nonresonance SFG spectra of z-cut quartz (92), which results in imaginary and real parts of molecular VSFG spectra. We note our current scheme works for Gaussian shape upconversion pulses, but not for etalon shape pulses, because mid-IR is ahead of upconversion pulses when arriving at a $LiNbO_3$ crystal and therefore cannot overlap with etalon upconversion pulses. This issue can be solved by generating an LO before the sample (72).

The largest advantage of this new HD VSFG microscope is that an LO pulse is created from the same pulses that generate VSFG signals. The benefits are threefold: First, an LO is intrinsically collinear with the VSFG signal, because they are generated by the same collinear mid-IR and upconversion pulses. This geometry eliminates the necessity of extra procedures to align the LO to be collinear with the VSFG signal, which is difficult but also the most critical factor in heterodyne detection. Second, the spectral phase measured using this new setup is not sensitive to sample height. In heterodyne detection, where an LO is generated on a different beam path from signals, a small change of sample heights (~200 nm) is enough to change the spectral phase. In our setup, because all pulses are reflected from the sample, height variations would change the beam paths of all pulses together. Thus, the measured phase reveals only molecular orientations, but not sample heights. Third, because all beams travel along the same beam path, phase

fluctuation and drifts due to mechanical instability are largely alleviated. To illustrate this benefit, we measure the phase of the HD VSFG signal as a function of time, acquired using this collinear HD VSFG microscope and a Michelson interferometric HD VSFG microscope. The Michelson interferometric HD VSFG microscope uses the same optical parts as the collinear setup, except that an additional arm is used to generate the LO.

Thus, each microscope experiences the same amount of mechanical instability. In 12 min of measurements using the Michaelson interferometric HD VSFG microscope, the standard deviation of the phase is 0.44 radian, with the largest variation being 2.81 radians. Although phase acquired from the Michelson interferometric setup does not drift over 12 min of measurements, the spectral phase does fluctuate randomly on a large scale in the time frame of 10 s. On the other hand, the collinear HD VSFG microscope demonstrates a rock-solid phase stability, with a 0.039 radian standard deviation and 0.35 radian being the largest variation (Fig. 3.2). Thus, the collinear setup enhances phase stability by at least 9 times. In addition, the collinear HD VSFG microscope shows good long-term phase stability. During a 2 h window, the phase drifted only about 0.032 radian. As mentioned above, the image scan time is about 2 h. Thus, this phase stability is critical for improving the fidelity of phase extracted from a point-to-point scanning heterodyne microscope.

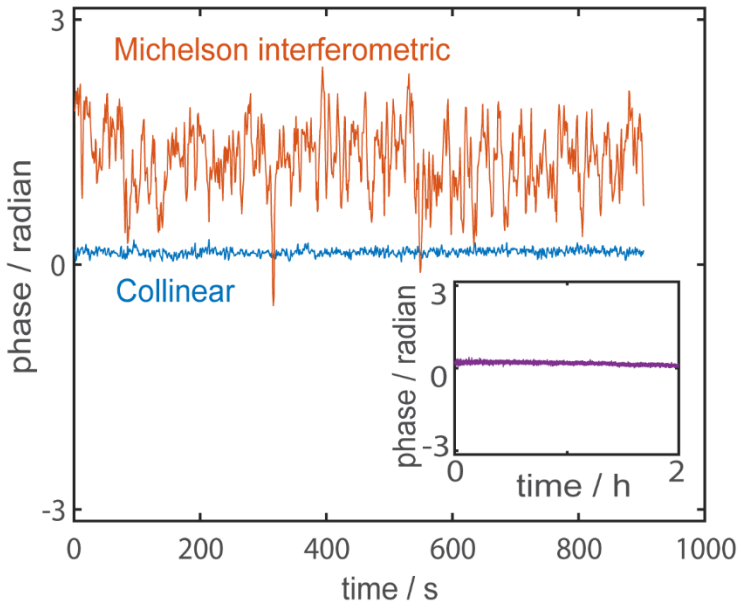

Figure 3.2. Phase stability of HD VSFG microscope. Collinear HD VSFG microscope shows little phase fluctuations in both short (blue) and long (insert, purple) terms. In comparison, a Michelson interferometric setup shows overall stable phase, but large fluctuations at 10 s time scales.

Next, we examine the quality and resolution of microscopic images. We acquire and compare optical and HD VSFG images of a lithographic pattern composed of gold and GaAs. SFG signals from gold and GaAs form good contrasts, as GaAs has a larger SFG signal than gold. Comparing the two images shows that the SFG image captures all the features shown in the optical image, including edges and the curved corners (Fig. 3.3 a and b). To determine the resolution, we scan across sharp edges between gold and GaAs and fit the first-order derivative of SFG intensity into a Gaussian model. We found the resolution is <2 μm, which is close to the theoretical limitation (1.2 μm) defined by the 80% separation criterion (104) (Fig. 3.3 c). The resolution can be further improved by expanding the 800 nm beam size or using a larger numerical aperture (NA) objective, which is beyond the scope of this report.

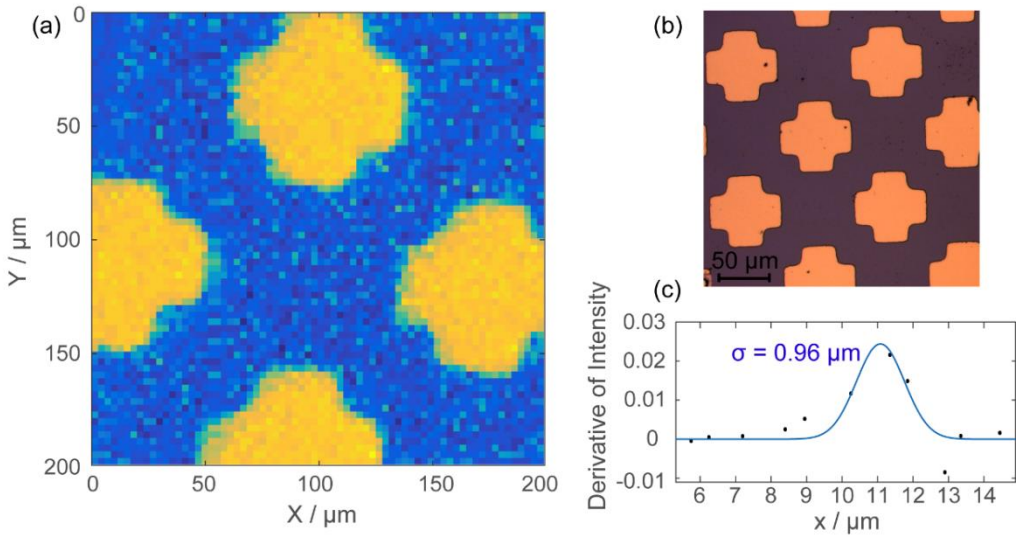

Figure 3.3. Image and resolution examination of sample pattern. (a) HD VSFG and (b) optical images of a GaAs/Au pattern.
(c) Scan across the GaAs/Au edge, Gaussian fitting of the first derivative of SFG intensity. Based on 80% separation criterion, the resolution is about 1.8 μm.

3.4 Applications in self-assembly

After examining the phase stability and resolution, we use the collinear HD VSFG microscope to investigate molecular self-assembly systems spin-coated on gold. The molecular self-assembly is formed by sodium dodecyl sulfate (SDS) and β-cyclodextrin (β-CD) through host−guest interactions, which is a good building block for responsive molecular devices and biomimic structures. (105, 106) β-CD forms a cup-shaped structure, with one of the rims being narrower than the other. One SDS molecule can form a complex with two β-CDs, and the conformation of the two β-CD molecules can be head-to-head, tail-to-tail, or head-to-tail. Simulations have shown that the head-to-head configuration is the most stable due to more hydrogen bonds. (107) However, head-to-tail conformations can also exist. Most existing techniques cannot distinguish between these different conformations, but the VSFG signal has a unique ability to identify head-to-tail conformations, because head-to-tail conformations are non-centrosymmetric and

generate strong VSFG signals. (37) Thus, the HD VSFG microscope is ideal for spatially differentiating between head-to-tail and head-to-head conformations.

The HD VSFG microscope image of molecular self-assembly contains ample spectroscopic information, including spectral intensity, phase, peak position, and line shapes (Fig. 3.4). By plotting the image based on different spectral features, various molecular aspects of these self-assemblies can be obtained. One approach is to plot the absolute integrated VSFG intensity image (Fig. 3.4 e). On the basis of this intensity image, we conclude the self-assembly sample is very inhomogeneous, composed of domains that have strong and weak VSFG signals, and the size of the domains ranges from 20 to 100 μm^2. Because molecular self-assembly fully covers gold substrates, the difference in VSFG intensity reflects various domain conformations, but not surface coverage: for example, domains with strong VSFG signals consist of head-to-tail conformations, because they are non-centrosymmetric, whereas domains with weak signals are composed of head-to-head configurations. (37)

However, there is much more information to be learned than what the VSFG intensity image can reveal, because in the HD VSFG image, each pixel encodes a phase-resolved HD VSFG spectrum. To take advantage of the rich spectral information, we further characterize each domain by comparing all the spectral patterns of their imaginary spectra (corresponding to absorptive spectra) (23, 69, 74, 92, 108), including peak position, phase, and line shapes. This spectral pattern recognition is done by a greedy algorithm (109), which can be easily extended to images that contain large data points. The algorithm sorts every pixel in the image based on its spectral similarity in every run and iterates the comparing mechanism until the sorting results converge. Then, pixels that are grouped as the same type are plotted in the image with the same color.

Using the spectral pattern recognition code, HD VSFG images of molecular self-assembly are sorted based on spectral similarity. We found six types of spectra in the image, with type 1 and 2 dominating (green and orange in Figure 3.4 a and c). The HD VSFG image is replotted as a spectral image, in which pixels of the same spectral type are coded with the same color (Fig. 3.4 a). The spectral image shows that pixels within each domain have the same spectral type, which indicates molecules in each domain adopt the same conformation. This result agrees with VSFG signal selection rules: VSFG can only survive when the interfaces or domain formed by molecules are ordered and non-centrosymmetric. Otherwise, their signals cancel each other out. (32, 43, 45) We note that there are four minor spectral shapes in the HD SFG image (bottom four of Fig. 3.4 c). These minor spectral pixels often appear at the edges or boundary of a domain. Thus, we assume these spectra are signatures of domain edges, whose structures are not as ordered as those of molecules at the centers of domains, or they are signatures of boundaries between two domains with different conformations, whose spectra should be an average result of molecules in both domains. The two dominating imaginary spectra have features that are similar to each other, but are out of phase by π (top two of Fig. 3.4 c). Both spectra include two noticeable peaks, a large peak at 2900 cm^{-1} and a small peak at 2870 cm^{-1}. A control experiment to measure the VSFG signal of deuterated SDS/β-CD molecular self-assembly shows that the VSFG spectral phase of deuterated SDS/β-CD is similar to the nondeuterated complex (15). Because deuteration shifts the CH stretch of SDS to 2000 cm^{-1}, (110) this result suggests the two vibrational peaks of Figure 3.4 c originate mainly from β-CD. This conclusion agrees with a previous study on a similar molecule. (111)

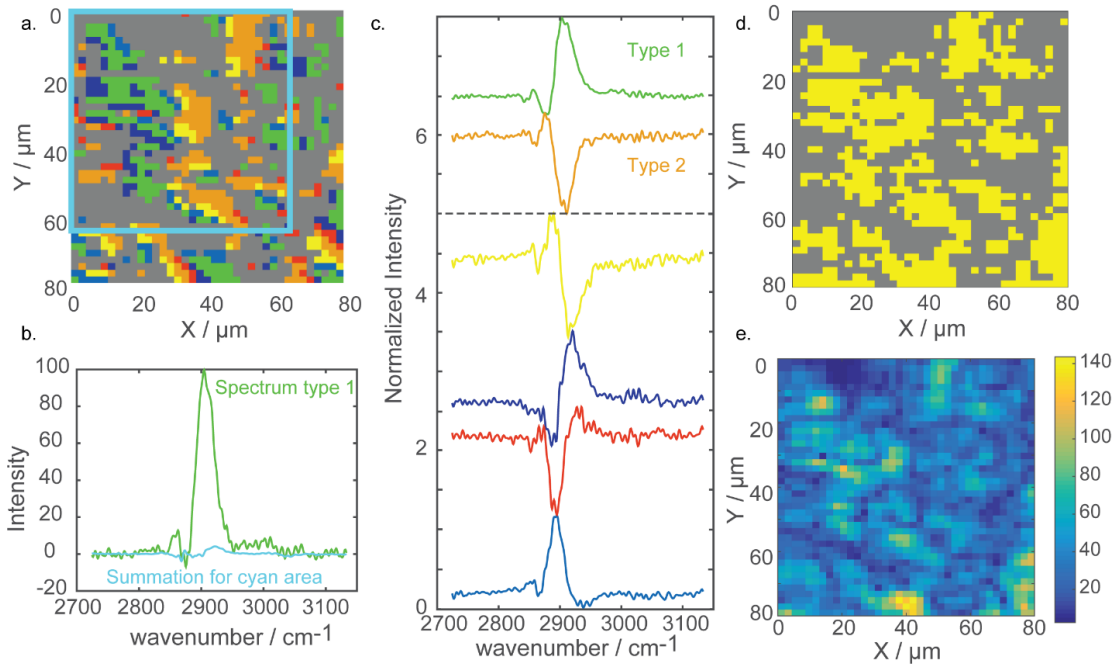

Figure 3.4. HD SFG image of molecular self-assembly. (a) Domain assignment of HD SFG image by the spectral pattern recognition code: pixels with similar spectral line shape are coded to the same color. (b) Summation of the cyan area (60 μm × 60 μm) in (a) mimics an ensemble-averaged HD SFG imaginary spectrum. It shows that under ensemble-average, HD SFG signals are mostly cancelled out. c) Color coded HD SFG imaginary spectra that corresponds to the same colored pixels in (a). Type 1 and type 2 are imaginary spectra of two dominant types and the rest of four are spectra of minority pixels at boundary of domains. (d) Domain assignment of the absolute square of HD SFG signal (equivalent to homodyne SFG), which shows phase is critical information for spectral recognition. (e) The HD SFG intensity image, which reveals various domains existing at the surface, but is lacking molecular information.

On the basis of literature reports, we assign the peak at 2900 cm^{-1} to be the asymmetric modes of CH_2 in β-CD and the peak at 2870 cm^{-1} to be the CH stretch of β-CD. (111) There are no CH_3 peaks of SDS observed because of the relatively small population of CH_3 groups in molecular self-assemblies. From peak assignments and corresponding spectral phases, we can determine the molecular orientation in each domain. As discussed previously, the molecules in domains that are visualized in HD VSFG microscopy should correspond to the head-to-tail configuration, which generates strong VSFG signals. On the basis of Gaussian calculation (112), the vibrational transition dipole vectors of CH asymmetric modes are rigid and

always point from narrow to wide rims of the β-CD cup.

Thus, we conclude that domains with type 1 spectra correspond to self-assembly aligned with the cup facing down, and a molecular self-assembly in domains with type 2 spectra faces the opposite direction (Fig. 3.4 c). The CH_2 asymmetric mode highly depends on local hydrogen bond environments, and its orientation relies on whether the basis sets and methods used in the calculation can properly model hydrogen bonding, which is out of the scope of this work. However, because the CH_2 peak always has an opposite sign of that of the CH peak, it indicates the CH_2 asymmetric mode has stable orientations due to hydrogen-bonding networks and always points in the opposite direction of the CH vibrational mode. A more detailed structure study of the molecular self-assembly will be reported in the future.

The ability to distinguish domains in HD VSFG microscopy is not possible with heterodyne VSFG spectroscopy or homodyne VSFG microscopy. First, to show the difference between HD and homodyne VSFG microscope images, we calculate the homodyne VSFG spectra by taking the absolute square value of HD VSFG spectra. Then, we use the same spectral pattern recognition code to analyze this homodyne VSFG image. We found all domains are sorted into the same type (Fig. 3.4 d), because the phase information is lost in homodyne signals. Second, to see how spectra of this self-assembly would look in an HD VSFG spectrometer that measures areas with diameters of 50 to 100 μm, we sum all heterodyne VSFG spectra inside of the cyan squared area (60×60 μm^2). The summed spectrum (cyan) in Figure 3.4 b appears to have a negligible spectral intensity compared to a VSFG spectrum from a single pixel in the HD VSFG image (Fig. 3.4 a). This is because spectra with different phases destructively interfere with each other in the cyan

square. If the ensembleaveraged HD SFG spectrum is used to study structure of this self-assembly, a conclusion that no head-to-tail self-assembly exists in this sample could be made, but would be misleading. Thus, the HD VSFG microscope is an essential tool to reveal spatial inhomogeneity, deconvolve ensemble-averaged spectra, and resolve spectral phase to determine molecular conformations.

3.5 Conclusion, future possible improvement, and perspective

In conclusion, we report a new design of HD VSFG microscope that shows a 9-fold improvement in phase stability. This increase in stability greatly enhances the fidelity of spectral phase extracted from the scanning microscope. In addition, LO is intrinsically collinearly aligned with the VSFG signal, which ensures a heterodyne signal of excellent quality and makes spectrometer alignment simple. To further take advantage of the richness of VSFG spectral information, we implemented a spectral pattern recognition code. We used the microscope and code to investigate molecule self-assembly samples and identified two molecular domains with opposite molecular orientation. The simplicity of alignments and stability of spectral phase of this new HD VSFG microscope lay the technical foundation for unraveling comprehensive molecular spectral knowledge and opening new avenues for studying indepth molecular physics of molecular interfaces and domains in environmental surfaces, (113, 114) heterojunction materials, (115) biological systems, (100, 116) and surface catalysts. (101, 117) The design can also be modified and developed into a wide field illuminated HD-VSFG microscope in combination with compressive sensing to increase data acquisition speed. (51)

However, even if the GVD/TOD is negligible in this experiment, it is only the case for relatively narrow band IR. For example, the IR bandwidth is about 80 cm^{-1} in our experiment. However, GVD/TOD

would become much larger for wider IR bandwidth. If the IR frequency coverage becomes 5 times larger, the GVD would become 25 times bigger while TOD would become 125 times larger.

For example, in the simulation, the bandwidth is only 80 cm^{-1} and the GVD is calculated to be negligible. However, if a broad band IR is used, the GVD could be much larger. In our broad band IR VSFG experiment, the bandwidth is about 800 cm^{-1}. Therefore, the GVD would be 100 times larger than that of 80 cm^{-1}, and the GVD is no longer negligible.

Chapter 3, in full, is a reprint of the material as it appears in ACS Photonics, 2017. Haoyuan Wang; Tian Gao; Wei Xiong. American Chemistry Society, 2017. The dissertation author was the primary investigator and author of this paper.

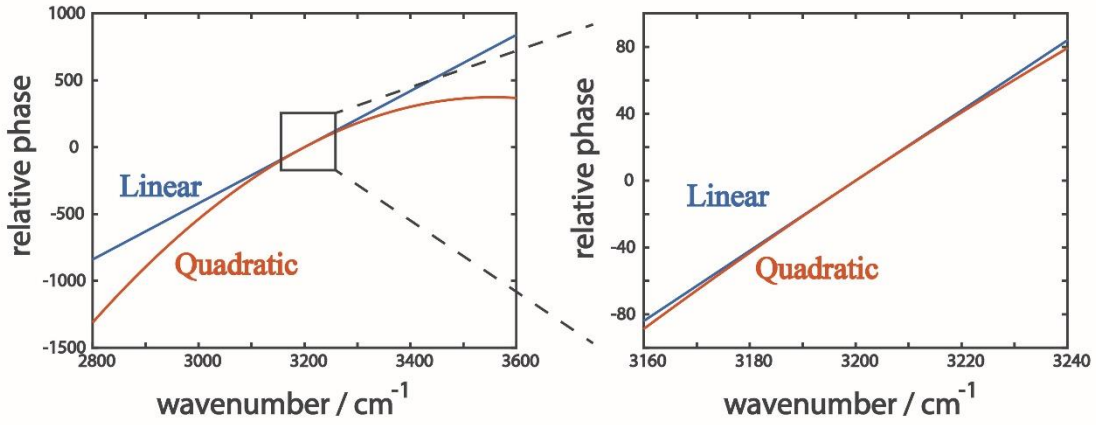

Figure 3.5. (Right) If the IR is relatively narrow band, the GVD is negligible. However, if the IR bandwidth becomes broader (Left), the GVD would increase nonlinearly. This is why such heterodyne-detection technique works for 80 cm^{-1} bandwidth IR in this scenario but cannot work for even broader bandwidth.

Chapter 4

Local Ordering of Lattice Self-Assembled SDS@2β-CD Materials and Adsorbed Water Revealed by Vibrational Sum Frequency Generation Microscope

In order to study the interactions between self-assemblies and water, we extended the IR coverage to OH stretching modes. A KTA crystal was used to generate IR at this region, and the total output is from 2700-3500 cm^{-1} with 7 μJ, in which 0.5 μJ was used for static VSFG microscopy.

We observed some VSFG peaks in the OH region, and there is inhomogeneity in the VSFG map (Fig. 4.1). Furthermore, we also found all the spectra are qualitatively similar but quantitively different for each domain. In this thesis, I will first discuss the origin of the VSFG signal in the self-assembly system. After that, I will make peak assignment based on Voigt spectral fitting result. In the end, I will discuss the spatial inhomogeneity.

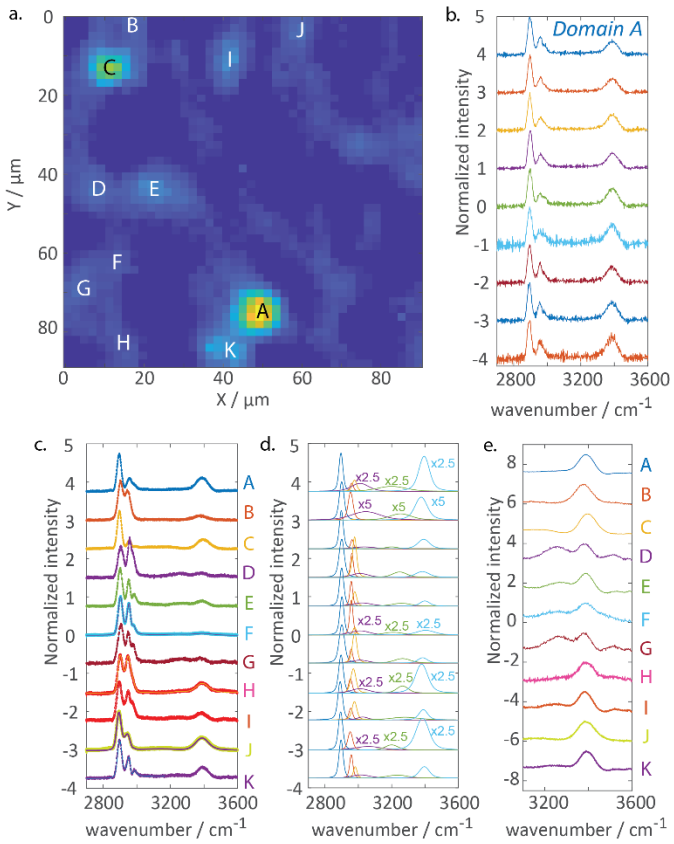

Figure 4.1. (a) VSFG image for OH region of molecular self-assembly. (b) Spectra of different positions in domain A look similar. (c) Individual spectrum of each domain with spectral fitting. (d) Individual component of each domain and (e) zoomed-in spectrum for OH region. All spectra have been normalized to their own maximum and have been offset vertically for better visualization.

4.1 Details about spectral fitting

VSFG spectral fitting is done by Matlab code provided by Paul Cremer's group with minor modification.(118, 119) The code uses a Voigt profile, which is the convolution between Lorentzian and gaussian profile, to fit the spectra. For each individual peak, a Lorentzian profile of specified width is generated first (2 cm^{-1} for CH peak and 5 cm^{-1} for OH peak) (119); later these Lorentzian profiles are convoluted with a Gaussian profile to generate a Voigt profile. A non-resonant background constant is also considered, and all these profiles are summed to calculate the absolute square to fit the spectra. After each

iteration, the output result of previous iteration is chosen to be the input for the next iteration, and iteration continues until the fitting results converge.

$$I(\omega_{IR}) \propto |\chi^{(2)}_{NR} e^{i\psi} + \sum_v \int \frac{A_v e^{i\psi_v}}{\omega_{IR} - \omega_L + i\Gamma_{L,v}} * e^{-(\frac{\omega_L - \omega_v}{\Gamma_v})^2} \, d\omega_L \,|^2 \qquad \text{eq.9}$$

Where I is intensity; $\chi^{(2)}_{NR}$ and ψ are the second order susceptibility and phase of the non-resonant background; A_v, ω_v, Γ_v, $\Gamma_{L,v}$, ψ_v are the amplitude, center resonant frequency, gaussian linewidth (due to inhomogeneous broadening), and individual Lorentzian linewidth (due to homogeneous broadening) and phase (either be 0 or π) of vibrational mode v, respectively, where ω_L is the center frequency of each individual Lorentzian.

4.2 Origin of VSFG signal of SDS@2β-CD Self-Assembly Sheets

It is important to understand the origin of these VSFG peaks, because the VSFG signal is not from air/water interfaces, or any general plane interfaces, but from well-ordered lattice self-assembled materials. The key reason this material is VSFG active arises from its *chirality* and *lack of inversion symmetry*. A VSFG signal only exists in ordered, non-centrosymmetric systems,(120) such as interfaces. Because there are multiple layers in each sheet, the detected VSFG signal is clearly not from a monolayer interface. Instead, the source of broken symmetry comes from the chiral β-CD and SDS@2β-CD self-assembled sheets. We note there is no CH VSFG signal from SDS, as confirmed from no VSFG signal change upon deuterating SDS in the samples in Chapter 3.(15)

β-CD molecule has C_7 symmetry, and based on molecular dynamics simulation(121) and experiment results(105), two β-CD molecules stack together head-to-head to form a "channel" type structure in the SDS@2β-CD supramolecule. Based on X-ray crystallography results (Fig. 4.2), the two β-

CD molecules would not form an eclipsed geometry, (i.e., the two C_7 β-CD molecules do not overlap entirely on each other when viewing from z axis), in order to form more hydrogen bonds. Thus, they do not have a C_2 axis perpendicular to C_7 axis, nor along C_7(z axis, Fig. 4.2); what is more, β-CD is a chiral molecule and does not have mirror plane in the xy plane. The lack of an xy mirror plane and C_2 along z axis results in lack of inversion center, i. Therefore, the overall symmetry of self-assembled SDS@2β-CD supramolecule is only C_7, without C_2 and i. As a result, second order optical susceptibilities, β_{zzz}, $\beta_{xxz} = \beta_{yyz}$, $\beta_{xzx} = \beta_{yzy} = \beta_{zxx} = \beta_{zyy}$, $\beta_{xzy} = \beta_{zxy} = -\beta_{yzx} = -\beta_{zyx}$, are non-zero.(122)

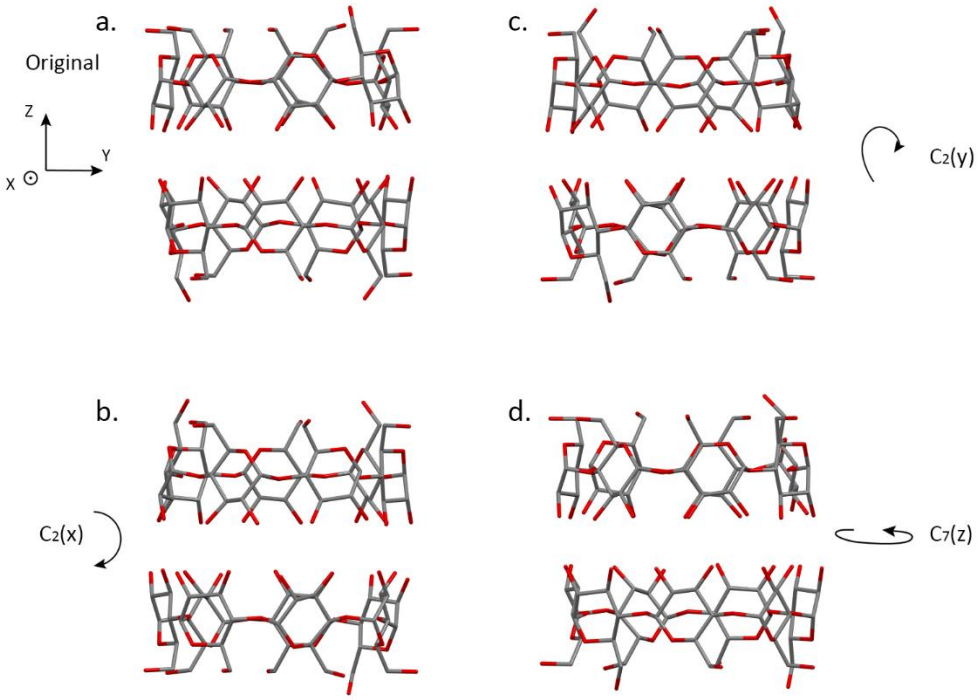

Figure 4.2. (a) β-CD dimer structure obtained through single crystal X-ray diffraction. All the hydrogen atoms have been hidden for better visualization. From the dimer structure, we can see that the two β-CD molecules are not in the eclipsed geometry. (b) After rotating the dimer by π at x axis, the rotated structure does not have the same framework as the original structure. (c) After rotating the dimer by π at y axis, the rotated structure still does not have the same framework. (d) After rotating the dimer by 2π/7 at z axis, the skeleton of rotated structure has the same framework as the original structure. The results above indicate the dimer does not have C_2 axis.

The chiral dimer self-assembles into layers of sheets. Based on our previous study(20) and optical images, sheets were observed to assume a parallelogram shape with an angle of 104°. This angle has been assigned as the exact angle for 7-fold symmetry in β-CD, which maximizes direct hydrogen bonds.(20) Because the formed sheet has C_2 symmetry about z axis while the supramolecule has C_7 symmetry, only C_1 symmetry remains with the combination of these two (Figure. 4.3 a). This C_1 symmetry leads to a striking result: different from interfaces with C_∞ symmetry, which have 11 non-zero second order optical susceptibilities, a C_1 symmetry system can have any second order susceptibilities to be non-zero, including χ_{xxx} (the corresponding equation is summarized in eq.10). The net result is that there should be SFG signal under SSS polarization, which does not exist in any C_∞ symmetry systems. Based on eq.10, we also note that it is important for the SDS@2β-CD supramolecule to have a non-zero tilt angle (θ) to generate SSS polarization signal.

$$\chi_{SSS}^{(2)} = L_{xx}(\omega_{\mathrm{SFG}})L_{xx}(\omega_{\mathrm{VIS}})L_{xx}(\omega_{\mathrm{IR}})\chi_{xxx},$$

$$\frac{\chi_{xxx}}{N} \propto \beta_{zzz} \cdot (\sin\theta\cos\phi)^3 +$$

$$\beta_{xxz} \cdot (-\sin\psi\sin\phi + \cos\theta\cos\psi\cos\phi)^2 \cdot \sin\theta\cos\phi +$$

$$\beta_{yyz} \cdot (-\cos\psi\sin\phi - \cos\theta\sin\psi\cos\phi)^2 \cdot \sin\theta\cos\phi +$$

$$\beta_{xzx} \cdot (-\sin\psi\sin\phi + \cos\theta\cos\psi\cos\phi)^2 \cdot \sin\theta\cos\phi +$$

$$\beta_{yzy} \cdot (-\cos\psi\sin\phi - \cos\theta\sin\psi\cos\phi)^2 \cdot \sin\theta\cos\phi +$$

$$\beta_{zxx} \cdot (-\sin\psi\sin\phi + \cos\theta\cos\psi\cos\phi)^2 \cdot \sin\theta\cos\phi +$$

$$\beta_{zyy} \cdot (-\cos\psi\sin\phi - \cos\theta\sin\psi\cos\phi)^2 \cdot \sin\theta\cos\phi +$$

$$\beta_{xzy} \cdot (-\sin\psi\sin\phi + \cos\theta\cos\psi\cos\phi) \cdot (-\cos\psi\sin\phi - \cos\theta\sin\psi\cos\phi) \cdot \sin\theta\cos\phi +$$

$$\beta_{zxy} \cdot (-\sin\psi \sin\phi + \cos\theta \cos\psi \cos\phi) \cdot (-\cos\psi \sin\phi - \cos\theta \sin\psi \cos\phi) \cdot \sin\theta \cos\phi +$$

$$\beta_{yzx} \cdot (-\sin\psi \sin\phi + \cos\theta \cos\psi \cos\phi) \cdot (-\cos\psi \sin\phi - \cos\theta \sin\psi \cos\phi) \cdot \sin\theta \cos\phi +$$

$$\beta_{zyx} \cdot (-\sin\psi \sin\phi + \cos\theta \cos\psi \cos\phi) \cdot (-\cos\psi \sin\phi - \cos\theta \sin\psi \cos\phi) \cdot \sin\theta \cos\phi$$

$$= \beta_{zzz} \cdot \sin^3\theta \cos^3\phi + \beta_{xxz} \cdot (\sin\theta \cos\phi - \sin^3\theta \cos^3\phi) +$$

$$2\beta_{xzx} \cdot (\sin\theta \cos\phi - \sin^3\theta \cos^3\phi) \qquad \text{eq.10}$$

In Figure 4.3 c, we found strong SSS polarization signal from SDS@2β-CD sheets, including both CH and OH spectral region, agreeing with the conclusion from the symmetry consideration. The existence of this SSS polarization signal indicates anisotropy in this sample, which comes from the highly coordinated ordering in the self-assembling sheets. If the supramolecules are randomly arranged in the sheets, the sheets could have C_2 symmetry and will not have any SSS polarization signal.

To further test this statement, we studied SDS@2γ-CD self-assembled sheets. γ-CD is from the same family as β-CD, the only difference is that there are 8 D-glucopyranosyl residues in γ-CD, and thus SDS@2γ-CD supramolecule have C_8 symmetry. The self-assembled SDS@2γ-CD sheets are square shape with C_4 symmetry(20), so C_4 is the overall symmetry of these sheets. Under C_4 symmetry, χ_{xxx} does not exist, and therefore SSS polarization SFG signal would not be observed. No SSS polarization signal was detected for SDS@2γ-CD, while strong PPS/PSP/SPP signals were found. Therefore, to conclude this section, we can confirm that the strong SSS signal, along with other chiral SFG signals, such as PPS, indicate the signal comes from the overall C_1 symmetry of SDS@2β-CD and the chirality of β-CD. Otherwise, there should be only achiral SFG signals(59).

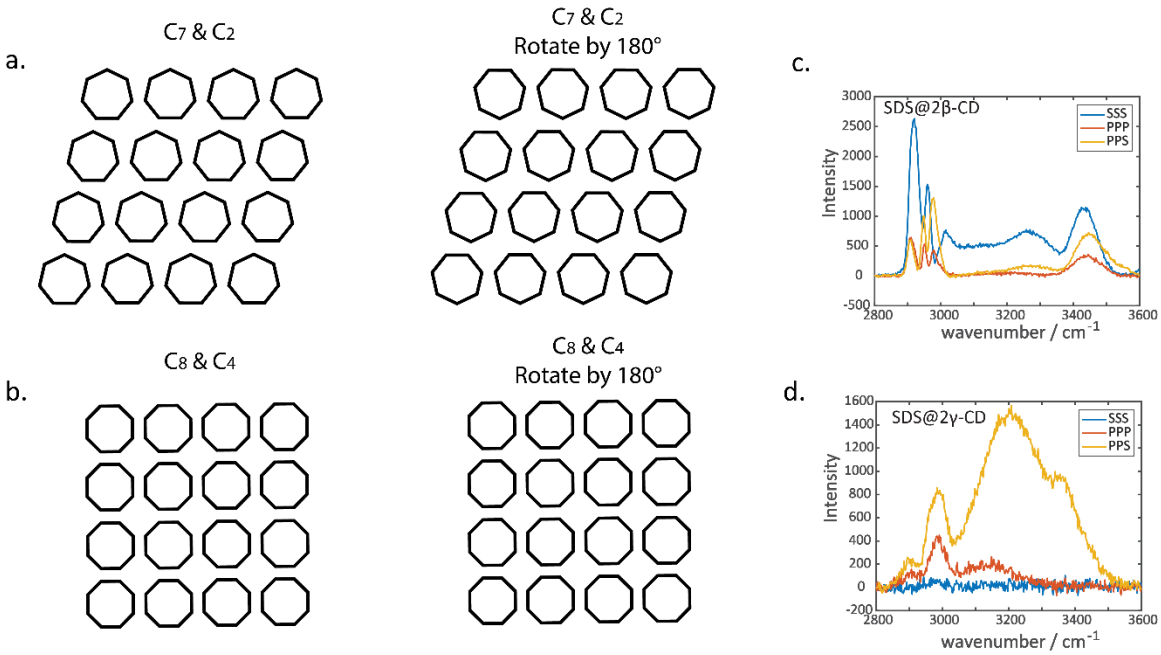

Figure 4.3. Schematic showing (a) when C_7 symmetry molecules assemble into C_2 symmetry parallelogram, the overall symmetry could only be C_1; (b) while when C_8 symmetry molecules assemble into C_4 symmetry square, the overall symmetry at least has C_2 axis. SSS, PPP and PPS polarization VSFG spectra of (c) SDS@2β-CD and (d) SDS@2γ-CD self-assembling sheets.

4.3 Multiple OH peaks originated from β-CD and adsorbed water

After understanding the origins of VSFG signals, we turn our attention to the spectral assignments of the complicated VSFG spectra. We first used Voigt profile to fit the VSFG spectra and found for all VSFG spectra taken at various spatial points, there are always three dominating peaks in the 2800 to 3000 cm^{-1} range, corresponding to the CH resonances, in addition to three peaks from 3000 to 3600 cm^{-1} corresponding to the OH bands. (Fig. 4.1 b and c) Those three OH peaks are at ~3050, ~3280 and ~3400 cm^{-1}, respectively.

To further assign the OH peaks, we first conducted FTIR measurements at different RH conditions. Because FTIR is sensitive to the concentration of molecular vibrational modes but not symmetry (therefore self-assembly ordering and structures), the interpretation of FTIR results are more straightforward than

VSFG. We fitted the FTIR OH spectra under different RH conditions with five gaussian peaks. (Fig. 4.4 a) The peak positions for these five peaks are at 3100, 3270, 3390, 3480 and 3570 cm^{-1}, respectively. The peak intensity variation as a function of RH is summarized in Table 4.1. Based on literature (123), the 3390 cm^{-1} peak is assigned to be the primary OH of β-cyclodextrin, which also agrees with the fact that its intensity remains nearly the same after reducing RH. The primary OH is expected to only form a weak hydrogen bond (HB) due to large orientation freedom, which results in the highest vibrational frequency. The 3480 and 3570 cm^{-1} peaks are assigned to be loosely bound water, both of whose intensities reduce dramatically as RH decrease. The 3100 and 3270 cm^{-1} peaks reduce nearly the same amount, indicating that they both are strongly dependent on the water in the self-assembly materials. The 3100 and 3270 cm^{-1} peaks have been assigned to strongly, hydrogen-bonded water and secondary OH of β-cyclodextrin, respectively, by literature.(123) Based on our result, because both modes are highly dependent on RH, they should be highly delocalized, e.g., hybrid vibrations between OHs of hydrogen-bonded water and secondary OHs, where the 3100 cm^{-1} peak contains more contribution from water OH and 3270 cm^{-1} peak has more secondary OH of β-CD character.(124) The secondary OHs are on the internal rims of the complex and form HBs with each other and with surrounding water, resulting in a redshift relative to primary OH peaks.

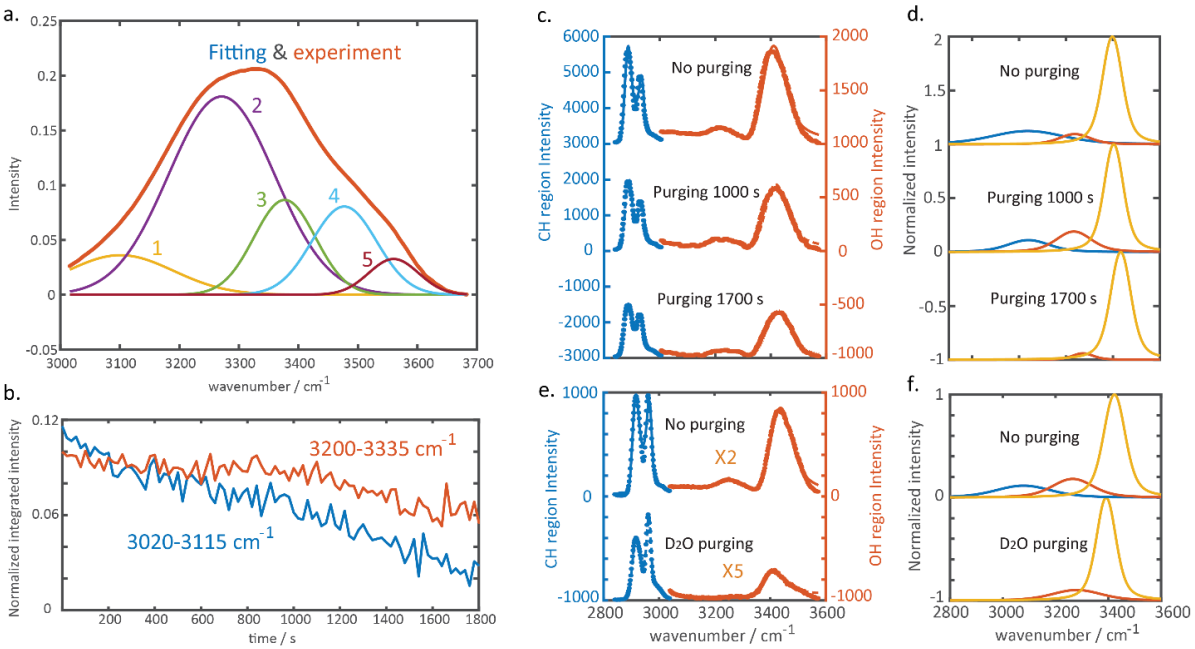

Figure 4.4. (a) The FTIR signal of SDS@2β-CD sample at RH=25% and fitting results with 5 gaussian peaks. Based on literatures and RH dependent FTIR experiment, these five components are assigned to be strongly-hydrogen-bonded water, secondary OH of β-cyclodextrin, primary OH of β-cyclodextrin, interstitial water and cavity water respectively. (b) Integrated VSFG spectra of different spectral regions, and the integrated intensity has been normalized by the CH region intensity to alleviate laser intensity fluctuation. (c) VSFG spectra fitting under different purging time in (b); (d) individual fitting component in (c). (e) VSFG spectra fitting of another position under ambient condition and with D_2O purging; (f) individual fitting component in (e).

Table 4.1. Individual peak intensity under different RH

	RH = 25%	RH = 1%	RH = 0%
Component 1 (~3100 cm^{-1})	0.036	0.018	0.017
Component 2 (~3270 cm^{-1})	0.18	0.11	0.10
Component 3 (~3390 cm^{-1})	0.087	0.086	0.078
Component 4 (~3480 cm^{-1})	0.081	0.032	0.018
Component 5 (~3570 cm^{-1})	0.033	0.012	0.005

We note that the strongly bound water, primary and secondary OH modes from β-CD also appears in VSFG spectra (see fitting results from Figs. 4.1 and 4.4 d and f). To further confirm the peak assignments in VSFG, we purged the sample with dry air and collected VSFG spectra every 20 s to track the dehydration dynamics. We integrated VSFG signals of the strongly bounded water and secondary OH regions. The strongly bound water (3020-3115 cm^{-1}) spectral region signal intensity continues decreases as the RH decreases, while the (3200-3335 cm^{-1}) spectral region signal intensity remains nearly constant during the first 1000 s and decreases only modestly afterwards (Fig. 4.4 b). From the spectral fitting results, the peak at ~3050 cm^{-1} disappears after 1700 s while the peak at ~3280 cm^{-1} persists at RH ~10% (Fig. 4.4 c and d). These results all support the assignment that the peak at 3020-3115 cm^{-1} has a dominant contribution from the OH in water, whereas the 3200-3335 cm^{-1} spectral feature also have some water OH contributions. This ~3050 cm^{-1} peak indicates that the strongly bound water forms strong HB networks among each other and the secondary OHs of neighboring β-CD, an added "adhesion force" between β-CDs. It is also noticeable that the ratio between secondary and primary OHs becomes larger, as dehydration occurs, which could be used as an indicator of hydration level of the self-assembly. We note if the samples are further dehydrated, the VSFG spectra would change dramatically indicating self-assembly structural changes, which we will report in a separate publication. To ensure that the spectral change we observed in Fig 4.4 c and d is because of losing of H_2O, instead of structural change, we further performed additional experiments of D_2O/H_2O exchange. Upon purging with D_2O, the strongly bound water peak disappears first, while the secondary OH peak remain intact at that time (Fig. 4.4 e and f). Because the sample is kept at constant RH during D_2O/H_2O exchange, the D_2O/H_2O exchange experiments rule out the possibility that the spectral change are due to self-assembly structural change induced by dehydration.

The fact that OH band of water in SDS@2β-CD is VSFG active is very intriguing. If the water molecules are loosely bound, like bulk liquids, they are expected to be isotropic and, therefore, not VSFG active. On the other hand, a broad VSFG peak of water OHs indicates that interactions between β-CD and nearby water molecules are strong enough that these water molecules are templated by β-CD through HB networks. As a result, these water molecules adopt the symmetry of SDS@2β-CD, and becomes VSFG active. Additional evidence to support this conclusion is observed in polarization dependent VSFG analysis. A clear peak around 3050 cm^{-1} can be seen in the SSS polarization VSFG spectra, which agrees with the previous statement that adsorbed water adopt the overall symmetry of the sheets. We note this observation also agrees with recent studies showing that water networks can adopt chirality from proteins and segments of DNA.(125)

Our conclusion of strong interaction between water and host molecules agrees with existing studies. (126–130) Pioneering works in water dynamics of reversed micelles done by the Fayer, Skinner, Thompson and Pschenichnikov groups have shown that water HB network dynamics are highly dependent on the size of the reversed micelles, where the dynamics of water near the surfactants are significantly slowed down due to water-surfactant interactions.(126–128) Thus, our observation is just another manifestation of strong interactions between water and host molecules in the lattice assembly materials. Because these bounded water only adsorb at the interfaces between self-assembly and water or between components of self-assemblies, the presented work extends the capability of VSFG from studying water at flat surfaces, to rugged interfaces of self-assembly materials – areas where water could play critical role in the structures or functions of the self-assemblies.

4.4 Spatially VSFG Heterogeneity Reveal Local Hydration Level

We now focus back on what information is obtained from the spatial heterogeneity revealed by spatially resolved VSFG hyperspectral imaging in Fig. 4.1. In the optical image (Fig. 4.1 a), tens-of-micron sized domains with strong VSFG signals can be identified, each of which represents individual self-assembled sheets. We found that within each domain, spectra at different spatial points are alike, whereas spectra from different domains are qualitatively similar but quantitatively different, i.e., they all contain the same spectral components, but the intensity of these components are different in various spectra (Fig. 4.1 c, d and e). Based on OH features from the fitting results, the spectra can be grouped into two categories: one with weak secondary OH peaks relative to the primary OH peaks (A, B, C, F, H, I, J), and one with strong secondary OH peaks relative to the primary OH features (D, E, G, K). These results agree with our previous heterodyned VSFG microscope study of the CH vibrational modes: the self-assembled materials are templated and ordered within each self-assembly domain, which is the reason for strong VSFG signals.(15) However, on the ensemble-averaged level, these sheets together appear disordered, with uncoordinated alignments.

We attribute the spatially heterogeneous spectra to the variation of hydration level among different sheets. During the dehydration experiment (Fig. 4.4 c and d), the intensity ratio between secondary and primary OH peak of β-CD increases as the sample is partially dehydrated.

However, our later study shows the intensity ratio between secondary and primary OH(OD) peaks are not monotonously dependent on RH (39). When RH increases from 25% to 45%, the secondary/primary OH ratios decreases; when RH further increases from 45% to 65%, the secondary/primary ratio increases instead. Therefore, there could be multiple phase changes accompanying the RH changes, which is subject

to future study. In summary, different secondary/primary ratios only indicate different hydration level of the domain, but do not offer enough information to quantify the local hydration level.

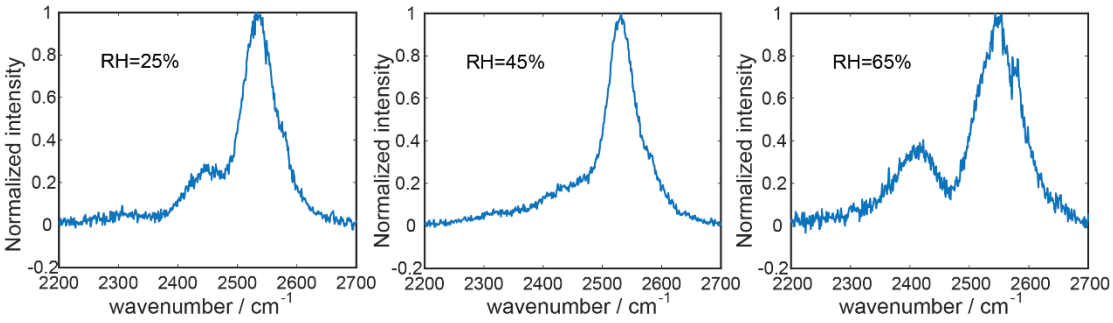

Figure 4.5. VSFG spectra of self-assembly sheets at RH=25%, 45% and 65%

Therefore, the intensity ratio between secondary and primary OH of β-CD could be indicative of local hydration level. The domains with larger secondary OH peaks (D, E, G, K) and domains with smaller secondary OH peaks (A, B, C, F, H, I, J) have different hydration level.

Chapter 4, in full, is a reprint of the material as it appears in The Journal of Physical Chemistry B, 2019. Haoyuan Wang; Wenfan Chen; Jackson Wagner; Wei Xiong. American Chemistry Society, 2019. The dissertation author was the primary investigator and author of this paper.

Chapter 5

Spatial Dependent H-bond Dynamics at Interfaces of Water/Biomimetic Self-Assembled Lattice Materials

5.1 Hydrogen bond dynamics

Hydrogen bond (H-bond) interaction is one of the key forces in self-assembled soft materials, which is a main avenue of research in synthetic biology. (3, 131–133) This field, known as biomimetics, seeks to create artificial organisms and includes two types of self-assemblies. (20, 134) The first, comprised of soft, fluidic membrane-like lipid assemblies, has been well-studied (135–137), whereas the second, rigid, crystalline lattice self-assemblies to mimic proteins, has not been investigated extensively using synthetic or non-peptide molecules. (131, 138, 139) This slow development is because delicate H-bond interaction is necessary to balance electrostatic interactions, which play critical roles in making synthetic lattice self-assemblies resemble not only the morphology but also the behavior of their biological analog in terms of flexibility, crystallinity, and chemical functionality. Recent reports discussed lattice self-assemblies formed from sodium dodecyl sulfate (SDS) and β-cyclodextrin (β-CD), referred to hereafter as SDS@2β-CD, and showed that they satisfy the criteria to mimic protein lattice self-assemblies (20, 105, 140). The authors proposed H-bonding as a key component of the strong, directional in-plane attraction force involved in maintaining 2D crystallinity. (105) Other works also demonstrated the influence of H-bond on self-healing,

proton transfer, and hydration of biomimetic materials. (141–144) For example, H-bonded water was reported to influence morphology (145) and adopt the symmetry of the self-assembly (146). To determine the principles for the better design of lattice self-assemblies, we focused on understanding the H-bond dynamics between water and self-assembled materials.

The proposed role of H-bond in SDS@2β-CD is in line with the strong H-bond interactions existing between water and host molecules in many materials and biological systems, which are critical in determining structures, dynamics, and functions of the hosts and the hydration layers. (126, 147, 148) For example, pioneering work on the water dynamics of reversed micelles performed by the Fayer, Skinner, Thompson, and Pschenichnikov groups have shown that water H-bonding network dynamics are highly dependent on the size of the reversed micelles, where the dynamics of water near the surfactants are significantly reduced due to water-surfactant interactions. (126, 147, 148) Petersen and co-workers also demonstrated that strong binding interactions allow water to adopt the local chirality of DNA. (125) Similar templating phenomena have been observed by Yan et al. in peptides. (149)

Although H-bonds have been studied in the systems mentioned above, H-bond interactions in the SDS@2β-CD system are exciting in their own right, because they are critical to the unique features of the self-assembled systems. (150) First, H-bonds and electrostatic repulsion are the only driving forces behind the self-assemblies composed of non-amphiphilic building blocks (105). Second, these interactions allow the organic components to self-assemble into a variety of morphologies, each of which possesses a biological analog with different levels of crystallinity, making it an ideal model system for synthetic biology applications. (20)

Despite its importance, H-bonding in the SDS@2β-CD self-assembly remains understudied. Based on the known structure of the self-assembly (20), there are six secondary OH molecules in each β-CD that cannot form H-bonds directly with OHs of adjacent β-CDs in the same layer, due to the far distance between them. A thermal analysis further indicated that there are, on average, 4.5 to 7 water molecules that form strong H-bonds with one β-CD (Chapter 5.10, Figure. 23), which agrees with previous studies. (151–155) Furthermore, our previous VSFG study (146), XRD and AFM-IR results (Figure. 13) all suggest that there could be heterogeneity of strongly bound water distribution in the self-assembly. Thus, the existing knowledge of strongly bound water in SDS@2β-CD begs further investigation to answer critical open questions, including What proof is there of the H-bond interactions between β-CD and water molecules? What is the difference between the H-bond dynamics of water in the self-assemblies and that of pure water, and how are strongly bound water molecules distributed in each self-assembly?

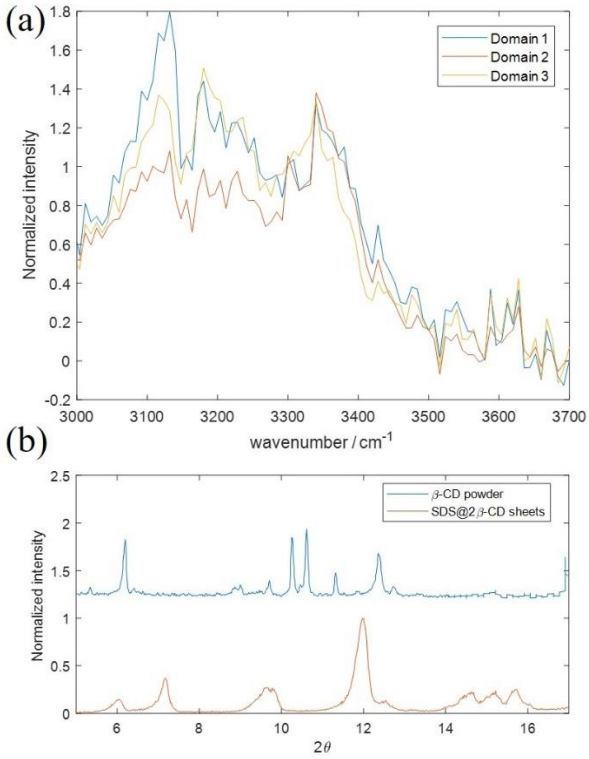

Figure 5.1. (a) AFM-IR measurements at three different domains. The ratios between ~3100 cm^{-1} and ~3350 cm^{-1} are different, suggesting different local strongly bound water concentration at these domains. (b) XRD results of lyophilized SDS@2β-CD sheets and β-CD powder. If we assume the broadening of SDS@2β-CD sheets XRD are purely from particle size, the particle size of self-assembly sheets is calculated to be 18-35 nm, which is much smaller than any dimension measured by AFM (146). Therefore, other broadening effects, such as heterogeneity, must contribute to the broadening of XRD peaks.

To answer these questions, we investigated H-bond interactions and dynamics at the water/self-assembly interfaces at the individual domain level (~1 μm) by developing the first spatially-resolved infrared (IR) pump vibrational sum-frequency generation (VSFG) probe microscope, which combines state-of-the-art VSFG microscopy (16, 25, 27, 49, 55, 95, 156) with pump-probe VSFG spectroscopy. (70, 75, 157–160) We found that relaxation dynamics are different between primary and secondary OHs of β-CD, indicating distinct H-bond environments of these OHs despite their angstrom scale proximity. Furthermore,

we observed H-bond dynamics between strongly bound water molecules and secondary OHs of β-CD, which followed a four-level-model dynamic. The relaxation dynamics of weakened water H-bond relaxation show characteristics of Förster energy transfer. (161) These dynamics of various domains range from 410 fs to 960 fs, which are longer than their counterparts of bulk water (<100 fs). (162, 163) Based on Förster energy transfer mechanism, we estimate the number of strongly bound water molecules per β-CD, thereby calculating the local hydration level in each domain. The local hydration levels in self-assembly sheets are different between domains but uniform within domains. Such a detailed understanding of the H-bonded water and its dynamics in this system opens doors for future materials engineering and applications of biomimetic self-assemblies.

5.2 Pump-probe technique

In the pump probe (transient) VSFG, an intense IR pump first interacts with the sample and excites the vibrational modes from ground state to vibrational state. After a certain time delay, the difference spectra with and without pump are measured (75, 164). Because some portions of the molecules are excited to first excited state by the pump, the excitation from $\nu = 0$ to $\nu = 1$ in SFG process is reduced, which gives rise to the ground state bleach (GSB) signal. On the other hand, since some molecules are at first excited state, there is $\nu = 1$ to $\nu = 2$ in SFG process, which gives rise to the excited state absorption (ESA) signal. However, the ESA signal will be very small in homodyne detection due to the absolute square nature (164).

5.3 Dynamics of OHs of β-CD

When water is strongly bounded to self-assembled materials, there are two possible changes to water dynamics. First, the templated water network H-bond dynamics could be different from bulk water, which is known to have fast energy dissipation. (165) Second, heterogeneity in the self-assembly host materials could ultimately lead to spatial heterogeneity in H-bond dynamics at water/SDS@2β-CD interfaces. To examine whether such changes exist, we carried out spatially resolved ultrafast measurements.

When excited by IR pulses, three distinct transient features are observed in the OH spectral regime. As shown in Figure 5.3, the two higher frequency features are related to OHs of β-CD, which we will discuss first. In Fig. 5.3 a and c, we plot the two most representative pump-probe dynamics of the OH spectral features (from domains A and E of Figure 5.2 a), with the dynamics of the remaining domains in Fig. 5.3 a summarized in Chapter 5.7. The primary OH peak is bleached, shown as negative dynamics at 3350 cm^{-1} in Figs. 5.3 a and c, and it lasts longer than 1.8 ps – the longest time delay scanned. The negative bleach dynamic is caused by removing the primary OH population from the ground vibrational states. Since the bleach dynamics for the primary OH of all domains exhibit long lifetimes (see Chapter 5.7), it indicates that the primary OH for all sheets experiences similar isolated or weak/no H-bond environments, leading to slow energy relaxation. (166)

Secondly, in some spots, the secondary OH peak near 3280 cm^{-1} also has a short-lived bleach dynamic (Fig. 5.3 c) with a lifetime of 280–400 fs. The fast decay dynamics suggest that secondary OH can quickly dissipate its energy into the environment, agreeing with its H-bonded nature. However, the intensity and existence of the secondary OH dynamics vary significantly from spot to spot (see Fig. 5.2 a and Chapter

5.7). This variation is likely correlated to the intensities of the secondary OH static VSFG peak. For example, domains A/B/C/K do not have the bleached secondary OH dynamics, and in the static VSFG spectra, the secondary OH signals in these domains are small as well.

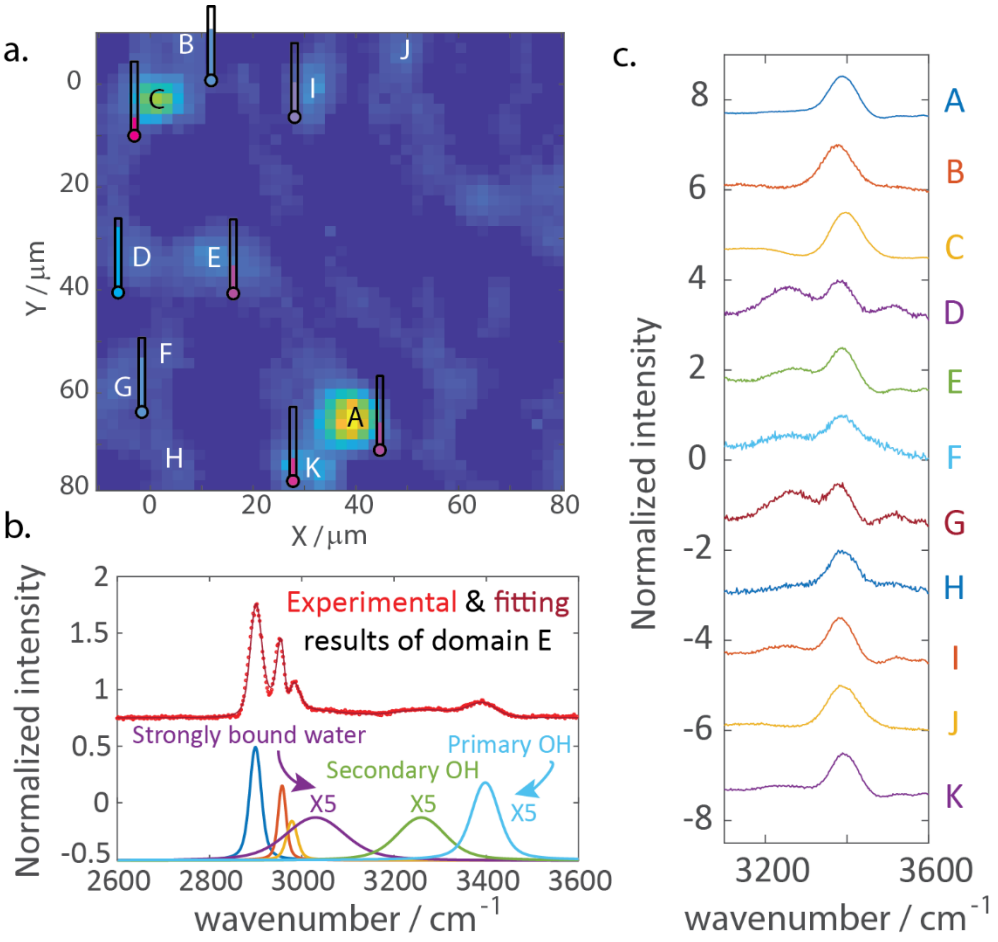

Figure 5.2. (a) VSFG intensity image (PPP polarization) for the OH region of molecular self-assembled micron sheets. The hygrometer next to each domain represents the relative hydration level determined in table 5.1. (b) A representative VSFG spectrum from domain E and its spectral fitting reveals that there are three CH peaks and three OH peaks, which correspond to strongly bound water, secondary and primary OH from β-cyclodextrin, respectively. (c) Individual zoomed-in spectra for OH region. All spectra have been normalized to their maximum and have been offset vertically for better visualization.

The drastically different dynamics of primary and secondary OHs indicate distinct local

environments. Comparing to the secondary OHs, the primary OHs are at the narrower rim of β-CDs, and therefore the distances between primary OHs from adjacent β-CDs are much larger. This distance difference could make the formation of primary OHs-water bridges less likely. Also, assuming their distance is approximately the depth of β-cyclodextrin, then the primary and secondary OHs are separated by about 0.8 nm, which highlights the proximity of this ordering. This contrast suggests that upon self-assembling, the hydrogen-bond network is so ordered that water is templated precisely near secondary OHs of β-cyclodextrin. Thus, despite the proximity of the two OH groups, they could have very different local environments, which, from a biochemical perspective, could enhance proton transfer and be necessary for functions of natural and artificial biological systems and influence membrane dipole potentials. (167)

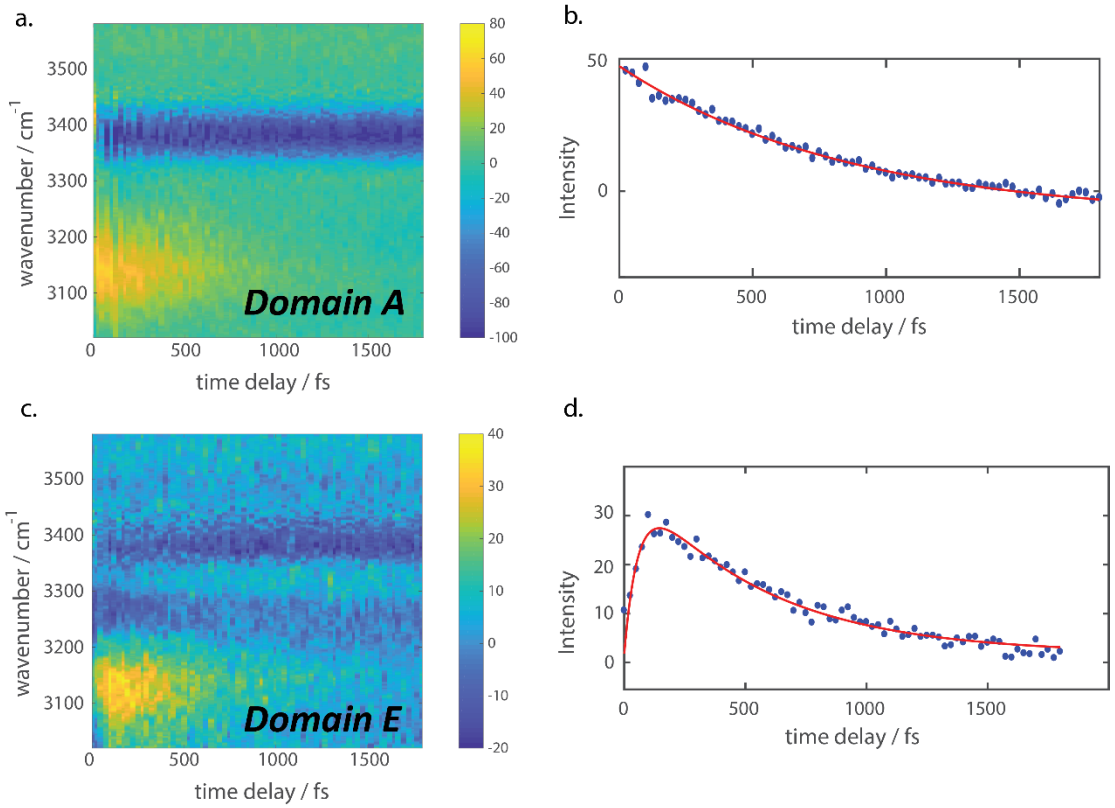

Figure 5.3. Two representative types of vibrational dynamics. (a) Domain A has long-lasting bleach dynamics for primary OH from β-cyclodextrin and has a positive signal for water OH, which shows a monotonical decay (as shown in (b)). (c) Domain E has long-lasting bleach dynamics for primary OH from β-cyclodextrin, a short-lived bleach dynamic for secondary OH from β-cyclodextrin, and a positive signal for water OH in a delayed fashion (as shown in (d)). (b) and (d) are the integrated signal for the strongly bound water OH frequency region near 3150 cm^{-1}.

5.4 Dynamics of H-bond weakening and restoration

Finally, we focus on the positive transient peak at ~3150cm^{-1}, which is associated with the OH feature of strongly bound water. There are two interesting features worth noting about this dynamic. First, the dynamic signal is positive, and, second, the peak center blueshifts from ~3050 cm^{-1} (obtained from static VSFG measurements) to ~3150 cm^{-1}. The nature of the positive peak is realized by a narrow-band IR pump VSFG probe, using IR filters to pump different OH modes selectively. By selectively pumping the primary OH mode (Filter 3), no pump-probe dynamics are observed while, when all modes except the primary OH are pumped (Filter 1), similar dynamics are observed near ~3150cm^{-1}. These results conclude that the

positive dynamics are not related to the primary OH. In addition, when all modes except the primary and secondary OH are pumped (Filter 2), a small positive dynamic is observed. These experiments, summarized in Fig. 16, indicate that the positive dynamics can be attributed to the excitation of the secondary OH, while similar but weaker intensity dynamics are observed when pumping strongly bound water. (The possibility of overtone peaks of secondary OH and interferences are also examined and excluded. (See Chapter 5.9).

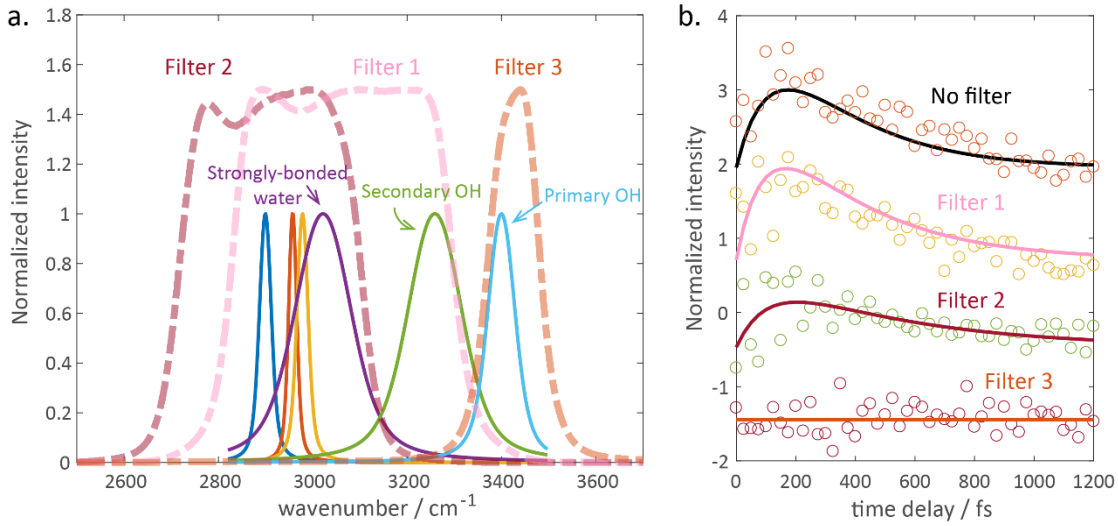

Figure 5.4. (a) Spectral coverage of the three filters in the narrow-band pump VSFG probe experiment. (b) Dynamic traces of the strongly bound water peak with different selective filters from the same spatial point. The pump power intensity variation is considered, and all the dynamics' intensities are normalized to the one without any filter. Filter 1 dynamics are nearly the same as the dynamics without any filter, while Filter 3 does not show any signal. Filter 2 shows a weak positive dynamic.

Since the positive dynamic peak at ~3150 cm^{-1} is blueshifted relative to the strongly bound water OH peak at ~3050 cm^{-1}, we can assign it to a weakening of the H-bond between water and the secondary OH of SDS@2β-CD. This assignment agrees with the fact that both peaks have mixed origins from water and the secondary OH. Therefore, when either or both modes are pumped, H-bond weakening is observed. We note the blueshift should also generate a transient negative signal appearing at 3050 cm^{-1}, which is very small due to the pseudo-heterodyne detection (see Chapter 5.5).

We performed a spatially resolved transient VSFG experiment on deuterated SDS@2β-CD to further understand the mechanism behind the positive dynamics seen at ~3150 cm^{-1}. The results (Fig. 5.5)

agree with the OH dynamics (Fig. 5.3). The transient features of the deuterated samples match well with the non-deuterated sample, with the negative peak at ~2540cm^{-1} corresponding to the primary OH of SDS@2β-CD, which has a long lifetime, and the positive peak at 2400 cm^{-1} corresponding to the weakening/fluctuation of the H-bond, which shows a relatively short-lived dynamic. Only domain OD1 has a short-lived bleach dynamic of secondary OH – consistent with the observation for the non-deuterated samples.

A quantitative comparison between the deuterated and non-deuterated system can help elucidate the nature of the H-bond weakening and recovery dynamics. All positive H-bond dynamics measured at different spatial domains were fitted and are summarized in Table 5.2 (see Chapter 5.7 for full lifetimes). Statistically, we found that deuteration does not affect the weakening dynamics significantly (rising dynamics, t_1), while deuteration drastically slows the relaxation dynamics. In the H-bond dynamics of water systems, fast dynamics within 150 fs are attributed to H-bond fluctuations through hindered translation motions, e.g., increase of O-O bond distance. (168–171) The fact that the H-bond weakening dynamic seen here is insensitive to deuteration implies that a similar O-O bond elongation mechanism could be responsible for the H-bond weakening.

In contrast, deuteration slows the relaxation dynamics by about twice. Such an effect suggests that the relaxation involves Förster energy transfer, which exists in water systems where OH modes of water are closely overlapped. (162, 172) The energy transfer rate was also determined to be about 2.3 times more efficient for the OH band than the OD band due to the difference in transition dipole moments (173), which agrees with our experimental observation as well. Contributions from other dynamics, i.e., wobbling-in-a-cone and energy transfer to CH modes, are excluded (see Chapter 5.9 for details).

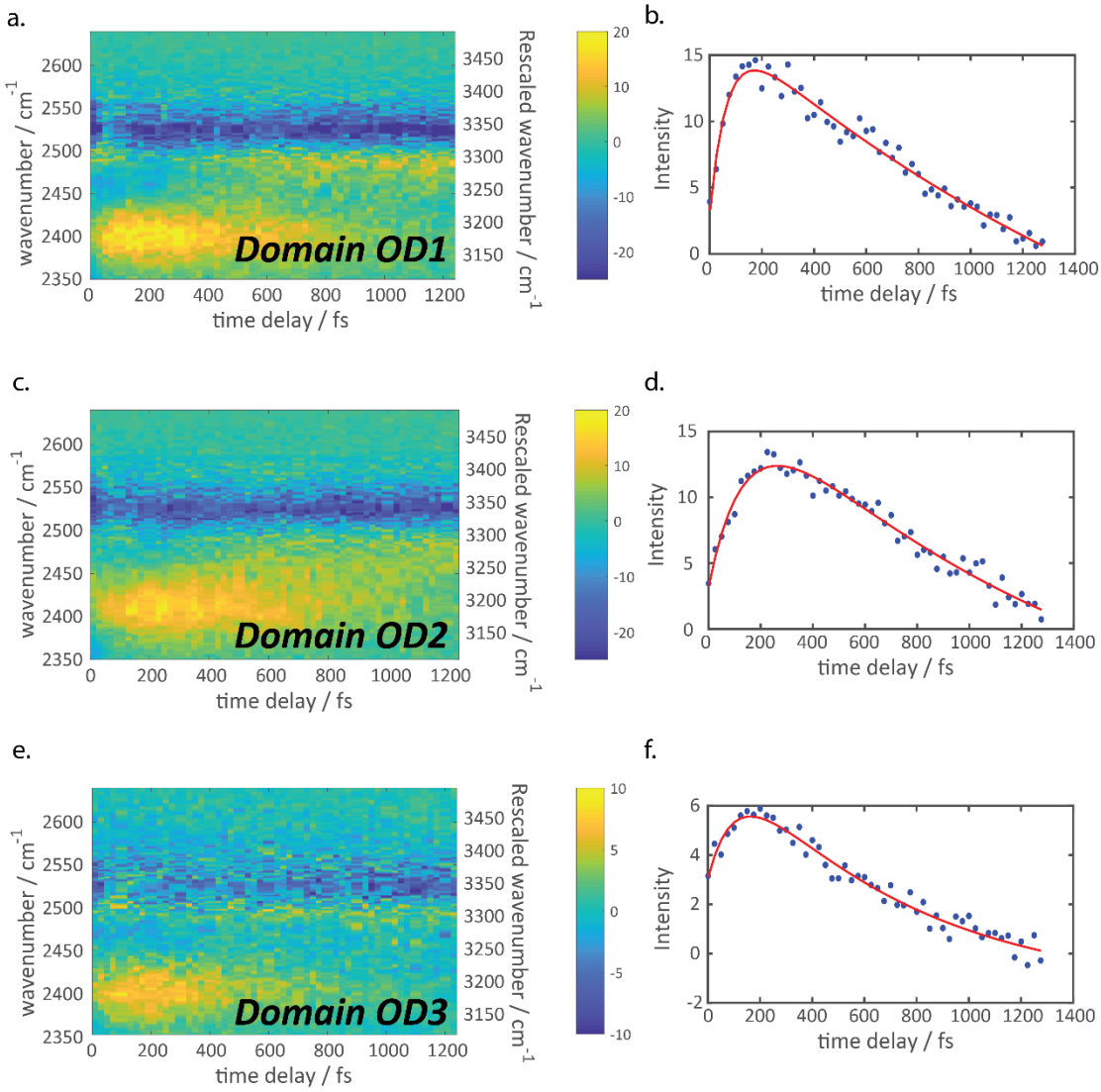

Figure 5.5. (a), (c), and (e): Dynamics traces from the deuterated SDS@2β-CD sample in the OD region. Y-axis on the right is the rescaled frequency using a ratio of 0.755, slightly different from the ratio in the gas phase (0.742) due to anharmonicity. (b), (d) and (f): integrated positive dynamics signal from the corresponding dynamics trace.

Table 5.1. The dynamic lifetimes fitted by a bi-exponential model: t_2 is H-bond relaxation lifetime, from which we calculated relative hydration level (details in Chapter 5.6)

Domain	t_1 / fs	Apparent t_2 / fs	Corrected t_2 / fs	Relative hydration level
OH dynamics				
A	NA	832±81	708±45	2.64
B	NA	456±25	468±18	4.04
C	141±31	770±67	958±74	2.14
D	48±8	359±64	410±66	5.11
E	68±9	594±98	659±92	2.76
G	40±10	408±69	452±65	4.35
I	NA	562±40	542±27	3.26
K	91±3	730±16	827±16	2.38
OD dynamics				
OD1	70±4	1640±530	1358±291	2.94
OD2	150±4	1270±470	1375±347	2.92
OD3	106±4	690±28	820±29	5.67

Combining all experimental observations, we adopt the existing four-level model (159) developed for ultrafast water vibrational dynamics to describe the H-bond vibrational dynamics at water/SDS@2β-CD interfaces (Fig. 5.6): The IR pulse first excites the secondary OH of β-CD or OH groups of strongly bound water. OH then transfers its energy to the surrounding H-bond network, resulting in an H-bond elongation coupled with a reduction in bond strength. The weakened H-bond is restored to its original

strength by transferring additional energy to its surroundings through Förster resonant energy transfer processes. We further simulate the spectral dynamics based on the four-level model (see Chapter 5.5). The simulated dynamics of the positive signal at ~2400 cm^{-1} (Fig. 5.7) match well with experimental results, validating the four-level model to describe the H-bond dynamics in this system.

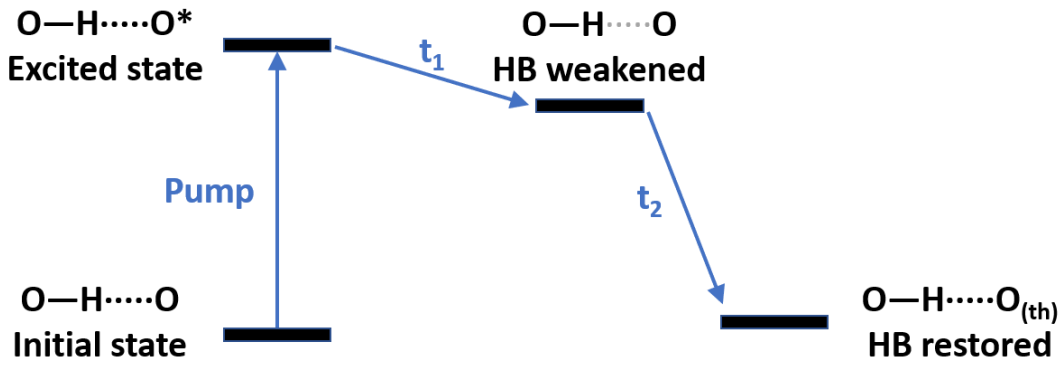

Figure 5.6. The four-level model that describes the OD (OH) dynamics in self-assembly.

Despite the fact that H-bond dynamics manifest as 2D spectral dynamics, we found the 1D dynamics at ~2400 cm^{-1} in Figure 5.4 (and ~3150 cm^{-1} for OH in Figure 5.2) can still accurately capture the actual H-bond dynamics. We confirmed it by fitting the dynamics at ~2400 cm^{-1} of a set of 2D spectral dynamics, which are modeled by bi-exponentials, in which t_1 and t_2 describe the initial weakening and relaxation process, respectively, in the four-level model (see Chapter 5.5 for details). We found that despite the fitted t_1 and t_2 and the original t_1 and t_2 being different, they had a one-to-one relationship. Therefore the dynamics at ~2400 cm^{-1} are a decent descriptor of the H-bond dynamics. The relationship is summarized as Table 5.2 and was used to extract the original H-bond dynamics from the apparent dynamics. The H-bond relaxation lifetime t_2 was found to range from 410 to 960 fs (Table 5.1), which is slower than Förster energy transfer rate in bulk water (<100 fs) or ice (300 fs). (162, 163) The slower transfer efficiency of OH in the confined environment could come from the lower mode density and less spectral overlapping that occurs between water and OH of β-CD compared to that seen between waters.

5.5 Simulation using a 4-level model

The 4-level model is used to describe the OH dynamics in self-assembly (Fig. 5.6). It involves:

(1) the pump pulse excites the hydrogen-bonded water and secondary OH of β-CD into the first excited vibrational state, which causes a redshift of the excited state absorption due to anharmonicity (not observed, because it is beyond our spectral coverage), and a bleach (negative) signal at the original peak position.

(2) Then, the energy relaxes to weaken the hydrogen bonds, causing the bleach signal decays, and a blueshifted VSFG strongly bound water OH peak, appearing as a positive feature in the transient spectra.

(3) Lastly, the hydrogen bonds restore by relaxing extra energy through Forster energy transfer.

Based on the 4-level model, we simulate the observed dynamics by describing each absorption feature using a Voigt function. We focus on reproducing the deuterated experiment spectral dynamics, as it has no interference from CH peaks. The transient VSFG spectra is simulated based on the following equations:

$$D(\omega_{\mathrm{IR}}, t) = I_{on}(\omega_{\mathrm{IR}}, t) - I_{off}(\omega_{\mathrm{IR}})$$

$$I_{off}(\omega_{\mathrm{IR}}) = |P_{\mathrm{water,\ off}}(\omega_{\mathrm{IR}}) + P_{\mathrm{1st\ OH,\ off}}(\omega_{\mathrm{IR}}) + P_{\mathrm{2nd\ OH,\ off}}(\omega_{\mathrm{IR}})|^2$$

$$I_{on}(\omega_{\mathrm{IR}}, t) = |P_{\mathrm{water,\ on}}(\omega_{\mathrm{IR}}, t) + P_{\mathrm{1st\ OH,\ on}}(\omega_{\mathrm{IR}}, t) + P_{\mathrm{2nd\ OH,\ on}}(\omega_{\mathrm{IR}}, t)|^2$$

$$P_{\mathrm{water,\ on}}(\omega_{\mathrm{IR}}, t) = \int \frac{A_{\mathrm{water}}(t)}{\omega_{IR} - \omega_L + i\Gamma_L} \times e^{-((\omega_L - \omega(t))/\Gamma_{G,water})^2}\, \mathrm{d}\omega_L$$

$$P_{\mathrm{1st\ OH,\ on}}(\omega_{\mathrm{IR}}, t) = \int \frac{A_{\mathrm{1st\ OH}}(t)}{\omega_{IR} - \omega_L + i\Gamma_L} \times e^{-((\omega_L - \omega_{1st\,OH})/\Gamma_{G,1st\,OH})^2}\, \mathrm{d}\omega_L$$

$$P_{\mathrm{2nd\ OH,\ on}}(\omega_{\mathrm{IR}}, t) = \int \frac{A_{\mathrm{1st\ OH}}(t)}{\omega_{IR} - \omega_L + i\Gamma_L} \times e^{-((\omega_L - \omega_{2nd\,OH})/\Gamma_{G,2nd\,OH})^2}\, \mathrm{d}\omega_L$$

$$A_{\mathrm{1st\ OH}}(t) = (1 - B_{\mathrm{1st\ OH}} \cdot e^{-t/T_{\mathrm{1st\ OH}}}) A_{\mathrm{1st\ OH,\ off}}$$

$$A_{\text{2nd OH}}(t) = (1 - B_{\text{2nd OH}} \cdot e^{-t/T_{\text{2nd OH}}})A_{\text{2nd OH, off}}$$

$$\omega(t) = \omega_{off} + S \cdot e^{-t/T_2} \quad (1)$$

$$A_{\text{water}}(t) = \left(1 - B \cdot e^{-t/T_1}\right)A_{\text{water, off}} \quad (2)$$

where $D(\omega_{\text{IR}}, t)$ is pump probe dynamics signal, $I_{on}(\omega_{\text{IR}}, t)$ and $I_{off}(\omega_{\text{IR}})$ are VSFG signal with pump on/off; $P(\omega_{\text{IR}})$ is the Voigt profile, which is the convolution between Lorentzian and Gaussian profile. $A_{\text{water, off}}$ and ω_{off} are the amplitude and center resonant frequency of strongly bound water at equilibrium, respectively. ω_L, Γ_L, Γ_G are the center frequency of each individual Lorentzian, individual Lorentzian line width (due to homogeneous broadening) and Gaussian line width (due to inhomogeneous broadening), respectively, and these parameters are obtained by fitting the linear VSFG experimental spectra. Similar Voigt profiles also apply to primary OH and secondary OH of β-CD.

Term (2) represents the initial bleach by IR excitation, and term (1) represents the blueshift due to H-bond weakening and T_2 represents the Forster energy transfer dynamics lifetime. $A_{\text{water}}(t)$ and $\omega(t)$ are the time-dependent amplitude and center resonant frequency of strongly bound water, after being excited, and S and B are the amplitude of peak shift and intensity change. T_2 are the lifetimes of peak shift due to Forster energy transfer, and T_1 are the lifetime for initial excited OH. Furthermore, we also considered ground state bleach for the other two OH modes from β-CD. Finally, we included peaks that do not directly involved in the dynamics in the simulation for reproducing the pseudoheterodyne effect – despite homodyne detection is used experimentally, the broad VSFG spectra from multiple peaks makes transient features interfere with them and get amplified.

We found that the 4-level model (Fig. 5.7 A) can well reconstruct the observed dynamics (Fig. 5.7 B), including the positive signal shape and the negative signal shape. To evaluate whether all components in the model are necessary, we further turn off certain dynamics/effects in the simulation equation. When the initial bleach is turned off, not only the negative feature at lower frequency become small and its lifetime does not match with experimental results (Fig. 5.7 C); If we turn of pseudoheterodyne, neither of the

dynamics cannot be observed under the same colorbar (Fig. 5.7 D). We note the intensity difference between the positive and negative feature is also due to pseudoheterodyne. The negative dynamics at lower frequency has poorer spectral overlap with other peaks, than the positive dynamics at higher frequency side, and therefore the positive dynamics are amplified more than its negative counterparts. Therefore, this comparison validated that each step in the 4-level model is necessary to properly account the observed dynamics.

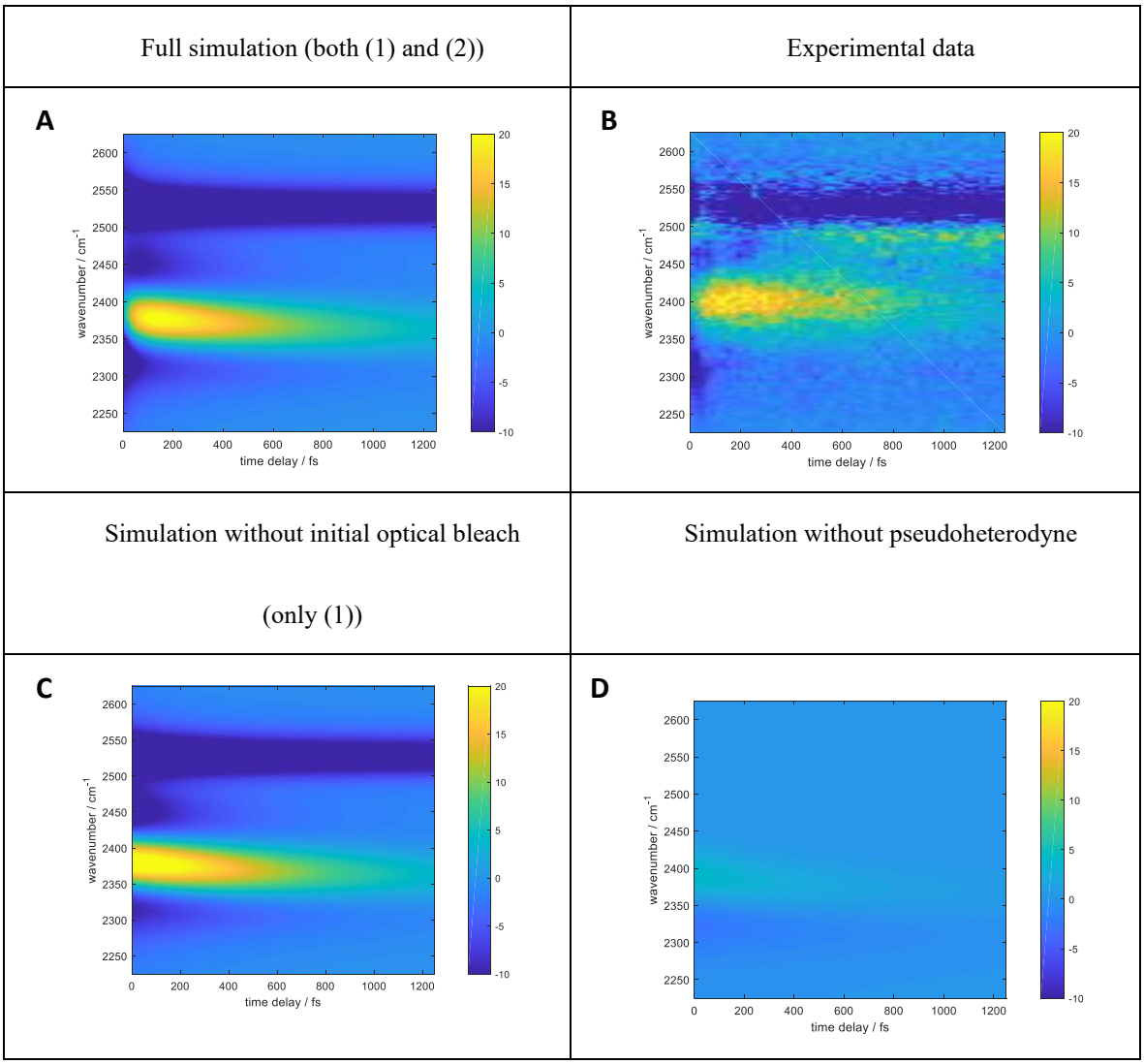

Figure 5.7. 4-level model can well reconstruct the observed dynamics, which means the initial bleach and peak shift both play an important role in the dynamics. If we do not consider the initial bleach (C), the positive feature and the negative feature do not show similar shape as the experimental data anymore. If we do not consider any peaks other than strongly bound water peak, the dynamics is hardly to be seen using the same colorbar (D). It means the pseudoheterodyne effect is also important.

Next, we examine whether the 1D dynamics at 2400 cm^{-1} can reflect the 4-level model well. To do so, we simulate a set of OH dynamics using the 4-level model, with different T_1 and T_2. Then, we fit the dynamics cut at 2400 cm^{-1} with bi-exponentials. The input and output T_1/T_2 are summarized in table 5.2. The fitted output T_1 is very close to original input T_1, while the fitted output T_2 is off from the input and the amount of offset depends on T_1.

We use table 5.2 to correct this discrepancy between the real (input) and apparent (output) lifetimes. For example, when the experimental dynamics is fitted as 60 fs and 810 fs, by looking up the table, we can find the apparent lifetime corresponds to the real lifetime of 50 fs and 800 fs in the 4-level system. Therefore, under the correction using Table 5.2, the spectral dynamics at ~2400 cm^{-1} can describe the dynamics of 4-level model well, and we will use this method to extract the actual dynamics of the systems.

Table 5.2. Correction table between fitted output and original input lifetimes

Input T_1 / fs	Input T_2 / fs	Output T_1 / fs	Output T_2 / fs
50	400	52	350
50	600	58	550
50	800	60	810
50	1000	60	1150
70	400	68	340
70	600	77	530
70	800	81	750
70	1000	83	1025
90	400	83	340
90	600	95	510
90	800	100	700
90	1000	105	935
110	400	100	330
110	600	110	490
110	800	121	670
110	1000	125	860
130	400	110	330
130	600	130	480

Table 5.2. Correction table between fitted output and original input lifetimes (Continue)

130	800	140	630
130	1000	150	810
10	400	12	370
10	600	13	640
10	800	13	1020
10	1000	13	1670

5.6 Model Connecting Macroscopic Dynamics with Microscopic Structure

Due to the heterogeneity and the average number of strongly bound water in a single self-assembly unit, we propose that there is the heterogeneity of the strongly bound water number in different domains. With the different number of water molecules occupying the same cavity, the distance between water molecules and nearby OH groups should be different. The difference in donor-acceptor distances would give rise to the heterogeneity of H-bond restoration lifetime (t_2).

We proposed a model to demonstrate this water density difference can give rise to the restoration lifetime difference in the experiment. We start our model by assuming that water resides in positions to make the total energy to be lowest. The potential of the hydrogen bond is modeled using Morse potential(174), with r_e to be 2.7 Å, which is the average distance between water and saccharides(175). The optimized geometric arrangement of water in self-assembly, under 2-water to 6-water limits, are shown in Fig. 5.8. We then use the equation 3&4 to determine the Forster energy transfer lifetime.

$$k_F = \frac{1}{\tau_D}\left(\frac{R_0}{r}\right)^6 \qquad (3)$$

$$T_2 = \frac{1}{\sum k_F} \qquad (4)$$

Where R_0 (the Forster distance) is 2.3 Å(173), τ_D (OH lifetime) is 740 fs (173), r is the distance between donor and acceptor.

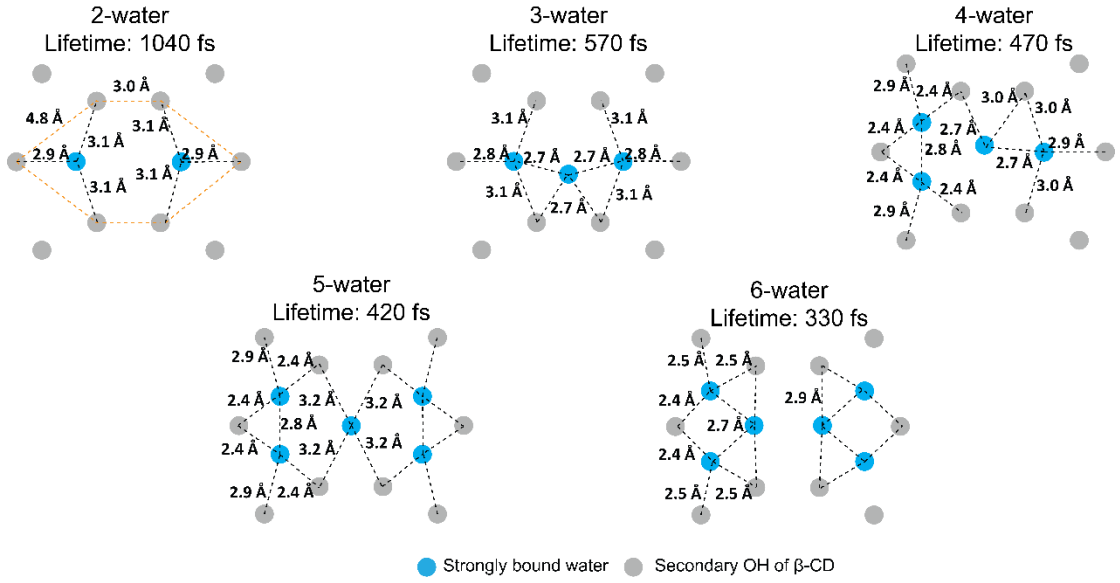

Figure 5.8. The geometric arrangement of water in self-assembly calculated from model, under 2-water to 6-water limits. The distances are estimated from SDS@2β-CD structure. The black dashed lines represent the nearest neighbor to have Forster energy transfer.

We also simulated dynamics of domains with a mixture of two lifetimes and found that bi-exponential fitted the mixture dynamics well, with only one t_2 to account for the Forster energy transfer H-bond restoration. The t_2 is between the t_2 of those two input lifetimes. Phenomenologically, the fitted t_2 matches well the geometric mean of the two inputs determined by the relation percentage of the two inputs in a domain (Figure. 5.9). For example, $\overline{t_2} = {\tau_a}^{x_a}{\tau_b}^{x_b}$, where τ_a and τ_b are t_2 lifetimes of the two inputs, x_a and x_b are the percentages.

Based on the calculation, the Forster energy transfer lifetimes are 1040 fs for the 2-water limit, 570

fs for the 3-water limit, 470 fs for the 4-water limit, 420 fs for the 5-water limit and 330 fs for the 6-water limit, respectively. Based on literature (173), the transfer lifetimes of OD are 2.3 times of OH for each case. These results qualitatively agree with experimental measurements, as all measured lifetimes are in between the lifetime of 2- to 6- water limits, suggesting the strongly bound water distribution is in between the two limits. To calculate the water density of each domain, we first determine the experimental result falls into which two limits, and later we use the geometric mean model to calculate the relative population. For example, domain A lifetime is 708 fs, which is in between 2-water and 3-water limits. Using the geometric mean model, we calculate there are 36% of the 2-water limit and 64% of 3-water. Therefore, we report the relative hydration level of domain A as 2*0.36+3*0.64 = 2.64.

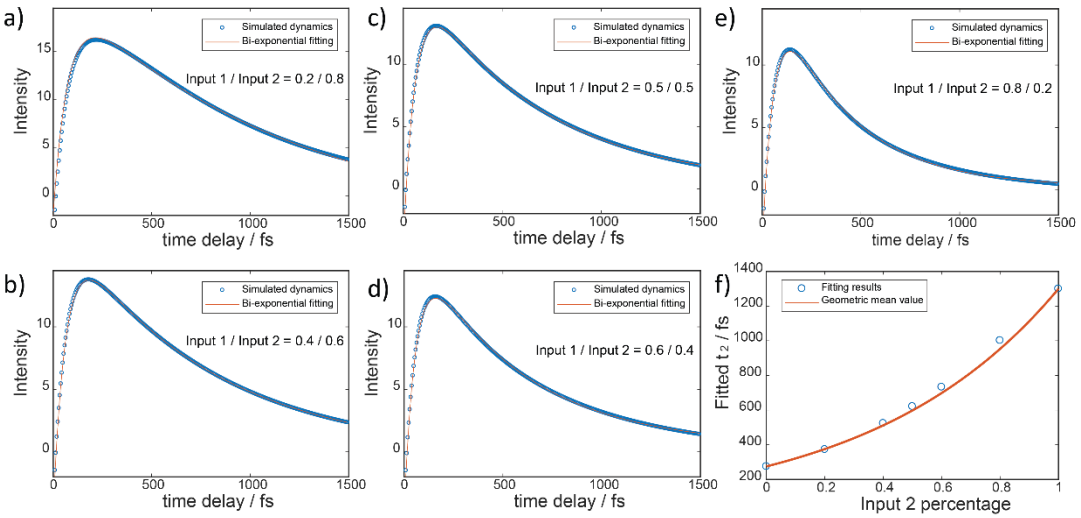

Figure 5.9. By mixing 2- and 3- water limits together with different ratios ((a) 20%/80%; (b) 40%/60%; (c) 50%/50%; (d) 60%/40%; (e) 80%/20%), all the simulated dynamics fit well using bi-exponential model. (f) The fitted t_2 lifetimes match well with the geometric mean value of two limits.

5.7 Dynamics of specific spatial points in each domain

The apparent dynamic lifetime is the fitting result from the single/bi-exponential model. To correct the apparent lifetime to the lifetime of the actual dynamics, we used a correlation table in Chapter 5.6.

Pump-probe dynamics	Integrated dynamics of strongly bound water	Apparent lifetime and corrected t_2 (fs)
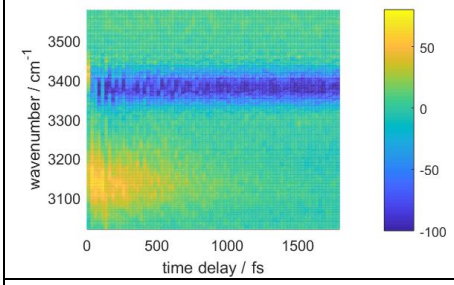	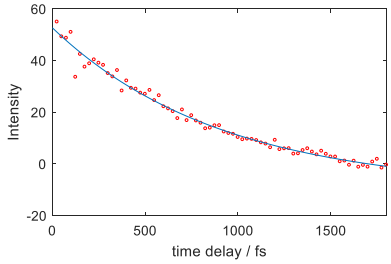	Apparent 774±112, 889±235 (Corrected 676, 739)
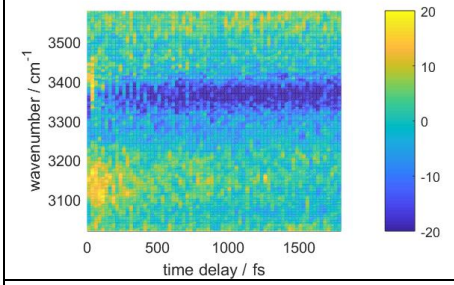	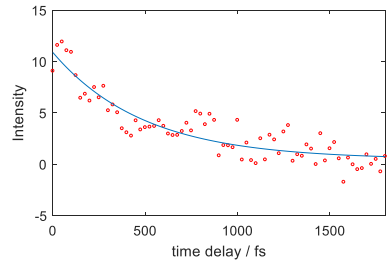	Apparent 439±182, 474±220 (Corrected 455, 481)
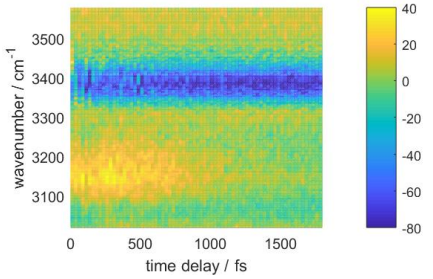	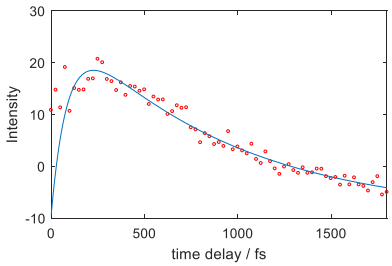	Apparent 163±31 / 723 ±185, 119±77 / 818 ±511 (Corrected 163/905, 119/1010)

Figure 5.10. Pump-probe scan signals and integrated intensity dynamics for each domain. The dynamic lifetime is fitted into single/bi-exponential and then corrected using the model developed in Table 5.2. For the single exponential data, we assumed t_1=10 fs data for the correction.

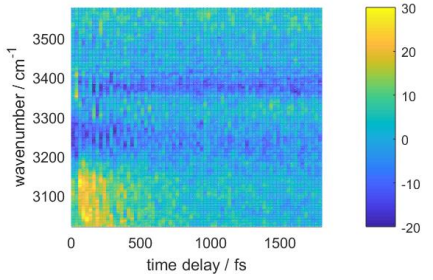	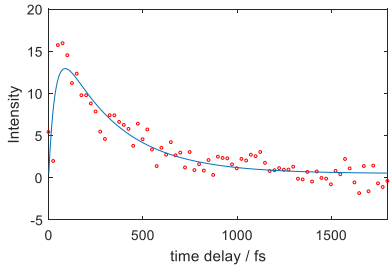	Apparent 53±40 / 404 ±142, 42±28 / 314 ±92 (Corrected 53/457, 42/364)
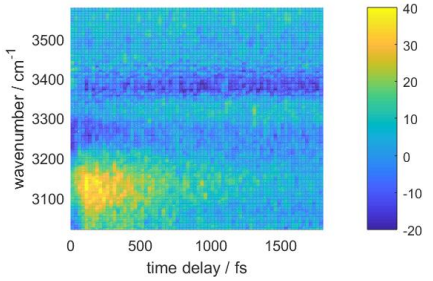	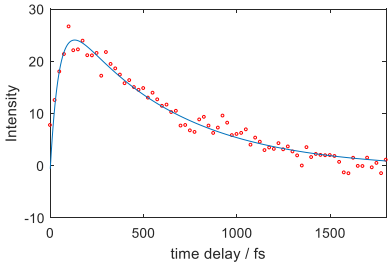	Apparent 75±27 / 524 ±143 62±24 / 663 ±180 (Corrected 75/594, 62/724)
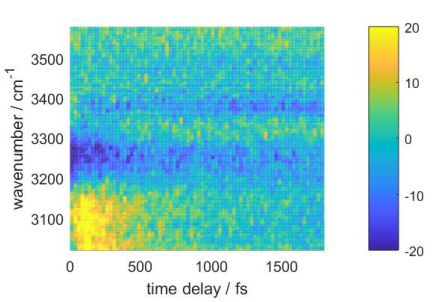	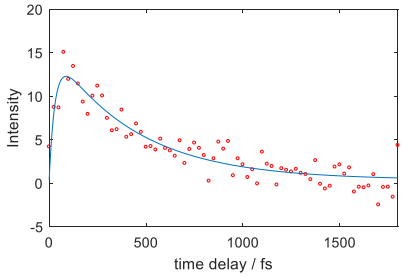	Apparent 33±27 / 457 ±130 47±24 / 359 ±85 (Corrected 33,498 47,406)
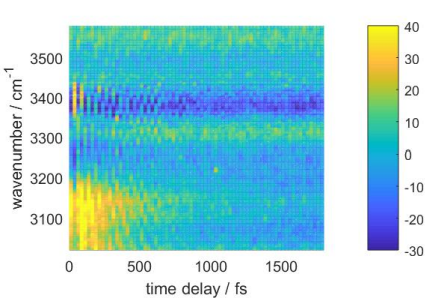	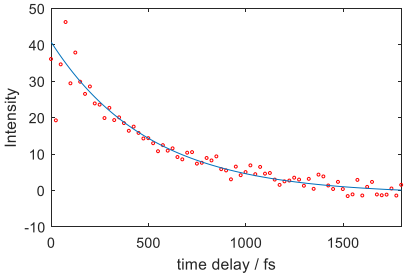	Apparent 533±118, 590±93 (Corrected 523, 561)

Figure 5.10. Pump-probe scan signals and integrated intensity dynamics for each domain. The dynamic lifetime is fitted into single/bi-exponential and then corrected using the model developed in Table 5.2. For the single exponential data, we assumed t_1=10 fs data for the correction. (Continue)

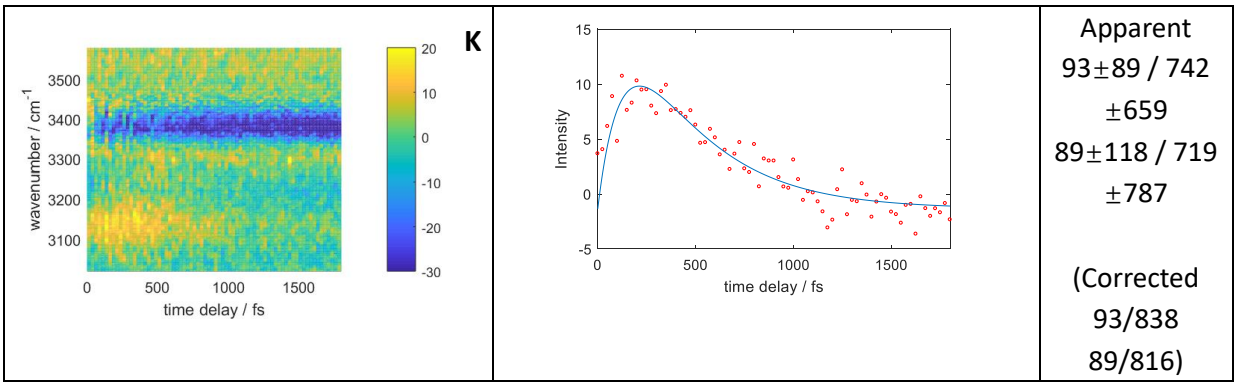

Figure 5.10. Pump-probe scan signals and integrated intensity dynamics for each domain. The dynamic lifetime is fitted into single/bi-exponential and then corrected using the model developed in Table 5.2. For the single exponential data, we assumed t_1=10 fs data for the correction. (Continue)

For each domain (Figure. 5.10), the dynamics reproduce themselves well between two scans. For A/B/I, the positive peak decays monotonically, so only one value is shown to describe the lifetime. For others, the positive peak appears in a delayed fashion. Therefore, a bi-exponential model is used to fit the dynamics, and the two numbers represent lifetimes of each step. F/H/J that do not have a good signal-to-noise ratio for these transient features.

5.8 Domain-dependent H-bond Dynamics

Next, we examine the spatial heterogeneity of the H-bond dynamics at ~3150 cm^{-1}. From Fig. 5.3, we present the most extreme case found in domains A and E (Figs. 5.3 a and b; other results are shown in Chapter 5.7). In this extreme case, the positive peak appears immediately after excitation and decays monotonically in domain A. In domain E, however (Figs. 5.3 c and d), the positive peak appears in a delayed fashion. Similar spatially heterogeneous dynamics are observed in deuterated samples, as they all rise and decay at different rates (Fig. 5.5). We carefully quantified the measurement's uncertainty and ruled out temporal artifacts (a variation of +/- 12 fs) by measuring time-zero through third-order signal. Thus, the observed heterogeneous dynamics reflect domain-specific H-bond dynamics.

The fitting results using the bi-exponential function (Table 5.1) quantify the domain-specific H-bond dynamics. For the regular (deuterated) sample, the H-bond weakening dynamics range from

instantaneous to 140 fs (70 to 150 fs), while the relaxation dynamics range from 410 fs to 960 fs (820 fs to 1.4 ps). Based on the four-level model and theoretical study from Hynes, the variation of H-bond weakening dynamics suggests a variety in H-bond strength. (170)

We then focus on modeling the relaxation dynamics because it is related to the amount of local strongly bound water. To do so, we built a model that correlates the relaxation dynamics with the number of strongly bound water (see Chapter 5.6). The model assumes that the hydration level of individual β-CD fluctuates between 2 to 6 water molecules, and water is at equilibrium (lowest energy calculated from a hydrogen bond potential), from which we calculate the OH-OH distance at different hydration levels. We further calculated the hydration-level-specific Förster energy transfer rate based on the OH-OH distances and known Förster energy radius and OH lifetime. We found from 2 to 6 strongly bound water molecules per β-CD molecule, the relaxation lifetime spans from 1.04 ps to 330 fs, and if a domain has a mixture of a different density of strongly bound water, the measured t_2 is the geometric mean of those two limits. Based on this empirical relationship, we summarize the hydration level of each domain in Table 5.1 and Figure 5.2 a. The relative hydration level ranges from 2.1 to 5.7 water molecules per β-CD molecule, which suggests the actual hydration of strongly bound water per β-CD is strongly domain-specific. A possible driving force of such local hydration heterogeneity could be the lattice structure variations of different domains (e.g. small variations of secondary OHs distances or the hexagonal exterior cavity angles). Such a detailed insight into local hydration of the self-assembled materials cannot be gained from static VSFG imaging measurements. (176)

Another stunning contrast is that both spectra and dynamics of different areas within an individual domain are similar. This contrast means there are similar H-bond coupling strength and hydration levels within domains. This intriguing observation implies that the mesoscopic arrangement of each SDS@2β-CD domain governs the H-bond interactions and strongly bound water arrangement at water/SDS@2β-CD interfaces. This observation is a mesoscopic analog of the microscopic water-host interaction observed in water-ion and water-reverse micelle clusters where water dynamics vary based on the specific water-ion

pair (177) or the specific location of water in the reverse micelle. (126, 147, 148)

5.9 Excluding Other Models

5.9.1 Alternative models for fitting VSFG spectra

The positive signal could come from the interference. However, in that scenario, the peaks need to have significant amount of overlap. In our fitting results, the overlap between the strongly bound water peak and secondary OH peak is minimal. The overlap is also small in the OD region experiment. If we force the peak to be broad enough for more significant overlap such that interference is generated, the model fits poorly (Fig. 5.11). The maximum difference between fitting and experimental is about 40 counts, which is comparable to our pump-probe signal intensity.

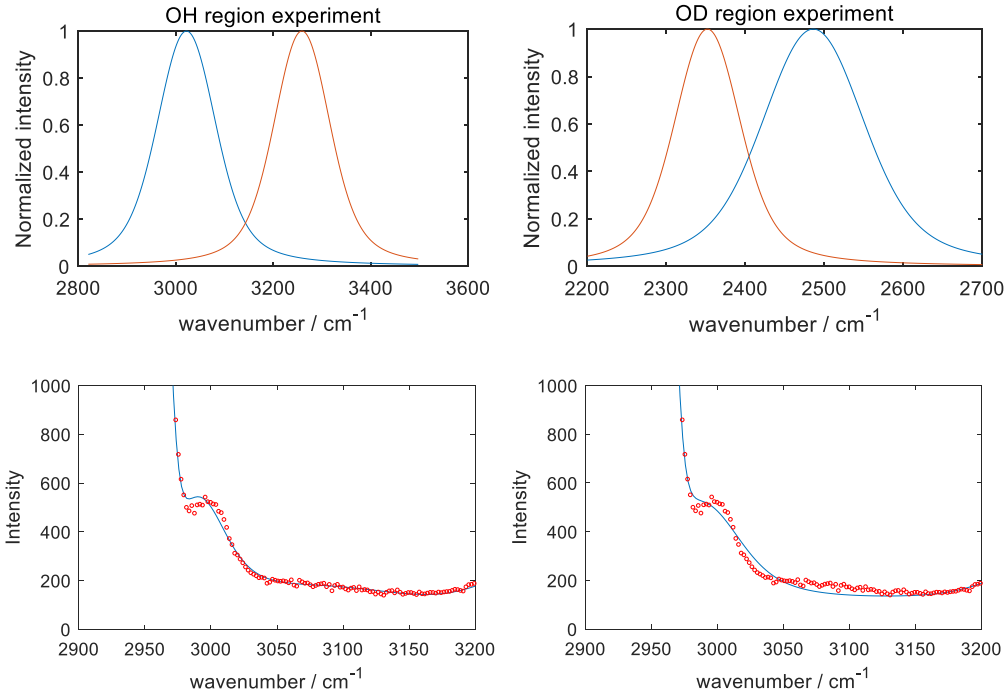

Figure 5.11. Top left: the overlap between strongly bound water and secondary OH is not large enough to be capable of generating significant interference. Top right: the overlap between strongly bound D_2O and secondary OD is also small in the deuterated experiment. Bottom left: spectral fitting presented in the main article; Bottom right: spectral fitting by forcing peaks to be broad to overlap and interfere with each other.

5.9.2 Wobbling-in-a-cone model

We conclude that "wobbling-in-a-cone" is negligible in the bi-exponential dynamics in our experiment for two reasons. First, all reported "wobbling-in-a-cone" lifetimes for water in hydrophilic environments are longer than 1 ps, which is much longer than most of the lifetimes in our case. (178–182) Second, the "wobbling-in-a-cone" shows a different isotope effect from the experimentally measured trend. "Wobbling-in-a-cone" lifetime depends on (183)

$$t \propto t_{rot} = C\eta + \frac{2\pi}{9}\sqrt{\frac{I}{k_B T}},$$

where η is the viscosity of the material, I is the moment of inertia and $I(\mathrm{D_2O}) \approx 1.8\, I(\mathrm{H_2O})$. Therefore, the "wobbling-in-a-cone" lifetime ratio between D_2O/H_2O should be between 1 (if the first term dominates) to 1.3 (if the second term dominates). In our experiment, the ratio is about 2, which agrees with Foster energy transfer, not "wobbling-in-a-cone."

5.9.3 CH dynamics

No dynamics of CH_3 or CH_2 modes were observed in our experiment. The transition dipole moments of CH modes, which are 5-10 times weaker than OH modes(184–186), make them 125-1000 times weaker than OH signals in the transient VSFG. This assessment is further supported by that the pump pulse energy used in this study is only 3 μJ, which is 10 to 26 times smaller than the pump pulse energy (30-80 μJ) used in the reports that studied CH dynamics using pump-probe VSFG spectroscopy. (164, 187, 188)

5.10 TGA-DSC Measurements

To estimate how many water molecules formed strong H-bond with the vacancy sites, we conducted TGA-DSC measurements of the lyophilized sheets sample and found the sample lost 9.6% weight at 146 °C (Figure. 5.12), above which the sample starts to decompose). This weight loss corresponds to a total of 15 water molecules for each SDS@2β-CD unit. From the first derivative of heat flow in DSC, which helps to find the hidden peaks in heat flow, we can identify two derivative shapes and therefore divide water thermal desorption process into four regions: below 47 °C (before the first derivative shape in 1st derivative, blue region), each SDS@2β-CD unit loses 0.9 water molecule; between 47-73 °C (first derivative shape, green region), each unit loses 4.9 water molecules; between 73-100 °C (second derivative, magenta region), each unit loses 6.0 water molecules; and above 100 °C (after the second derivative, cyan region), each unit loses 3.2 water molecules for each SDS@2β-CD unit.

Although it is difficult to assign these different regions into various water directly (e.g., cavity, loosely bound, and strongly bound water molecules (146)) in this self-assembly, it is safe to conclude the water in the first region is not strongly bounded to the materials. We can then estimate that roughly 9 to 14 water molecules are forming strongly-bound waters per SDS@2β-CD unit, corresponding to 4.5 to 7 water molecules per β-CD, distributed among the six vacancies. This assignment agrees with previous studies of other β-CD self-assemblies, which reported that there are usually 4-7 water molecules interacting with secondary OH of each β-CD.(151–155)

As discussed above, the self-assembly contains not only the strongly bound water at the interfacial vacancy sites but also other water molecules. Because the interfacial vacancies are hidden, it is difficult to

probe water at the interface of the self-assembly and liquid phase, as bulk-like water signals can overwhelm it. For example, in FTIR the OH peak is broad, composed of several peaks, whereas in VSFG, the OH features are much smaller and better resolved. This difference suggests that bulk-like water is the majority in the systems, which overwhelms the interfacial water, and VSFG is necessary to probe water at interfaces.

Chapter 5, in full, is a reprint of the material as it appears in Proceedings of the National Academy of Sciences of the United States of America, 2020. Haoyuan Wang; Jackson Wagner; Wenfan Chen; Chenglai Wang; Wei Xiong. United States National Academy of Sciences, 2020. The dissertation author was the primary investigator and author of this paper.

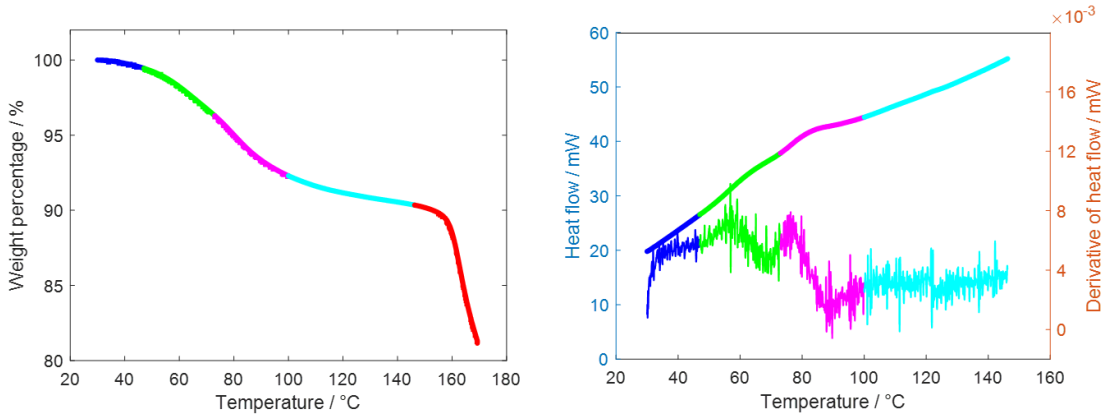

Figure 5.12. TGA (left) and DSC (right) measurements of the lyophilized sheets sample. In the DSC, the upper one is the heat flow while the bottom one is the first derivative of heat flow

Chapter 6

2D VSFG Microscopy Development

6.1 2D VSFG technique

In previous sections, one-dimensional VSFG has shown great capability of studying self-assemblies, and transient VSFG has demonstrated its application in studying dynamics in self-assemblies. However, there is still some information missing. By applying the multi-dimensional spectroscopy techniques into VSFG, it enables the ability to investigate the relationships between different modes. For example, in two-dimensional VSFG, the frequency correlation spectrum can offer structural information such as coupling between modes, anharmonicities and energy transfer rates, as well as molecular dynamics.

In a 2D VSFG experiment, two IR pump pulses first interact with the sample to create a coherence between ground state and first excited state. After a certain time delay t_2, which is called waiting time, the IR probe and upconversion pulse interact with the sample to detect the VSFG signal. The time delay between the two IR pulses t_1 can be tuned by the pulse shaper, which reflects the pump frequency through Fourier transform. The t_3 reflects the probe frequency through Fourier transform, which is done by the spectrograph since the spectra are collected in frequency domain.

6.2 Pulse shaper setup

To generate the two pulses for IR pump, we built the pulse shaper by our own from a germanium acousto-optic modulator (Ge AOM) based on literature. The detailed procedures of how to build the pulse shaper are listed below:

Abbreviations:

P: Parabolic; G: Blazed Grating; M: Mirror; f: focusing distance of parabolic

1. Mount G1/P1/P2 onto translational stage and put them on the laser table. Make sure the distance between G1/P1 is about f, and the distance between P1/P2 is about 2f.
2. Use the He-Ne laser to do the alignment. Put G1 to 0^{th} order, and rotate P1 to make sure all the beam diffracted by G1 are parallel after P1. If they are not parallel, adjust the distance between G1/P1.
3. Use a mirror to replace G2 for now. The diffracted He-Ne beams should all go onto the mirror at the same position. Make sure the beam after the mirror is collimated. If it is not collimated, the distance between P1/P2 should be adjusted.
4. Rotate G1 to 1^{st} order angle of the mid-IR beam. Replace the mirror with a detector and make sure the power is maximized.
5. Replace the detector with G2. Now G2/P2 should be fully symmetric with G1/P1.
6. Put the Ge AOM at the Fourier plane.
7. Plug in the power of Ge AOM and send the waveform in. For now, a relatively large waveform can be chosen, usually 0.8 V voltage range with 100% waveform intensity. The IR power after G2 should drop by about 50% since the Ge AOM would diffract the IR beam.

8. Rotate P1 counterclockwise by ~0.7°. The rotated angle is half of the Bragg angle for that center wavelength. For 4 μm, the angle is ~0.7°; for 5 μm, the angle is ~2°.

9. Rotate P2 clockwise accordingly to maximize the output power. Now the output changes from 0^{th} order to 1^{st} order of Ge AOM.

10. Optimize the waveform to maximize the output power. Usually, it is 0.68 V voltage range with 20% waveform.

11. Now the output beam after G2 will not be collimate anymore due to spatial chirp. It is because the Ge AOM diffracts different wavelengths of light differently. Therefore, the G2 needs to be rotated by ~2° to compensate for it. The beam size after G2 needs to be measured at several distances to make sure it is collimated.

6.3 Output Details

The efficiency of the pulse shaper at 4 μm we built is ~30% (3 μJ out of 9 μJ), which is comparable to what literature reported (30%).(189) If step 11 is not conducted, the pump pulse duration is about 600 fs (assuming probe pulse duration is 140 fs); after step 11, the pulse duration becomes ~140 fs.

Chapter 6, in full, is still under development. The dissertation author was one of the primary investigators.

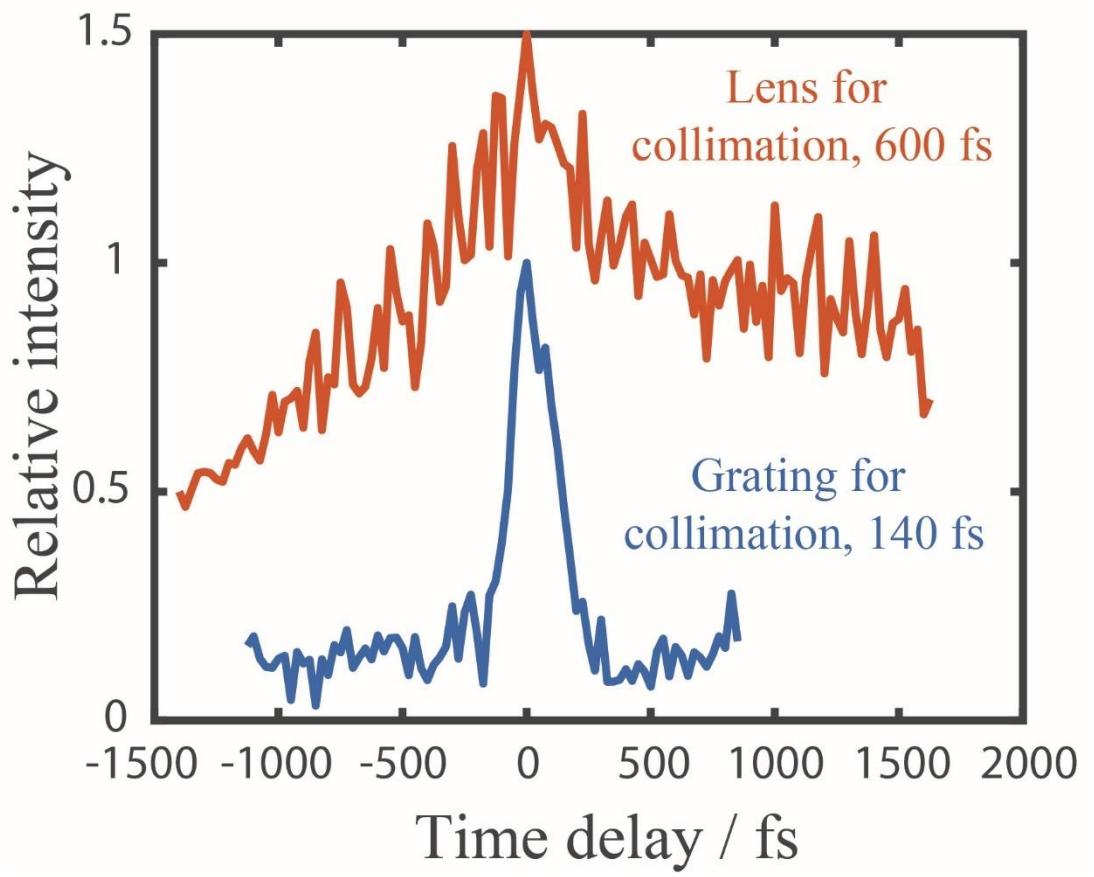

Figure 6.1. If we do not rotate G2 to compensate from spatial chirp generated by the Ge AOM and use a lens to collimate the beam, the pulse duration is about 600 fs. After finishing step 11, the pulse duration is reduced to 140 fs.

Chapter 7

Conclusion and Outlook

Sum frequency generation microscopy is a powerful technique to study self-assembly, from both static and dynamic perspective, in a spatially resolved manner. In this dissertation, two new SFG microscopies developed by us are introduced. With these of newly developed techniques, we obtained more information for self-assembly, which cannot be achieved by any other existing techniques. The main findings are summarized as below:

1. We built the first self-phase-stabilized heterodyne-detected VSFG microscopy. In our geometry, the VSFG signal and local oscillator are generated from the same beam path, which showed a 9-fold improvement in phase stability. Furthermore, our geometry also made spectrometer alignment and maintenance easy.

2. We studied SDS@2β-CD self-assembly using the heterodyne VSFG microscopy, and successfully identified domains with opposite molecular orientations.

3. We further studied the self-assembly with extended spectral coverage and demonstrated that self-assembled materials which lack inversion symmetry can be VSFG active. In particular, we showed anisotropy of SDS@2β-CD self-assembly, which was because the self-assembly is highly coordinated. Besides, the interaction between water and host molecules are so strong that can template water to adopt local mesoscopic ordering of the self-assembly.

4. The self-assembly is homogeneous within domain while heterogeneous among different domains. The heterogeneity comes from different local hydration level.

5. We built the first time-resolved VSFG microscopy with ~70 fs temporal resolution, and studied spatially resolved ultrafast dynamics in the self-assembly. We observed domain dependent ultrafast hydrogen bond network restoration, which was the product of Forster energy transfer process. The heterogeneity of the lifetime comes from the local hydration level, i.e., more hydrated domains have faster dynamics.

With the development of new technology, we can gain more information from the molecular systems. For example, if we finished building the 2D VSFG microscopy, we could potentially study the vibrational modes couplings and anharmonicities. This part of work will be finished by future students in Dr. Wei Xiong's group.

Furthermore, there are still some potential improvements for the heterodyne geometry. As I discussed in Chapter 3, even if the GVD is small in our experiment, it could become enormous if the spectral coverage becomes wide. This would limit the application of the collinear heterodyne technique. Therefore, it is important to develop a heterodyne geometry for wide spectral coverage with both stable phase and limited GVD.

Appendices

Appendix A. Voigt profile fitting code

A1. How the spectral fitting works

Voigt profile is the convolution between Lorentzian and Gaussian. The matlab code to fit the spectrum using Voigt profile follows the procedure:

1. A subfunction named 'SFG_Lorentzian' generates Lorentzian profile of a single peak.
2. A subfunction named 'SFG_Lorentzian_Gaussian' generates Voigt profile of a single peak by convolution.
3. A subfunction named 'SFG_signal_sum' generates SFG signal with Voigt profile by calculating absolute square of all the peaks.
4. The function named 'SpectralFitting' fits the spectrum.

Therefore, 'SpectralFitting' calls 'SFG_signal_sum'; then 'SFG_signal_sum' calls 'SFG_Lorentzian_Gaussian'; and 'SFG_Lorentzian_Gaussian' calls 'SFG_Lorentzian' in the end. All the input parameters are in 'SpectralFitting'.

A2. SFG_Lorentzian code

```
% A Lorentzian type function for susceptibility in SFG, no phase angle %
% OUTPUT:
% return the susceptibility array (complex numbers) as function of frequencies for a resonant peak

% INPUT:
% w frequencies, can be array
% wr resonant frequency, Tau, width, A, oscillation strength. All scaler
function ki = SFG_Lorentzian (A,wr,w,Tau)

ki=A*ones(size(w))./(w-wr+i*Tau);
```

A3. SFG_Lorentzian_Gaussian code

```
% Susceptibility with a gaussion distributed phase angle centered at zero degree%
% OUTPUT:
% return the susceptibility array (complex numbers) as function of frequencies for a resonant peak
```

```
% INPUT:
% w frequencies, can be array
% wr resonant frequency, Tau, width, A, oscillation strength. All scaler
% sigma, distribution of phase angle, in arc unit;
function ki = SFG_Lorentzian_Gaussian (A,wr,w,Tau,sigma)
%if (sigma<=3) % wavenumbers
  %    ki=SFG_Lorentzian(A,wr,w,Tau);
    % return;
%end

ki=zeros(size(w));

num_per_sigma=30;    %number of point evaluated for each sigma
max_sigma=3;              %max sigma evaluated
step=1;

if Tau<5
       step=0.1;
end

norm=0;
for n= -num_per_sigma*max_sigma:step:num_per_sigma*max_sigma
     weight= exp(-1*n*n/(num_per_sigma*num_per_sigma)); % weight according to gaussion distribution.
     ki=ki+SFG_Lorentzian(A,wr-n/num_per_sigma*sigma,w,Tau)*weight;
     norm=norm + weight;
end

ki=ki/norm;
```

A4. SFG_signal_sum code

```
% Sum of SFG signal %
% OUTPUT:
% return the signal array (real numbers) as function of frequencies

% INPUT:
% w frequencies, can be array
% n number of peaks
function y = SFG_signal_sum (parameters, frequency)
```

```
ki=zeros(size(frequency));
y=zeros(size(frequency));

num_peaks = (length(parameters)-2)/4;
for i = 1:num_peaks
    index = (i-1)*4 + 2 ;

ki=ki+SFG_Lorentzian_Gaussian(parameters(index+1),parameters(index+2),frequency,parameters(index
+3),parameters(index+4));
end


ki= ki+ parameters(2);    % non-resonant SFG signal

y = abs(ki).^2;

y= y+ parameters(1);    % Background noise from green light scattering
```

A5. SpectralFitting code

```
x=wavenumber;
y=intensity;

%If more peaks are needed, please follow the rule below
p=[0 %background scattering
0.0001 %non-resonant signal
220 %A1
2483    %wr1
5 %Tau1
45 %sigma1
240 %A2
2524 %wr2
5 %tau2
23 %sigma2
90 %A3
2349 %wr3
5 %tau3
49 %sigma3
];
```

```
num_peaks = (length(p)-2)/4; % num of peaks
n=5; %set optimization cycles

Boundary=[
0      8
-2    2
10      280 %A1
2380    2510 %wr1
5 5%Tau1
20      90 %sigma1
120      300 %A2
2510 2535%wr2
5 5%tau2
0      50 %sigma2
0      150
2310        2390
5      5
0      150
% 0 480
% 2380 2480
% 5 5
% 0 90
];

p_LB= Boundary(:,1);
p_UB= Boundary(:,2);

%[p_LB,p_UB]=Xin_Set_Parameter_Boundary(p);

pall=zeros(length(p),3);
pall(:,1)=p_LB;
pall(:,2)=p;
pall(:,3)=p_UB;

%Display the initial error
%y_predicted = SFG_signal_sum(p, x);
%[relative_residual,residual]=relative_residual(y_predicted,y);
%disp(strcat('Initial error = ',num2str(relative_residual)));
% optimization
options=optimset('Maxiter',500000,'TolFun',1.0*10^-8); %set iterative cycles
for index=1:n
```

```
    disp(strcat('*********Starting optimization cycle # ',num2str(index),'*********'));
    [p,residual_norm,residual]=lsqcurvefit('SFG_signal_sum',p,x,y,p_LB,p_UB,options);
    relative_residual = sqrt(residual_norm / sum (y.^2));
     disp(strcat('relative error = ',num2str(relative_residual)));

end


% print final error for individual points and sum error
if n>=0
      peaks=zeros(length(y),10);
    for index =1:num_peaks
        temp=SFG_Lorentzian_Gaussian(p(index*4-1),p(index*4),x,p(index*4+1),p(index*4+2));
        peaks(:,index)=abs(temp).^2;
    end

    y_predicted = SFG_signal_sum(p, x);

    %plot(x,y_predicted,'b-',x,peaks(:,1),'r--',x,peaks(:,2),'g--',x,peaks(:,3),'c--',x,peaks(:,4),'r--
',x,peaks(:,5),'g--',x,peaks(:,6));    % plot y against x

      % Print final variables
      disp(p);
end

% Print results

ys=zeros(10,length(y));
ys(1,:)=rot90(x);
ys(2,:)=rot90(y);
ys(3,:)=rot90(y_predicted);

for index =1:num_peaks
        temp=SFG_Lorentzian_Gaussian(p(index*4-1),p(index*4),x,p(index*4+1),p(index*4+2));
        ys(index+3,:)=rot90(abs(temp).^2);
end

fid=fopen('data.txt','w');
fprintf(fid,'%6.6f    %6.6f      %6.6f      %6.6f      %6.6f      %6.6f      %6.6f      %6.6f      %6.6f      %6.6f\n
',ys);
fclose(fid);
```

```
figure;plot(x,y);hold on;plot(x,y_predicted)
```

Appendix B. Matlab code for simulation of geometric arrangement in Figure 5.8

B1. 2-water situation

```
close all;
clear all
%Coordinates of all the O atoms
OH1=-5.35;;
OH2=-4.1+4.2*i;
OH3=-4.1-4.2*i;
OH4=-1.5+2.9*i;
OH5=-1.5-2.9*i;
OH6=1.5+2.9*i;
OH7=1.5-2.9*i;
OH8=4.1+4.2*i;
OH9=4.1-4.2*i;
OH10=5.35;

x1=real(OH1);x2=0;x3=0;x4=0;

m=1;
step=0.05;
step2=0.05;
a=1
water=0;
re=2.7; %parameter in the Morse potential

while x1<real(OH10)
    if x1<real(OH4) | x1>real(OH6)
    x1=x1+step
    else
        x1=x1+step2
    end
    if x1<=real(OH4) | x1>=real(OH6)
    lim= imag(OH2);
    else
        lim=imag(OH4);
    end
    n=floor(2*lim/step);
    y1= linspace(-lim, lim, n);
    x1_array=ones(1,length(y1))*x1;
```

```
    water=[water x1_array+i*y1];
    a=a+1;
end

bound=2.2; %assuming the distance between two OH should not be smaller than this value
for j=length(water):(-1):1
    temp=water(j);
    if min(abs([temp-OH1 temp-OH2 temp-OH3 temp-OH4 temp-OH5 temp-OH6 temp-OH7 temp-OH8 temp-OH9
temp-OH10]))<bound
    water(j)=[];
    end
end
water(1)=[];
%%
water_min=zeros(1,4);
std_min=100000;
E_min=100000;
ET_min=100000;
for A=1:length(water)
    A
    length(water)
    w1=water(A);
    for B=A+1:length(water)
        w2=water(B);
        if abs(w2-w1)>bound
                    if min(abs([OH1-w1 OH1-w2]))<3.2 & min(abs([OH4-w1 OH4-w2]))<3.2 &
min(abs([OH5-w1 OH5-w2]))<3.2 & min(abs([OH6-w1 OH6-w2]))<3.2 & min(abs([OH7-w1 OH7-w2]))<3.2 &
min(abs([OH10-w1 OH10-w2]))<3.2
                        w1d=(abs([w1-w2 w1-OH1 w1-OH2 w1-OH3 w1-OH4 w1-OH5 w1-OH6 w1-
OH7 w1-OH8 w1-OH9 w1-OH10]));
                        HB1=(abs([w1-w2,12; w1-OH1,1.1; w1-OH2,1.2; w1-OH3,1.3; w1-OH4,1.4; w1-
OH5,1.5; w1-OH6,1.6; w1-OH7,1.7; w1-OH8,1.8; w1-OH9,1.9; w1-OH10,1.11]));%
                        HB1a=sortrows(HB1);
                        HB1real=HB1a(1:4,:);

                        w2d=(abs([w2-w1 w2-OH1 w2-OH2 w2-OH3 w2-OH4 w2-OH5 w2-OH6 w2-
OH7 w2-OH8 w2-OH9 w2-OH10]));
                        HB2=(abs([w2-OH1,2.1; w2-OH2,2.2; w2-OH3,2.3; w2-OH4,2.4; w2-OH5,2.5;
w2-OH6,2.6; w2-OH7,2.7; w2-OH8,2.8; w2-OH9,2.9; w2-OH10,2.11]));%
                        HB2a=sortrows(HB2);
                        HB2real=HB2a(1:(4-double(ismember(12,HB1real(:,2)))),:);
```

```
                                HBr=([w1d w2d(2:end)]);
                                Ew_i=(1-exp(re-HBr)).^2-1;

                                HBreal=[HB1real; HB2real];
                                HBsave=HBreal;

                                Ew_j=(1-exp(re-HBreal(:,1))).^2-1;


                                Ew=sum(Ew_j);
                                EwT=sum(Ew_i);

                                if Ew<=E_min %&EwT<=ET_min
                                    E_min=Ew;
                                    ET_min=EwT;
                                    wd1=[w1d; w2d];
                                    water_min1=[w1 w2];
                                    clear HBsave;
                                    HBsave=HBreal;
                                end
                            end
                        end
                    end
                end

                E_min
                ET_min
                %%
                figure;plot(real(OH1),imag(OH1),'ro')
                hold on
                plot(real(OH2),imag(OH2),'ro')
                plot(OH3,'ro')
                plot(OH4,'ro')
                plot(OH5,'ro')
                plot(real(OH6),imag(OH6),'ro')
                plot(OH7,'ro')
                plot(OH8,'ro')
                plot(OH9,'ro')
                plot(real(OH10),imag(OH10),'ro')
                plot(real(water),imag(water),'bo')
```

```
plot(real(water_min1),imag(water_min1),'m*')
daspect([1 1 1])
```

B2. 3-water simulation

```
close all; clear all

OH1=-5.35;;
OH2=-4.1+4.2*i;
OH3=-4.1-4.2*i;
OH4=-1.5+2.9*i;
OH5=-1.5-2.9*i;
OH6=1.5+2.9*i;
OH7=1.5-2.9*i;
OH8=4.1+4.2*i;
OH9=4.1-4.2*i;
OH10=5.35;

x1=real(OH1);x2=0;x3=0;x4=0;
%y1=0;y2=0;y3=0;y4=0;

m=1;
step=0.2;
step2=0.2;
a=1
water=0;
re=2.7;
while x1<real(OH10)
    if x1<real(OH4) | x1>real(OH6)
    x1=x1+step
    else
        x1=x1+step2
    end
    if x1<=real(OH4) | x1>=real(OH6)
    lim= imag(OH2);
    else
        lim=imag(OH4);
    end
    n=floor(2*lim/step);
    y1= linspace(-lim, lim, n);
    x1_array=ones(1,length(y1))*x1;
    water=[water x1_array+i*y1];
    a=a+1;
end
```

```
bound=2.1;
for j=length(water):(-1):1
    temp=water(j);
    if min(abs([temp-OH1 temp-OH2 temp-OH3 temp-OH4 temp-OH5 temp-OH6 temp-OH7 temp-OH8
temp-OH9 temp-OH10]))<bound
    water(j)=[];
    end
end
water(1)=[];
%%
water_min=zeros(1,4);
std_min=100000;
E_min=100000;
ET_min=100000;
for A=1:length(water)
    A
    length(water)
    w1=water(A);
    for B=A+1:length(water)
        w2=water(B);
        if abs(w2-w1)>bound
            for C=B+1:length(water)
                w3=water(C);
                if min(abs([w3-w1 w3-w2]))>bound
                    %for D=C+1:length(water)
                     %     w4=water(D);
                      %    if min(abs([w4-w1 w4-w2 w4-w3]))>bound
                        if min(abs([OH1-w1 OH1-w2 OH1-w3]))<3.0 & min(abs([OH4-w1 OH4-w2
OH4-w3]))<3.0 & min(abs([OH5-w1 OH5-w2 OH5-w3]))<3.0 & min(abs([OH6-w1 OH6-w2 OH6-
w3]))<3.0 & min(abs([OH7-w1 OH7-w2 OH7-w3]))<3.0 & min(abs([OH10-w1 OH10-w2 OH10-
w3]))<3.0
                            w1d=(abs([w1-w2 w1-w3 w1-OH1 w1-OH2 w1-OH3 w1-OH4 w1-
OH5 w1-OH6 w1-OH7 w1-OH8 w1-OH9 w1-OH10]));
                            HB1=(abs([w1-w2,12; w1-w3,13; w1-OH1,1.1; w1-OH2,1.2; w1-
OH3,1.3; w1-OH4,1.4; w1-OH5,1.5; w1-OH6,1.6; w1-OH7,1.7; w1-OH8,1.8; w1-OH9,1.9; w1-
OH10,1.11]));%
                            HB1a=sortrows(HB1);
                            HB1real=HB1a(1:4,:);

                            w2d=(abs([w2-w1 w2-w3 w2-OH1 w2-OH2 w2-OH3 w2-OH4 w2-
```

```
OH5 w2-OH6 w2-OH7 w2-OH8 w2-OH9 w2-OH10]));
                                HB2=(abs([w2-w3,23; w2-OH1,2.1; w2-OH2,2.2; w2-OH3,2.3; w2-
OH4,2.4; w2-OH5,2.5; w2-OH6,2.6; w2-OH7,2.7; w2-OH8,2.8; w2-OH9,2.9; w2-OH10,2.11]));%
                                HB2a=sortrows(HB2);
                                HB2real=HB2a(1:(4-double(ismember(12,HB1real(:,2)))),:);

                                w3d=(abs([w3-w1 w3-w2 w3-OH1 w3-OH2 w3-OH3 w3-OH4 w3-
OH5 w3-OH6 w3-OH7 w3-OH8 w3-OH9 w3-OH10]));
                                HB3=(abs([w3-OH1,3.1; w3-OH2,3.2; w3-OH3,3.3; w3-OH4,3.4; w3-
OH5,3.5; w3-OH6,3.6; w3-OH7,3.7; w3-OH8,3.8; w3-OH9,3.9; w3-OH10,3.11]));%
                                HB3a=sortrows(HB3);
                                HB3real=HB3a(1:(4-double(ismember(23,HB2real(:,2)))-
double(ismember(13,HB1real(:,2)))),:);

                                %w4d=(abs([w4-w1 w4-w2 w4-w3 w4-OH1 w4-OH2 w4-OH3 w4-
OH4 w4-OH5 w4-OH6 w4-OH7 w4-OH8 w4-OH9 w4-OH10]));
                                %HB4=(abs([w4-OH1,4.1; w4-OH2,4.2; w4-OH3,4.3; w4-OH4,4.4;
w4-OH5,4.5; w4-OH6,4.6; w4-OH7,4.7; w4-OH8,4.8; w4-OH9,4.9; w4-OH10,4.11]));%
                                %HB4a=sortrows(HB4);
                                %HB4real=HB4a(1:(4-double(ismember(34,HB3real(:,2)))-
double(ismember(24,HB2real(:,2)))-double(ismember(14,HB1real(:,2)))),:);



                                %%%%%%%%%%%%this lines of code solve the new issue
                                HBr=([w1d w2d(2:end) w3d(3:end)]);
                                Ew_i=(1-exp(re-HBr)).^2-1;
                                %[Ew1    IN1]=sort(Ew_i(1:9));[Ew2    IN2]=sort(Ew_i(10:17));[Ew3
IN3]=sort(Ew_i(18:24));[Ew4 IN4]=sort(Ew_i(25:30));%
                                %wOH1=[w1-w2 w1-w3 w1-w4 w1-OH1 w1-OH2 w1-OH3 w1-OH4
w1-OH5 w1-OH6];
                                %wOH2=[w2-w1 w2-w3 w2-w4 w2-OH1 w2-OH2 w2-OH3 w2-OH4
w2-OH5 w2-OH6];
                                %wOH3=[w3-w1 w3-w2 w3-w4 w3-OH1 w3-OH2 w3-OH3 w3-OH4
w3-OH5 w3-OH6];
                                %wOH4=[w4-w1 w4-w2 w4-w3 w4-OH1 w4-OH2 w4-OH3 w4-OH4
w4-OH5 w4-OH6];



                                HBreal=[HB1real; HB2real; HB3real];
                                HBsave=HBreal;
                                %Ew1=sort(Ew_i(1:9));Ew2=sort(Ew_i(10:17));Ew3=sort(Ew_i(18:2
```

```
4));Ew4=sort(Ew_i(25:30));
                                    %Ew=sum(Ew1(1:4)+Ew2(1:4)+Ew3(1:4)+Ew4(1:4));

                                    Ew_j=(1-exp(re-HBreal(:,1))).^2-1;


                                    Ew=sum(Ew_j);
                                    EwT=sum(Ew_i);
                                    %%%%%%%%%%%%%%%%%%%%%%%%%%%%%%%%%%%%
                                    %Ew=sum((1-exp(re-w1d)).^2)+sum((1-exp(re-
w2d(2:end))).^2)+sum((1-exp(re-w3d(3:end))).^2)+sum((1-exp(re-w4d(4:end))).^2);

                                    if Ew<=E_min %&EwT<=ET_min
                                        E_min=Ew;
                                        ET_min=EwT;
                                        wd1=[w1d; w2d; w3d];
                                        water_min1=[w1 w2 w3];
                                        %IN=[IN1(1:4); IN2(1:4); IN3(1:4); IN4(1:4)];%
                                        %wOH=[wOH1; wOH2; wOH3; wOH4];
                                        clear HBsave;
                                        HBsave=HBreal;
                                    end
                                end
                                 % end
                            %end
                        end
                    end
                end
            end
        end
end

E_min
ET_min
%%
figure;plot(real(OH1),imag(OH1),'ro')
hold on
plot(real(OH2),imag(OH2),'ro')
plot(OH3,'ro')
plot(OH4,'ro')
plot(OH5,'ro')
plot(real(OH6),imag(OH6),'ro')
```

```
plot(OH7,'ro')
plot(OH8,'ro')
plot(OH9,'ro')
plot(real(OH10),imag(OH10),'ro')
plot(real(water),imag(water),'bo')
%plot(real(water_min),imag(water_min),'g*')
plot(real(water_min1),imag(water_min1),'m*')
daspect([1 1 1])
```

B3. 4-water simulation

```
close all; clear all

OH1=-5.35;;
OH2=-4.1+4.2*i;
OH3=-4.1-4.2*i;
OH4=-1.5+2.9*i;
OH5=-1.5-2.9*i;
OH6=1.5+2.9*i;
OH7=1.5-2.9*i;
OH8=4.1+4.2*i;
OH9=4.1-4.2*i;
OH10=5.35;

x1=real(OH1);

m=1;
step=0.3;
step2=0.3;
a=1
water=0;
re=2.7;
while x1<real(OH10)
    if x1<real(OH4) | x1>real(OH6)
    x1=x1+step
    else
        x1=x1+step2
    end
    if x1<=real(OH4) | x1>=real(OH6)
    lim= imag(OH2);
    else
        lim=imag(OH4);
    end
    n=floor(2*lim/step);
    y1= linspace(-lim, lim, n);
    x1_array=ones(1,length(y1))*x1;
    water=[water x1_array+i*y1];
    a=a+1;
end
```

```
bound=2.2;
for j=length(water):(-1):1
    temp=water(j);
    if min(abs([temp-OH1 temp-OH2 temp-OH3 temp-OH4 temp-OH5 temp-OH6 temp-OH7 temp-OH8
temp-OH9 temp-OH10]))<bound
    water(j)=[];
    end
end
water(1)=[];
%%
water_min=zeros(1,4);
std_min=100000;
E_min=100000;
ET_min=100000;
for A=1:length(water)
    A
    length(water)
    w1=water(A);
    for B=A+1:length(water)
        w2=water(B);
        if abs(w2-w1)>bound & real(w2)<real(OH4)
            for C=B+1:length(water)
                w3=water(C);
                if min(abs([w3-w1 w3-w2]))>bound & real(w3)>real(OH4) & real(w3)<real(OH6)%
                    for D=C+1:length(water)
                        w4=water(D);
                        if min(abs([w4-w1 w4-w2 w4-w3]))>bound & real(w4)>real(OH6)%

                            w1d=(abs([w1-w2 w1-w3 w1-w4 w1-OH1 w1-OH2 w1-OH3 w1-OH4
w1-OH5 w1-OH6 w1-OH7 w1-OH8 w1-OH9 w1-OH10]));
                            HB1=(abs([w1-w2,12; w1-w3,13; w1-w4,14; w1-OH1,1.1; w1-
OH2,1.2; w1-OH3,1.3; w1-OH4,1.4; w1-OH5,1.5; w1-OH6,1.6; w1-OH7,1.7; w1-OH8,1.8; w1-OH9,1.9;
w1-OH10,1.11]));%
                            HB1a=sortrows(HB1);
                            HB1real=HB1a(1:4,:);

                            w2d=(abs([w2-w1 w2-w3 w2-w4 w2-OH1 w2-OH2 w2-OH3 w2-OH4
w2-OH5 w2-OH6 w2-OH7 w2-OH8 w2-OH9 w2-OH10]));
                            HB2=(abs([w2-w3,23; w2-w4,24; w2-OH1,2.1; w2-OH2,2.2; w2-
OH3,2.3; w2-OH4,2.4; w2-OH5,2.5; w2-OH6,2.6; w2-OH7,2.7; w2-OH8,2.8; w2-OH9,2.9; w2-
OH10,2.11]));%
```

```
HB2a=sortrows(HB2);
HB2real=HB2a(1:(4-double(ismember(12,HB1real(:,2)))),:);

w3d=(abs([w3-w1 w3-w2 w3-w4 w3-OH1 w3-OH2 w3-OH3 w3-OH4
w3-OH5 w3-OH6 w3-OH7 w3-OH8 w3-OH9 w3-OH10]));
HB3=(abs([w3-w4,34; w3-OH1,3.1; w3-OH2,3.2; w3-OH3,3.3; w3-
OH4,3.4; w3-OH5,3.5; w3-OH6,3.6; w3-OH7,3.7; w3-OH8,3.8; w3-OH9,3.9; w3-OH10,3.11]));%
HB3a=sortrows(HB3);
HB3real=HB3a(1:(4-double(ismember(23,HB2real(:,2)))-
double(ismember(13,HB1real(:,2)))),:);

w4d=(abs([w4-w1 w4-w2 w4-w3 w4-OH1 w4-OH2 w4-OH3 w4-OH4
w4-OH5 w4-OH6 w4-OH7 w4-OH8 w4-OH9 w4-OH10]));
HB4=(abs([w4-OH1,4.1; w4-OH2,4.2; w4-OH3,4.3; w4-OH4,4.4; w4-
OH5,4.5; w4-OH6,4.6; w4-OH7,4.7; w4-OH8,4.8; w4-OH9,4.9; w4-OH10,4.11]));%
HB4a=sortrows(HB4);
HB4real=HB4a(1:(4-double(ismember(34,HB3real(:,2)))-
double(ismember(24,HB2real(:,2)))-double(ismember(14,HB1real(:,2)))),:);


%%%%%%%%%%%%this lines of code solve the new issue
HBr=([w1d w2d(2:end) w3d(3:end) w4d(4:end)]);
Ew_i=(1-exp(re-HBr)).^2-1;
%[Ew1    IN1]=sort(Ew_i(1:9));[Ew2    IN2]=sort(Ew_i(10:17));[Ew3
IN3]=sort(Ew_i(18:24));[Ew4 IN4]=sort(Ew_i(25:30));%
%wOH1=[w1-w2 w1-w3 w1-w4 w1-OH1 w1-OH2 w1-OH3 w1-OH4
w1-OH5 w1-OH6];
%wOH2=[w2-w1 w2-w3 w2-w4 w2-OH1 w2-OH2 w2-OH3 w2-OH4
w2-OH5 w2-OH6];
%wOH3=[w3-w1 w3-w2 w3-w4 w3-OH1 w3-OH2 w3-OH3 w3-OH4
w3-OH5 w3-OH6];
%wOH4=[w4-w1 w4-w2 w4-w3 w4-OH1 w4-OH2 w4-OH3 w4-OH4
w4-OH5 w4-OH6];


HBreal=[HB1real; HB2real; HB3real; HB4real];
HBsave=HBreal;
%Ew1=sort(Ew_i(1:9));Ew2=sort(Ew_i(10:17));Ew3=sort(Ew_i(18:2
4));Ew4=sort(Ew_i(25:30));
%Ew=sum(Ew1(1:4)+Ew2(1:4)+Ew3(1:4)+Ew4(1:4));
```

```
                                    Ew_j=(1-exp(re-HBreal(:,1))).^2-1;


                                    Ew=sum(Ew_j);
                                    EwT=sum(Ew_i);
                                    %%%%%%%%%%%%%%%%%%%%%%%%%%%%%%%%%%%%
                                    %Ew=sum((1-exp(re-w1d)).^2)+sum((1-exp(re-
w2d(2:end))).^2)+sum((1-exp(re-w3d(3:end))).^2)+sum((1-exp(re-w4d(4:end))).^2);

                                    if Ew<=E_min %&EwT<=ET_min
                                        E_min=Ew;
                                        ET_min=EwT;
                                        wd1=[w1d; w2d; w3d; w4d];
                                        water_min1=[w1 w2 w3 w4];
                                        %IN=[IN1(1:4); IN2(1:4); IN3(1:4); IN4(1:4)];%
                                        %wOH=[wOH1; wOH2; wOH3; wOH4];
                                        clear HBsave;
                                        HBsave=HBreal;
                                    end
                                end
                            end
                        end
                    end
                end
            end
        end
    end

E_min
ET_min
%%
figure;plot(real(OH1),imag(OH1),'ro')
hold on
plot(real(OH2),imag(OH2),'ro')
plot(OH3,'ro')
plot(OH4,'ro')
plot(OH5,'ro')
plot(real(OH6),imag(OH6),'ro')
plot(OH7,'ro')
plot(OH8,'ro')
plot(OH9,'ro')
plot(real(OH10),imag(OH10),'ro')
```

```
plot(real(water),imag(water),'bo')
plot(real(water_min),imag(water_min),'g*')
plot(real(water_min1),imag(water_min1),'m*')
daspect([1 1 1])
```

B4. 5-water simulation

```
close all; clear all
OH1=-5.35;
OH2=-4.1+4.2*i;
OH3=-4.1-4.2*i;
OH4=-1.5+2.9*i;
OH5=-1.5-2.9*i;
OH6=1.5+2.9*i;
OH7=1.5-2.9*i;
OH8=4.1+4.2*i;
OH9=4.1-4.2*i;
OH10=5.35;

x1=real(OH1);

m=1;
step=0.2;
step2=0.2;
a=1
water=0;
re=2.7;
while x1<real(OH10)
    if x1<real(OH4) | x1>real(OH6)
    x1=x1+step
    else
        x1=x1+step2
    end
    if x1<=real(OH4) | x1>=real(OH6)
    lim= imag(OH2);
    else
        lim=imag(OH4);
    end
    n=floor(2*lim/step);
    y1= linspace(-lim, lim, n);
    x1_array=ones(1,length(y1))*x1;
    water=[water x1_array+i*y1];
    a=a+1;
end

bound=2.2;
```

```
for j=length(water):-1:1
    temp=water(j);
    if min(abs([temp-OH1 temp-OH2 temp-OH3 temp-OH4 temp-OH5 temp-OH6]))<bound
    water(j)=[];
    end
end
water(1)=[];


%%
water_min=zeros(1,4);
std_min=100000;
E_min=100000;
ET_min=100000;
for A=1:length(water)
    A
    length(water)
    w1=water(A);
    for B=A+1:length(water)
        w2=water(B);
        if abs(w2-w1)>bound
            for C=B+1:length(water)
                w3=water(C);
                if min(abs([w3-w1 w3-w2]))>bound
                    for D=C+1:length(water)
                        w4=water(D);
                        if min(abs([w4-w1 w4-w2 w4-w3]))>bound
                            for E=D+1:1:length(water)
                                w5=water(E);
                                if min(abs([w5-w1 w5-w2 w5-w3 w5-w4]))>bound
                                    w1d=(abs([w1-w2 w1-w3 w1-w4 w1-w5 w1-OH1 w1-OH2
w1-OH3 w1-OH4 w1-OH5 w1-OH6 w1-OH7 w1-OH8 w1-OH9 w1-OH10]));
                                    HB1=(abs([w1-w2,12; w1-w3,13; w1-w4,14; w1-w5,15; w1-
OH1,1.1; w1-OH2,1.2; w1-OH3,1.3; w1-OH4,1.4; w1-OH5,1.5; w1-OH6,1.6; w1-OH7,1.7; w1-OH8,1.8;
w1-OH9,1.9; w1-OH10,1.11]));%
                                    HB1a=sortrows(HB1);
                                    HB1real=HB1a(1:4,:);

                                    w2d=(abs([w2-w1 w2-w3 w2-w4 w2-w5 w2-OH1 w2-OH2
w2-OH3 w2-OH4 w2-OH5 w2-OH6 w2-OH7 w2-OH8 w2-OH9 w2-OH10]));
                                    HB2=(abs([w2-w3,23;  w2-w4,24;  w2-w5,25;  w2-OH1,2.1;
```

```
w2-OH2,2.2; w2-OH3,2.3; w2-OH4,2.4; w2-OH5,2.5; w2-OH6,2.6; w2-OH7,2.7; w2-OH8,2.8; w2-OH9,2.9; w2-OH10,2.11]));%
                                        HB2a=sortrows(HB2);
                                        HB2real=HB2a(1:(4-double(ismember(12,HB1real(:,2)))),:);

                                        w3d=(abs([w3-w1 w3-w2 w3-w4 w3-w5 w3-OH1 w3-OH2 w3-OH3 w3-OH4 w3-OH5 w3-OH6 w3-OH7 w3-OH8 w3-OH9 w3-OH10]));
                                        HB3=(abs([w3-w4,34; w3-w5,35; w3-OH1,3.1; w3-OH2,3.2; w3-OH3,3.3; w3-OH4,3.4; w3-OH5,3.5; w3-OH6,3.6; w3-OH7,3.7; w3-OH8,3.8; w3-OH9,3.9; w3-OH10,3.11]));%
                                        HB3a=sortrows(HB3);
                                        HB3real=HB3a(1:(4-double(ismember(23,HB2real(:,2)))-double(ismember(13,HB1real(:,2)))),:);

                                        w4d=(abs([w4-w1 w4-w2 w4-w3 w4-w5 w4-OH1 w4-OH2 w4-OH3 w4-OH4 w4-OH5 w4-OH6 w4-OH7 w4-OH8 w4-OH9 w4-OH10]));
                                        HB4=(abs([w4-w5,45; w4-OH1,4.1; w4-OH2,4.2; w4-OH3,4.3; w4-OH4,4.4; w4-OH5,4.5; w4-OH6,4.6; w4-OH7,4.7; w4-OH8,4.8; w4-OH9,4.9; w4-OH10,4.11]));%
                                        HB4a=sortrows(HB4);
                                        HB4real=HB4a(1:(4-double(ismember(34,HB3real(:,2)))-double(ismember(24,HB2real(:,2)))-double(ismember(14,HB1real(:,2)))),:);

                                        w5d=(abs([w5-w1 w5-w2 w5-w3 w5-w4 w5-OH1 w5-OH2 w5-OH3 w5-OH4 w5-OH5 w5-OH6 w5-OH7 w5-OH8 w5-OH9 w5-OH10]));
                                        HB5=(abs([w5-OH1,5.1; w5-OH2,5.2; w5-OH3,5.3; w5-OH4,5.4; w5-OH5,5.5; w5-OH6,5.6; w5-OH7,5.7; w5-OH8,5.8; w5-OH9,5.9; w5-OH10,5.11]));%
                                        HB5a=sortrows(HB5);
                                        HB5real=HB5a(1:(4-double(ismember(45,HB4real(:,2)))-double(ismember(35,HB3real(:,2)))-double(ismember(25,HB2real(:,2)))-double(ismember(15,HB1real(:,2)))),:);


                                        %%%%%%%%%%%%this lines of code solve the new issue
                                        HBr=([w1d w2d(2:end) w3d(3:end) w4d(4:end) w5d(5:end)]);

                                        HBreal=[HB1real; HB2real; HB3real; HB4real; HB5real];
                                        HBsave=HBreal;
                                        %Ew1=sort(Ew_i(1:9));Ew2=sort(Ew_i(10:17));Ew3=sort(Ew_i(18:24));Ew4=sort(Ew_i(25:30));
```

```
                                    %Ew=sum(Ew1(1:4)+Ew2(1:4)+Ew3(1:4)+Ew4(1:4));

                                    Ew_j=(1-exp(re-HBreal(:,1))).^2-1;
                                    Ew_i=(1-exp(re-HBr)).^2-1;

                                    Ew=sum(Ew_j);
                                    EwT=sum(Ew_i);
                                    %%%%%%%%%%%%%%%%%%%%%%%%%%%%%%%%%%%

                                    %Ew=sum((1-exp(re-w1d)).^2)+sum((1-exp(re-w2d(2:end))).^2)+sum((1-exp(re-w3d(3:end))).^2)+sum((1-exp(re-w4d(4:end))).^2);

                                    if Ew<=E_min %&EwT<=ET_min
                                        E_min=Ew;
                                        ET_min=EwT;
                                        wd1=[w1d; w2d; w3d; w4d; w5d];
                                        water_min1=[w1 w2 w3 w4 w5];
                                        clear HBsave;
                                        HBsave=HBreal;
                                    end
                                end
                            end
                        end
                    end
                end
            end
        end
    end
end

%std_min
E_min
ET_min
%%
figure;plot(real(OH1),imag(OH1),'ro')
hold on
plot(real(OH2),imag(OH2),'ro')
plot(OH3,'ro')
plot(OH4,'ro')
plot(OH5,'ro')
plot(real(OH6),imag(OH6),'ro')
```

```
plot(OH7,'ro')
plot(OH8,'ro')
plot(OH9,'ro')
plot(real(OH10),imag(OH10),'ro')
plot(real(water),imag(water),'bo')
%plot(real(water_min),imag(water_min),'g*')
plot(real(water_min1),imag(water_min1),'m*')
daspect([1 1 1])
```

B5. 6-water simulation

```
close all; clear all
OH1=-5.35;
OH2=-4.1+4.2*i;
OH3=-4.1-4.2*i;
OH4=-1.5+2.9*i;
OH5=-1.5-2.9*i;
OH6=1.5+2.9*i;
OH7=1.5-2.9*i;
OH8=4.1+4.2*i;
OH9=4.1-4.2*i;
OH10=5.35;

x1=real(OH1)-0.4;

m=1;
step=0.3;
step2=0.3;
a=1
water=0;
re=2.7;
while x1<(real(OH10)+0.4)
    if x1<real(OH4) | x1>real(OH6)
    x1=x1+step
    else
        x1=x1+step2
    end
    if x1<=real(OH4) | x1>=real(OH6)
    lim= imag(OH2);
    else
        lim=imag(OH4);
    end
    n=floor(2*lim/step);
    y1= linspace(-lim, lim, n);
    x1_array=ones(1,length(y1))*x1;
    water=[water x1_array+i*y1];
    a=a+1;
end

bound=2.2;
```

```
for j=length(water):-1:1
    temp=water(j);
    if min(abs([temp-OH1 temp-OH2 temp-OH3 temp-OH4 temp-OH5 temp-OH6 temp-OH7 temp-OH8
temp-OH9 temp-OH10]))<bound
    water(j)=[];
    end
end
water(1)=[];

%%
water_min=zeros(1,4);
std_min=100000;
E_min=100000;
ET_min=100000;
for A=1:length(water)
    A
    w1=water(A);
    for B=A+1:length(water)
        w2=water(B);
        if abs(w2-w1)>bound
            for C=B+1:length(water)
                w3=water(C);
                if min(abs([w3-w1 w3-w2]))>bound
                    for D=C+1:length(water)
                        w4=water(D);
                        if min(abs([w4-w1 w4-w2 w4-w3]))>bound
                            for E=D+1:1:length(water)
                                w5=water(E);
                                if min(abs([w5-w1 w5-w2 w5-w3 w5-w4]))>bound
                                    for F=E+1:1:length(water)
                                        w6=water(F);
                                        if min(abs([w6-w1 w6-w2 w6-w3 w6-w4 w6-
w5]))>bound
                                            w1d=(abs([w1-w2 w1-w3 w1-w4 w1-w5 w1-
w6 w1-OH1 w1-OH2 w1-OH3 w1-OH4 w1-OH5 w1-OH6 w1-OH7 w1-OH8 w1-OH9 w1-OH10]));
                                            HB1=(abs([w1-w2,12; w1-w3,13; w1-w4,14;
w1-w5,15; w1-w6,16; w1-OH1,1.1; w1-OH2,1.2; w1-OH3,1.3; w1-OH4,1.4; w1-OH5,1.5; w1-OH6,1.6;
w1-OH7,1.7; w1-OH8,1.8; w1-OH9,1.9; w1-OH10,1.11]));%
                                            HB1a=sortrows(HB1);
                                            HB1real=HB1a(1:4,:);
```

w2d=(abs([w2-w1 w2-w3 w2-w4 w2-w5 w2-w6 w2-OH1 w2-OH2 w2-OH3 w2-OH4 w2-OH5 w2-OH6 w2-OH7 w2-OH8 w2-OH9 w2-OH10]));

HB2=(abs([w2-w3,23; w2-w4,24; w2-w5,25; w2-w6,26; w2-OH1,2.1; w2-OH2,2.2; w2-OH3,2.3; w2-OH4,2.4; w2-OH5,2.5; w2-OH6,2.6; w2-OH7,2.7; w2-OH8,2.8; w2-OH9,2.9; w2-OH10,2.11]));%

HB2a=sortrows(HB2);

HB2real=HB2a(1:(4-double(ismember(12,HB1real(:,2)))),:);

w3d=(abs([w3-w1 w3-w2 w3-w4 w3-w5 w3-w6 w3-OH1 w3-OH2 w3-OH3 w3-OH4 w3-OH5 w3-OH6 w3-OH7 w3-OH8 w3-OH9 w3-OH10]));

HB3=(abs([w3-w4,34; w3-w5,35; w3-w6,36; w3-OH1,3.1; w3-OH2,3.2; w3-OH3,3.3; w3-OH4,3.4; w3-OH5,3.5; w3-OH6,3.6; w3-OH7,3.7; w3-OH8,3.8; w3-OH9,3.9; w3-OH10,3.11]));%

HB3a=sortrows(HB3);

HB3real=HB3a(1:(4-double(ismember(23,HB2real(:,2)))-double(ismember(13,HB1real(:,2)))),:);

w4d=(abs([w4-w1 w4-w2 w4-w3 w4-w5 w4-w6 w4-OH1 w4-OH2 w4-OH3 w4-OH4 w4-OH5 w4-OH6 w4-OH7 w4-OH8 w4-OH9 w4-OH10]));

HB4=(abs([w4-w5,45; w4-w6,46; w4-OH1,4.1; w4-OH2,4.2; w4-OH3,4.3; w4-OH4,4.4; w4-OH5,4.5; w4-OH6,4.6; w4-OH7,4.7; w4-OH8,4.8; w4-OH9,4.9; w4-OH10,4.11]));%

HB4a=sortrows(HB4);

HB4real=HB4a(1:(4-double(ismember(34,HB3real(:,2)))-double(ismember(24,HB2real(:,2)))-double(ismember(14,HB1real(:,2)))),:);

w5d=(abs([w5-w1 w5-w2 w5-w3 w5-w4 w5-w6 w5-OH1 w5-OH2 w5-OH3 w5-OH4 w5-OH5 w5-OH6 w5-OH7 w5-OH8 w5-OH9 w5-OH10]));

HB5=(abs([w5-w6,56; w5-OH1,5.1; w5-OH2,5.2; w5-OH3,5.3; w5-OH4,5.4; w5-OH5,5.5; w5-OH6,5.6; w5-OH7,5.7; w5-OH8,5.8; w5-OH9,5.9; w5-OH10,5.11]));%

HB5a=sortrows(HB5);

HB5real=HB5a(1:(4-double(ismember(45,HB4real(:,2)))-double(ismember(35,HB3real(:,2)))-double(ismember(25,HB2real(:,2)))-double(ismember(15,HB1real(:,2)))),:);

w6d=(abs([w6-w1 w6-w2 w6-w3 w6-w4 w6-w5 w6-OH1 w6-OH2 w6-OH3 w6-OH4 w6-OH5 w6-OH6 w6-OH7 w6-OH8 w6-OH9 w6-OH10]));

HB6=(abs([w6-OH1,6.1; w6-OH2,6.2; w6-

```
OH3,6.3; w6-OH4,6.4; w6-OH5,6.5; w6-OH6,6.6; w6-OH7,6.7; w6-OH8,6.8; w6-OH9,6.9; w6-OH10,6.11]));%
                                                    HB6a=sortrows(HB6);
                                                    HB6real=HB6a(1:(4-
double(ismember(56,HB5real(:,2)))-double(ismember(46,HB4real(:,2)))-
double(ismember(36,HB3real(:,2)))-double(ismember(26,HB2real(:,2)))-
double(ismember(16,HB1real(:,2)))),:);

                                                    %%%%%%%%%%%%this lines of code
solve the new issue
                                                    HBr=([w1d w2d(2:end) w3d(3:end)
w4d(4:end) w5d(5:end) w6d(6:end)]);

                                                    HBreal=[HB1real; HB2real; HB3real;
HB4real; HB5real; HB6real];
                                                    HBsave=HBreal;
                                                    %Ew1=sort(Ew_i(1:9));Ew2=sort(Ew_i(10:1
7));Ew3=sort(Ew_i(18:24));Ew4=sort(Ew_i(25:30));
                                                    %Ew=sum(Ew1(1:4)+Ew2(1:4)+Ew3(1:4)+E
w4(1:4));

                                                    Ew_j=(1-exp(re-HBreal(:,1))).^2-1;
                                                    Ew_i=(1-exp(re-HBr)).^2-1;

                                                    Ew=sum(Ew_j);
                                                    EwT=sum(Ew_i);
                                                    %%%%%%%%%%%%%%%%%%%%%%%%%%%%%%%%%%%%
                                                    %Ew=sum((1-exp(re-w1d)).^2)+sum((1-
exp(re-w2d(2:end))).^2)+sum((1-exp(re-w3d(3:end))).^2)+sum((1-exp(re-w4d(4:end))).^2);

                                                    if Ew<=E_min %&EwT<=ET_min
                                                    E_min=Ew;
                                                    ET_min=EwT;
                                                    wd1=[w1d; w2d; w3d; w4d; w5d; w6d];
                                                    water_min1=[w1 w2 w3 w4 w5 w6];
                                                    clear HBsave;
                                                    HBsave=HBreal;
                                                    end
                                                end
                                            end
```

```
                                        end
                                    end
                                end
                            end
                        end
                    end
                end
            end
        end
end

%std_min
E_min
ET_min
%%
figure;plot(real(OH1),imag(OH1),'ro')
hold on
plot(real(OH2),imag(OH2),'ro')
plot(OH3,'ro')
plot(OH4,'ro')
plot(OH5,'ro')
plot(real(OH6),imag(OH6),'ro')
plot(OH7,'ro')
plot(OH8,'ro')
plot(OH9,'ro')
plot(real(OH10),imag(OH10),'ro')
plot(real(water),imag(water),'bo')
%plot(real(water_min),imag(water_min),'g*')
plot(real(water_min1),imag(water_min1),'m*')
daspect([1 1 1])
```

Bibliography

1. Whitelam S, Jack RL. 2015. The Statistical Mechanics of Dynamic Pathways to Self-Assembly. *Annu. Rev. Phys. Chem.* 66(1):143–63

2. Schwartz DK. 2001. Mechanisms and kinetics of self-assembled monolayer formation. *Annu. Rev. Phys. Chem.* 52(1):107–37

3. Whitesides GM. 2002. Self-Assembly at All Scales. *Science*. 295(5564):2418–21

4. Klug A. 1983. From Macromolecules to Biological Assemblies(Nobel Lecture). *Angew. Chemie Int. Ed. English*. 22(8):565–82

5. Hernández NE, Hansen WA, Zhu D, Shea ME, Khalid M, et al. 2019. Stimulus-responsive self-assembly of protein-based fractals by computational design. *Nat. Chem.* 11(7):605–14

6. Mallory SA, Valeriani C, Cacciuto A. 2018. An Active Approach to Colloidal Self-Assembly. *Annu. Rev. Phys. Chem.* 69(1):59–79

7. Boles MA, Engel M, Talapin D V. 2016. Self-assembly of colloidal nanocrystals: From intricate structures to functional materials. *Chem. Rev.* 116(18):11220–89

8. Herbst S, Soberats B, Leowanawat P, Stolte M, Lehmann M, Würthner F. 2018. Self-assembly of multi-stranded perylene dye J-aggregates in columnar liquid-crystalline phases. *Nat. Commun.* 9(1):2646

9. Love JC, Estroff LA, Kriebel JK, Nuzzo RG, Whitesides GM. 2005. Self-Assembled Monolayers of Thiolates on Metals as a Form of Nanotechnology. *Chem. Rev.* 105(4):1103–70

10. Van Rijn P, Tutus M, Kathrein C, Zhu L, Wessling M, et al. 2013. Challenges and advances in the field of self-assembled membranes. *Chem. Soc. Rev.* 42(16):6578–92

11. Chen IA, Walde P. 2010. From Self-Assembled Vesicles to Protocells. *Cold Spring Harb. Perspect. Biol.* 2(7):a002170–a002170

12. Zou Q, Liu K, Abbas M, Yan X. 2016. Peptide-Modulated Self-Assembly of Chromophores toward Biomimetic Light-Harvesting Nanoarchitectonics. *Adv. Mater.* 28(6):1031–43

13. Schmidt-Mende L. 2001. Self-Organized Discotic Liquid Crystals for High-Efficiency Organic Photovoltaics. *Science*. 293(5532):1119–22

14. Nelson J. 2001. SOLAR ENERGY: Solar Cells by Self-Assembly? *Science*. 293(5532):1059–60

15. Wang H, Gao T, Xiong W. 2017. Self-Phase-Stabilized Heterodyne Vibrational Sum Frequency Generation Microscopy. *ACS Photonics*. 4(7):1839–45

16. Han Y, Raghunathan V, Feng R, Maekawa H, Chung C-Y, et al. 2013. Mapping Molecular Orientation with Phase Sensitive Vibrationally Resonant Sum-Frequency Generation Microscopy. *J. Phys. Chem. B.* 117(20):6149–56

17. Santos GM, Baldelli S. 2013. Monitoring Localized Initial Atmospheric Corrosion of Alkanethiol-Covered Copper Using Sum Frequency Generation Imaging Microscopy: Relation between Monolayer Properties and Cu 2 O Formation. *J. Phys. Chem. C.* 117(34):17591–602

18. Makarem M, Sawada D, O'Neill HM, Lee CM, Kafle K, et al. 2017. Dependence of Sum Frequency Generation (SFG) Spectral Features on the Mesoscale Arrangement of SFG-Active Crystalline Domains Interspersed in SFG-Inactive Matrix: A Case Study with Cellulose in Uniaxially Aligned Control Samples and Alkali-Treated Seconda. *J. Phys. Chem. C.* 121(18):10249–57

19. Whitesides GM, Boncheva M. 2002. Beyond molecules: Self-assembly of mesoscopic and macroscopic components. *Proc. Natl. Acad. Sci. U. S. A.* 99(8):4769–74

20. Yang S, Yan Y, Huang J, Petukhov A V., Kroon-Batenburg LMJ, et al. 2017. Giant capsids from lattice self-assembly of cyclodextrin complexes. *Nat. Commun.* 8(1):15856

21. He WN, Xu JT. 2012. Crystallization assisted self-assembly of semicrystalline block copolymers. *Prog. Polym. Sci.* 37(10):1350–1400

22. Jiang L, Peng Y, Yan Y, Deng M, Wang Y, Huang J. 2010. "annular ring" microtubes formed by SDS@2β-CD complexes in aqueous solution. *Soft Matter*. 6(8):1731–36

23. Laaser JE, Xiong W, Zanni MT. 2011. Time-domain SFG spectroscopy using mid-IR pulse shaping: Practical and intrinsic advantages. *J. Phys. Chem. B.* 115(11):2536–46

24. Wang J, Clark ML, Li Y, Kaslan CL, Kubiak CP, Xiong W. 2015. Short-Range Catalyst-Surface Interactions Revealed by Heterodyne Two-Dimensional Sum Frequency Generation Spectroscopy.

J. Phys. Chem. Lett. 6(21):4204–9

25. Fang M, Baldelli S. 2017. Surface-Induced Heterogeneity Analysis of an Alkanethiol Monolayer on Microcrystalline Copper Surface Using Sum Frequency Generation Imaging Microscopy. *J. Phys. Chem. C.* 121(3):1591–1601

26. Fang M, Baldelli S. 2015. Grain structures and boundaries on microcrystalline copper covered with an octadecanethiol monolayer revealed by sum frequency generation microscopy. *J. Phys. Chem. Lett.* 6(8):1454–60

27. Cimatu K, Baldelli S. 2006. Sum Frequency Generation Microscopy of Microcontact-Printed Mixed Self-Assembled Monolayers. *J. Phys. Chem. B.* 110(4):1807–13

28. Cimatu K, Baldelli S. 2007. Spatially resolved surface analysis of an octadecanethiol self-assembled monolayer on mild steel using sum frequency generation imaging microscopy. *J. Phys. Chem. C.* 111(19):7137–43

29. Shah SA, Baldelli S. 2020. Chemical Imaging of Surfaces with Sum Frequency Generation Vibrational Spectroscopy. *Acc. Chem. Res.* 53(6):1139–50

30. Zheng D, Lu L, Kelly KF, Baldelli S. 2018. Chemical Imaging of Self-Assembled Monolayers on Copper Using Compressive Hyperspectral Sum Frequency Generation Microscopy. *J. Phys. Chem. B.* 122(2):464–71

31. Rich CC, Mattson MA, Krummel AT. 2016. Direct Measurement of the Absolute Orientation of N3 Dye at Gold and Titanium Dioxide Surfaces with Heterodyne-Detected Vibrational SFG Spectroscopy. *J. Phys. Chem. C.* 120(12):6601–11

32. Nihonyanagi S, Mondal JA, Yamaguchi S, Tahara T. 2013. Structure and Dynamics of Interfacial Water Studied by Heterodyne-Detected Vibrational Sum-Frequency Generation. *Annu. Rev. Phys. Chem.* 64(1):579–603

33. Deng GH, Qian Y, Wei Q, Zhang T, Rao Y. 2020. Interface-Specific Two-Dimensional Electronic Sum Frequency Generation Spectroscopy. *J. Phys. Chem. Lett.* 11(5):1738–45

34. Liu WT, Ron Shen Y. 2014. In situ sum-frequency vibrational spectroscopy of electrochemical interfaces with surface plasmon resonance. *Proc. Natl. Acad. Sci. U. S. A.* 111(4):1293–97

35. Huang S, Makarem M, Kiemle SN, Hamedi H, Sau M, et al. 2018. Inhomogeneity of Cellulose Microfibril Assembly in Plant Cell Walls Revealed with Sum Frequency Generation Microscopy. *J. Phys. Chem. B.* 122(19):5006–19

36. Kong L, Lee C, Kim SH, Ziegler GR. 2014. Characterization of Starch Polymorphic Structures Using Vibrational Sum Frequency Generation Spectroscopy. *J. Phys. Chem. B.* 118(7):1775–83

37. Lee CM, Chen X, Weiss PA, Jensen L, Kim SH. 2017. Quantum Mechanical Calculations of Vibrational Sum-Frequency-Generation (SFG) Spectra of Cellulose: Dependence of the CH and OH Peak Intensity on the Polarity of Cellulose Chains within the SFG Coherence Domain. *J. Phys. Chem. Lett.* 8(1):55–60

38. Lee CM, Kafle K, Park YB, Kim SH. 2014. Probing crystal structure and mesoscale assembly of cellulose microfibrils in plant cell walls, tunicate tests, and bacterial films using vibrational Sum Frequency Generation (SFG) spectroscopy. *Phys. Chem. Chem. Phys.* 16(22):10844–53

39. Wang H, Wagner JC, Chen W, Wang C, Xiong W. 2020. Spatially dependent H-bond dynamics at interfaces of water/biomimetic self-assembled lattice materials. *Proc. Natl. Acad. Sci.*, p. 202001861

40. Vickerman JC, Gilmore IS. 2009. *Surface Analysis– The Principal Techniques*. Chichester, UK: John Wiley & Sons, Ltd

41. Kärger J. 1995. Modern Techniques of Surface Science — Second Edition. *Zeitschrift für Phys. Chemie*. 189(Part_2):275–76

42. Ishiyama T, Morita A. 2017. Computational Analysis of Vibrational Sum Frequency Generation Spectroscopy. *Annu. Rev. Phys. Chem.* 68(1):355–77

43. Wang H-F, Velarde L, Gan W, Fu L. 2015. Quantitative Sum-Frequency Generation Vibrational Spectroscopy of Molecular Surfaces and Interfaces: Lineshape, Polarization, and Orientation SFG-VS: sum-frequency generation vibrational spectroscopy. *Annu. Rev. Phys. Chem.* 66:189–216

44. Wang HF, Gan W, Lu R, Rao Y, Wu BH. 2005. Quantitative spectral and orientational analysis in surface sum frequency generation vibrational spectroscopy (SFG-VS). *Int. Rev. Phys. Chem.* 24(2):191–256

45. Shen YR. 2013. Phase-Sensitive Sum-Frequency Spectroscopy. *Annu. Rev. Phys. Chem.* 64(1):129–50

46. Guyot-Sionnest P, Hunt JH, Shen YR. 1987. Sum-frequency vibrational spectroscopy of a Langmuir film: Study of molecular orientation of a two-dimensional system. *Phys. Rev. Lett.* 59(14):1597–1600

47. Zhu XD, Suhr H, Shen YR. 1987. Surface vibrational spectroscopy by infrared-visible sum frequency generation. *Phys. Rev. B.* 35(6):3047–50

48. Flörsheimer M, Brillert C, Fuchs H. 1999. Chemical Imaging of Interfaces by Sum Frequency Microscopy. *Langmuir*. 15(17):5437–39

49. Hoffmann DMP, Kuhnke K, Kern K. 2002. Sum-frequency generation microscope for opaque and reflecting samples. *Rev. Sci. Instrum.* 73(9):3221

50. Cai X, Hu B, Sun T, Kelly KF, Baldelli S. 2011. Sum frequency generation-compressive sensing microscope. *J. Chem. Phys.* 135(19):

51. Zheng D, Lu L, Li Y, Kelly KF, Baldelli S. 2016. Compressive Broad-Band Hyperspectral Sum Frequency Generation Microscopy to Study Functionalized Surfaces. *J. Phys. Chem. Lett.* 7(10):1781–87

52. Cimatu K, Baldelli S. 2006. Sum frequency generation imaging microscopy of CO on platinum. *J. Am. Chem. Soc.* 128(50):16016–17

53. Cimatu KA, Baldelli S. 2009. Chemical microscopy of surfaces by sum frequency generation imaging. *J. Phys. Chem. C*. 113(38):16575–88

54. Baldelli S. 2008. Chemical imaging of monolayers on metal surfaces: Applications in corrosion, catalysis, and self-assembled monolayers. *ChemPhysChem*. 9(16):2291–98

55. Flörsheimer M, Brillert C, Fuchs H. 1999. Chemical imaging of interfaces by sum frequency microscopy. *Langmuir*. 15(17):5437–39

56. Inoue K, Fujii M, Sakai M. 2010. Development of a non-scanning vibrational sum-frequency generation detected infrared super-resolution microscope and its application to biological cells. *Appl. Spectrosc.* 64(3):275–81

57. Lee CM, Kafle K, Huang S, Kim SH. 2016. Multimodal Broadband Vibrational Sum Frequency Generation (MM-BB-V-SFG) Spectrometer and Microscope. *J. Phys. Chem. B.* 120(1):102–16

58. Mizutani G, Koyama T, Tomizawa S, Sano H. 2005. Distinction between some saccharides in scattered optical sum frequency intensity images. *Spectrochim. Acta - Part A Mol. Biomol. Spectrosc.* 62(4–5):845–49

59. Yan ECY, Fu L, Wang Z, Liu W. 2014. Biological Macromolecules at Interfaces Probed by Chiral Vibrational Sum Frequency Generation Spectroscopy. *Chem. Rev.* 114(17):8471–98

60. Lambert AG, Davies PB, Neivandt DJ. 2005. Implementing the theory of sum frequency generation vibrational spectroscopy: A tutorial review. *Appl. Spectrosc. Rev.* 40(2):103–45

61. Han Y, Hsu J, Ge N, Potma EO. 2015. Polarization-Sensitive Sum-Frequency Generation Microscopy of Collagen Fibers. *J. Phys. Chem. B.* 119(8):3356–65

62. Hieu HC, Tuan NA, Li H, Miyauchi Y, Mizutani G. 2011. Sum frequency generation microscopy study of cellulose fibers. *Appl. Spectrosc.* 65(11):1254–59

63. Mingabudinova LR, Vinogradov V V., Milichko VA, Hey-Hawkins E, Vinogradov A V. 2016. Metal-organic frameworks as competitive materials for non-linear optics. *Chem. Soc. Rev.* 45(19):5408–31

64. Chen Z, Gallo G, Sawant VA, Zhang T, Zhu M, et al. 2020. Giant Enhancement of Second Harmonic Generation Accompanied by the Structural Transformation of 7-Fold to 8-Fold Interpenetrated Metal–Organic Frameworks (MOFs). *Angew. Chemie Int. Ed.* 59(2):833–38

65. Hirose C, Akamatsu N, Domen K. 1992. Formulas for the Analysis of the Surface SFG Spectrum and Transformation Coefficients of Cartesian SFG Tensor Components. *Appl. Spectrosc.* 46(6):1051–72

66. Moad AJ, Simpson GJ. 2004. A unified treatment of selection rules and symmetry relations for sum-frequency and second harmonic spectroscopies. *J. Phys. Chem. B.* 108(11):3548–62

67. Li Z, Wang J, Li Y, Xiong W. 2016. Solving the “magic angle” challenge in determining molecular orientation heterogeneity at interfaces. *J. Phys. Chem. C.* 120(36):20239–46

68. Tian CS, Shen YR. 2009. Structure and charging of hydrophobic material/water interfaces studied by phase-sensitive sum-frequency vibrational spectroscopy. *Proc. Natl. Acad. Sci.* 106(36):15148–53

69. Stiopkin I V., Jayathilake HD, Bordenyuk AN, Benderskii A V. 2008. Heterodyne-Detected Vibrational Sum Frequency Generation Spectroscopy. *J. Am. Chem. Soc.* 130(7):2271–75

70. Xiong W, Laaser JE, Mehlenbacher RD, Zanni MT. 2011. Adding a dimension to the infrared spectra of interfaces using heterodyne detected 2D sum-frequency generation (HD 2D SFG) spectroscopy. *Proc. Natl. Acad. Sci.* 108(52):20902–7

71. Vanselous H, Petersen PB. 2016. Extending the Capabilities of Heterodyne-Detected Sum-Frequency Generation Spectroscopy: Probing Any Interface in Any Polarization Combination. *J. Phys. Chem. C.* 120(15):8175–84

72. Xu B, Wu Y, Sun D, Dai H-L, Rao Y. 2015. Stabilized phase detection of heterodyne sum frequency generation for interfacial studies. *Opt. Lett.* 40(19):4472–75

73. Hosseinpour S, Tang F, Wang F, Livingstone RA, Schlegel SJ, et al. 2017. Chemisorbed and Physisorbed Water at the TiO2/Water Interface. *J. Phys. Chem. Lett.* 8(10):2195–99

74. Chen X, Hua W, Huang Z, Allen HC. 2010. Interfacial water structure associated with phospholipid membranes studied by phase-sensitive vibrational sum frequency generation spectroscopy. *J. Am. Chem. Soc.* 132(32):11336–42

75. Nihonyanagi S, Yamaguchi S, Tahara T. 2017. Ultrafast Dynamics at Water Interfaces Studied by Vibrational Sum Frequency Generation Spectroscopy. *Chem. Rev.* 117(16):10665–93

76. Bonn M, Nagata Y, Backus EHG. 2015. Molecular Structure and Dynamics of Water at the Water-Air Interface Studied with Surface-Specific Vibrational Spectroscopy. *Angew. Chemie Int. Ed.* 54(19):5560–76

77. Dickson RM, Norris DJ, Tzeng Y-L, Moerner WE. 1996. Three-Dimensional Imaging of Single Molecules Solvated in Pores of Poly(acrylamide) Gels. *Science*. 274(5289):966–68

78. Lu HP, Xun L, Xie XS. 1998. Single-Molecule Enzymatic Dynamics. *Science*. 282(5395):1877–82

79. Peterman EJG, Sosa H, Moerner WE. 2004. Single-Molecule Fluorescence Spectroscopy and Microscopy of Biomolecular Motors. *Annu. Rev. Phys. Chem.* 55(1):79–96

80. Pavani SRP, Thompson MA, Biteen JS, Lord SJ, Liu NN, et al. 2009. Three-dimensional, single-molecule fluorescence imaging beyond the diffraction limit by using a double-helix point spread function. *Proc. Natl. Acad. Sci.* 106(9):2995–99

81. Huang B, Bates M, Zhuang X. 2009. Super-Resolution Fluorescence Microscopy. *Annu. Rev. Biochem.* 78(1):993–1016

82. Klar TA, Hell SW. 1999. Subdiffraction resolution in far-field fluorescence microscopy. *Opt. Lett.* 24(14):954

83. Betzig E, Patterson GH, Sougrat R, Lindwasser OW, Olenych S, et al. 2006. Imaging intracellular fluorescent proteins at nanometer resolution. *Science*. 313(5793):1642–45

84. Wampler RD, Kissick DJ, Dehen CJ, Gualtieri EJ, Grey JL, et al. 2008. Selective detection of protein crystals by second harmonic microscopy. *J. Am. Chem. Soc.* 130(43):14076–77

85. Wan Y, McDole K, Keller PJ. 2019. Light-Sheet Microscopy and Its Potential for Understanding Developmental Processes. *Annu. Rev. Cell Dev. Biol.* 35(1):655–81

86. Lew MD, Lee SF, Ptacin JL, Lee MK, Twieg RJ, et al. 2011. Three-dimensional superresolution colocalization of intracellular protein superstructures and the cell surface in live Caulobacter crescentus. *Proc. Natl. Acad. Sci.* 108(46):E1102–10

87. Wang W, Shen H, Shuang B, Hoener BS, Tauzin LJ, et al. 2016. Super Temporal-Resolved Microscopy (STReM). *J. Phys. Chem. Lett.* 7(22):4524–29

88. Snaider JM, Guo Z, Wang T, Yang M, Yuan L, et al. 2018. Ultrafast Imaging of Carrier Transport across Grain Boundaries in Hybrid Perovskite Thin Films. *ACS Energy Lett.* 3(6):1402–8

89. Wong CY, Penwell SB, Cotts BL, Noriega R, Wu H, Ginsberg NS. 2013. Revealing Exciton Dynamics in a Small-Molecule Organic Semiconducting Film with Subdomain Transient Absorption Microscopy. *J. Phys. Chem. C.* 117(42):22111–22

90. Gabriel MM, Kirschbrown JR, Christesen JD, Pinion CW, Zigler DF, et al. 2013. Direct Imaging of Free Carrier and Trap Carrier Motion in Silicon Nanowires by Spatially-Separated Femtosecond Pump–Probe Microscopy. *Nano Lett.* 13(3):1336–40

91. Silva WR, Graefe CT, Frontiera RR. 2016. Toward Label-Free Super-Resolution Microscopy. *ACS Photonics*. 3(1):79–86

92. Nihonyanagi S, Yamaguchi S, Tahara T. 2009. Direct evidence for orientational flip-flop of water molecules at charged interfaces: A heterodyne-detected vibrational sum frequency generation study. *J. Chem. Phys.* 130(20):204704

93. Denk W, Strickler J, Webb W. 1990. Two-photon laser scanning fluorescence microscopy. *Science*. 248(4951):73–76

94. Humbert B, Grausem J, Burneau A, Spajer M, Tadjeddine A. 2001. Step towards sum frequency generation spectromicroscopy at a submicronic spatial resolution. *Appl. Phys. Lett.* 78(1):135–37

95. Raghunathan V, Han Y, Korth O, Ge N-H, Potma EO. 2011. Rapid vibrational imaging with sum frequency generation microscopy. *Opt. Lett.* 36(19):3891

96. Shen Y, Swiatkiewicz J, Winiarz J, Markowicz P, Prasad PN. 2000. Second-harmonic and sum-frequency imaging of organic nanocrystals with photon scanning tunneling microscope. *Appl. Phys. Lett.* 77(19):2946–48

97. Ji N, Zhang K, Yang H, Shen YR. 2006. Three-dimensional chiral imaging by sum-frequency generation. *J. Am. Chem. Soc.* 128(11):3482–83

98. Schaller RD, Saykally RJ. 2001. Near-field infrared sum-frequency generation imaging of chemical vapor deposited zinc selenide. *Langmuir*. 17(7):2055–58

99. Hoffmann DMP, Kuhnke K, Kern K. 2002. Sum-frequency generation microscope for opaque and reflecting samples. *Rev. Sci. Instrum.* 73(9):3221–26

100. Fu L, Wang Z, Psciuk BT, Xiao D, Batista VS, Yan ECY. 2015. Characterization of Parallel β-Sheets at Interfaces by Chiral Sum Frequency Generation Spectroscopy. *J. Phys. Chem. Lett.* 6(8):1310–15

101. Buchbinder AM, Weitz E, Geiger FM. 2010. When the Solute Becomes the Solvent: Orientation, Ordering, and Structure of Binary Mixtures of 1-Hexanol and Cyclohexane over the (0001) α-Al 2 O 3 Surface. *J. Am. Chem. Soc.* 132(41):14661–68

102. Curtis AD, Reynolds SB, Calchera AR, Patterson JE. 2010. Understanding the role of nonresonant sum-frequency generation from polystyrene thin films. *J. Phys. Chem. Lett.* 1(16):2435–39

103. Liu AA, Liu S, Zhang R, Ren Z. 2015. Spectral Identification of Methanol on TiO2(110) Surfaces with Sum Frequency Generation in the C-H Stretching Region. *J. Phys. Chem. C*. 119(41):23486–94

104. Lee E. 2012. *Raman Imaging*, Vol. 168. Berlin, Heidelberg: Springer Berlin Heidelberg. 13 pp.

105. Jiang L, Peng Y, Yan Y, Deng M, Wang Y, Huang J. 2010. “Annular Ring” microtubes formed by SDS@2β-CD complexes in aqueous solution. *Soft Matter*. 6(8):1731–36

106. Jiang L, de Folter JWJ, Huang J, Philipse AP, Kegel WK, Petukhov A V. 2013. Helical Colloidal Sphere Structures through Thermo-Reversible Co-Assembly with Molecular Microtubes. *Angew. Chemie Int. Ed.* 52(12):3364–68

107. Brocos P, Díaz-Vergara N, Banquy X, Pérez-Casas S, Costas M, Piñeiro A. 2010. Similarities and Differences Between Cyclodextrin−Sodium Dodecyl Sulfate Host−Guest Complexes of Different Stoichiometries: Molecular Dynamics Simulations at Several Temperatures. *J. Phys. Chem. B.* 114(39):12455–67

108. Ostroverkhov V, Waychunas GA, Shen YR. 2005. New information on water interfacial structure revealed by phase-sensitive surface spectroscopy. *Phys. Rev. Lett.* 94(4):2–5

109. Vazirani U, Papadimitriou C, Dasgupta S. 2006. *Algorithms*. McGraw-Hill Education

110. Tyrode E, Hedberg J. 2012. A Comparative Study of the CD and CH Stretching Spectral Regions

of Typical Surfactants Systems Using VSFS: Orientation Analysis of the Terminal CH 3 and CD 3 Groups. *J. Phys. Chem. C.* 116(1):1080–91

111. Kouyama W, Nishida T, Thu Hien KT, Mizutani G, Hasegawa H, Miyamura H. 2016. Optical Sum Frequency Generation Spectroscopy of Cracked Non-Glutinous Rice (<i>Oryza sativa</i> L.) Kernels. *J. Biomater. Nanobiotechnol.* 07(01):13–18

112. Gaussian 16, Revision A.03, M. J. Frisch, G. W. Trucks, H. B. Schlegel, G. E. Scuseria, M. A. Robb, J. R. Cheeseman, G. Scalmani, V. Barone, G. A. Petersson, H. Nakatsuji, X. Li, M. Caricato, A. V. Marenich, J. Bloino, B. G. Janesko, R. Gomperts, B. Mennu WC. 2016. Gaussian 16. *Gaussian, Inc. Wallingford CT,*

113. Tang CY, Huang Z, Allen HC. 2011. Interfacial water structure and effects of Mg2+ and Ca 2+ binding to the COOH headgroup of a palmitic acid monolayer studied by sum frequency spectroscopy. *J. Phys. Chem. B.* 115(1):34–40

114. Ebben CJ, Ault AP, Ruppel MJ, Ryder OS, Bertram TH, et al. 2013. Size-Resolved Sea Spray Aerosol Particles Studied by Vibrational Sum Frequency Generation. *J. Phys. Chem. A.* 117(30):6589–6601

115. Ai X, Beard MC, Knutsen KP, Shaheen SE, Rumbles G, Ellingson RJ. 2006. Photoinduced Charge Carrier Generation in a Poly(3-hexylthiophene) and Methanofullerene Bulk Heterojunction Investigated by Time-Resolved Terahertz Spectroscopy. *J. Phys. Chem. B.* 110(50):25462–71

116. Nguyen KT, King JT, Chen Z. 2010. Orientation Determination of Interfacial β-Sheet Structures in Situ. *J. Phys. Chem. B.* 114(25):8291–8300

117. Alayoglu S, Krier JM, Michalak WD, Zhu Z, Gross E, Somorjai GA. 2012. In situ surface and reaction probe studies with model nanoparticle catalysts. *ACS Catal.* 2(11):2250–58

118. Sagle LB, Cimatu K, Litosh VA, Liu Y, Flores SC, et al. 2011. Methyl groups of trimethylamine N-oxide orient away from hydrophobic interfaces. *J. Am. Chem. Soc.* 133(46):18707–12

119. Gordon BP, Moore FG, Scatena LF, Valley NA, Wren SN, Richmond GL. 2018. Model Behavior: Characterization of Hydroxyacetone at the Air-Water Interface Using Experimental and Computational Vibrational Sum Frequency Spectroscopy. *J. Phys. Chem. A.* 122(15):3837–49

120. Shen YR. 1989. Surface properties probed by second-harmonic and sum-frequency generation. *Nature*. 337(6207):519–25

121. Brocos P, Díaz-Vergara N, Banquy X, Pérez-Casas S, Costas M, Piñeiro Á. 2010. Similarities and

differences between cyclodextrin-sodium dodecyl sulfate host-guest complexes of different stoichiometries: Molecular dynamics simulations at several temperatures. *J. Phys. Chem. B.* 114(39):12455–67

122. Simpson G. 2017. *Nonlinear Optical Polarization Analysis in Chemistry and Biology*. New York: Cambridge University Press

123. Gavira JM, Hernanz A, Bratu I. 2003. Dehydration of β-cyclodextrin: An IR ν(OH) band profile analysis. *Vib. Spectrosc.* 32(2):137–46

124. Lee CM, Kubicki JD, Fan B, Zhong L, Jarvis MC, Kim SH. 2015. Hydrogen-Bonding Network and OH Stretch Vibration of Cellulose: Comparison of Computational Modeling with Polarized IR and SFG Spectra. *J. Phys. Chem. B.* 119(49):15138–49

125. McDermott ML, Vanselous H, Corcelli SA, Petersen PB. 2017. DNA's Chiral Spine of Hydration. *ACS Cent. Sci.* 3(7):708–14

126. Fenn EE, Wong DB, Giammanco CH, Fayer MD. 2011. Dynamics of water at the interface in reverse micelles: Measurements of spectral diffusion with two-dimensional infrared vibrational echoes. *J. Phys. Chem. B.* 115(40):11658–70

127. Abel S, Galamba N, Karakas E, Marchi M, Thompson WH, Laage D. 2016. On the Structural and Dynamical Properties of DOPC Reverse Micelles. *Langmuir*. 32(41):10610–20

128. Bakulin AA, Cringus D, Pieniazek PA, Skinner JL, Jansen TLC, Pshenichnikov MS. 2013. Dynamics of water confined in reversed micelles: Multidimensional vibrational spectroscopy study. *J. Phys. Chem. B.* 117(49):15545–58

129. Ramakrishnan G, González-Jiménez M, Lapthorn AJ, Wynne K. 2017. Spectrum of Slow and Super-Slow (Picosecond to Nanosecond) Water Dynamics around Organic and Biological Solutes. *J. Phys. Chem. Lett.* 8(13):2964–70

130. Cremer PS, Flood AH, Gibb BC, Mobley DL. 2017. Collaborative routes to clarifying the murky waters of aqueous supramolecular chemistry. *Nat. Chem.* 10(1):8–16

131. Nam KT, Shelby SA, Choi PH, Marciel AB, Chen R, et al. 2010. Free-floating ultrathin two-dimensional crystals from sequence-specific peptoid polymers. *Nat. Mater.* 9(5):454–60

132. Valéry C, Paternostre M, Robert B, Gulik-Krzywicki T, Narayanan T, et al. 2003. Biomimetic organization: Octapeptide self-assembly into nanotubes of viral capsid-like dimension. *Proc. Natl. Acad. Sci. U. S. A.* 100(18):10258–62

133. Aliprandi A, Mauro M, De Cola L. 2016. Controlling and imaging biomimetic self-assembly. *Nat. Chem.* 8(1):10–15

134. Wu C, Xie Q, Xu W, Tu M, Jiang L. 2019. Lattice self-assembly of cyclodextrin complexes and beyond. *Curr. Opin. Colloid Interface Sci.* 39:76–85

135. Clarke S. 1981. The hydrophobic effect: Formation of micelles and biological membranes, 2nd edition (Tanford, Charles). *J. Chem. Educ.* 58(8):A246

136. Discher DE. 2002. Polymer Vesicles. *Science*. 297(5583):967–73

137. Nikolic MS, Olsson C, Saldier A, Kornowski A, Rank A, et al. 2009. Micelle and vesicle formation of amphiphilic nanopartieles. *Angew. Chemie - Int. Ed.* 48(15):2752–54

138. Dubois M, Demé B, Gulik-Krzywicki T, Dedieu JC, Vautrin C, et al. 2001. Self-assembly of regular hollow icosahedra in salt-free catanionic solutions. *Nature*. 411(6838):672–75

139. Dubois M, Lizunov V, Meister A, Gulik-Krzywicki T, Verbavatz JM, et al. 2004. Shape control through molecular segregation in giant surfactant aggregates. *Proc. Natl. Acad. Sci. U. S. A.* 101(42):15082–87

140. Jiang L, Peng Y, Yan Y, Huang J. 2011. Aqueous self-assembly of SDS@2β-CD complexes: Lamellae and vesicles. *Soft Matter*. 7(5):1726–31

141. Wikström M, Verkhovsky MI, Hummer G. 2003. Water-gated mechanism of proton translocation by cytochrome c oxidase. *Biochim. Biophys. Acta - Bioenerg.* 1604(2):61–65

142. Levy Y, Onuchic JN. 2006. Water Mediation in Protein Folding and Molecular Recognition. *Annu. Rev. Biophys. Biomol. Struct.* 35(1):389–415

143. Cordier P, Tournilhac F, Soulié-Ziakovic C, Leibler L. 2008. Self-healing and thermoreversible rubber from supramolecular assembly. *Nature*. 451(7181):977–80

144. Liu F, Dong BQ, Liu XH, Zheng YM, Zi J. 2009. Structural color change in longhorn beetles Tmesisternus isabellae. *Opt. Express*. 17(18):16183

145. Zhou C, Cheng X, Yan Y, Wang J, Huang J. 2014. Reversible transition between SDS@2β-CD microtubes and vesicles triggered by temperature. *Langmuir*. 30(12):3381–86

146. Wang H, Chen W, Wagner JC, Xiong W. 2019. Local Ordering of Lattice Self-Assembled SDS@2β-CD Materials and Adsorbed Water Revealed by Vibrational Sum Frequency Generation

Microscope. *J. Phys. Chem. B.* 123(29):6212–21

147. Abel S, Galamba N, Karakas E, Marchi M, Thompson WH, Laage D. 2016. On the Structural and Dynamical Properties of DOPC Reverse Micelles. *Langmuir*. 32(41):10610–20

148. Bakulin AA, Cringus D, Pieniazek PA, Skinner JL, Jansen TLC, Pshenichnikov MS. 2013. Dynamics of water confined in reversed micelles: Multidimensional vibrational spectroscopy study. *J. Phys. Chem. B.* 117(49):15545–58

149. Perets EA, Yan ECY. 2019. Chiral Water Superstructures around Antiparallel β-Sheets Observed by Chiral Vibrational Sum Frequency Generation Spectroscopy. *J. Phys. Chem. Lett.* 10(12):3395–3401

150. Khuntawee W, Karttunen M, Wong-Ekkabut J. 2017. A molecular dynamics study of conformations of beta-cyclodextrin and its eight derivatives in four different solvents. *Phys. Chem. Chem. Phys.* 19(35):24219–29

151. Makedonopoulou S, Mavridis IM. 2000. Structure of the inclusion complex of β-cyclodextrin with 1,12-dodecanedioic acid using synchrotron radiation data; a detailed dimeric β-cyclodextrin structure. *Acta Crystallogr. Sect. B Struct. Sci.* 56(2):322–31

152. Giastas P, Yannakopoulou K, Mavridis IM. 2003. Molecular structures of the inclusion complexes β-cyclodextrin-1,2- bis(4-aminophenyl)ethane and β-cyclodextrin-4,4′-diaminobiphenyl; packing of dimeric β-cyclodextrin inclusion complexes. *Acta Crystallogr. Sect. B Struct. Sci.* 59(2):287–99

153. Pop MM, Goubitz K, Borodi G, Bogdan M, De Ridder DJA, et al. 2002. Crystal structure of the inclusion complex of β-cyclodextrin with mefenamic acid from high-resolution synchrotron powder-diffraction data in combination with molecular-mechanics calculations. *Acta Crystallogr. Sect. B Struct. Sci.* 58(6):1036–43

154. Aree T, Schulz B, Reck G. 2003. Crystal structures of β-cyclodextrin complexes with formic acid and acetic acid. *J. Incl. Phenom.* 47(1–2):39–45

155. Aree T, Chaichit N. 2003. Crystal structure of β-cyclodextrin-benzoic acid inclusion complex. *Carbohydr. Res.* 338(5):439–46

156. Fu Y, Wang H, Shi R, Cheng JX. 2007. Second harmonic and sum frequency generation imaging of fibrous astroglial filaments in ex vivo spinal tissues. *Biophys. J.* 92(9):3251–59

157. Tuladhar A, Dewan S, Kubicki JD, Borguet E. 2016. Spectroscopy and Ultrafast Vibrational Dynamics of Strongly Hydrogen Bonded OH Species at the α-Al2O3(112-0)/H2O Interface. *J. Phys.*

Chem. C. 120(29):16153–61

158. McGuire JA. 2006. Ultrafast Vibrational Dynamics at Water Interfaces. *Science*. 313(5795):1945–48

159. Livingstone RA, Nagata Y, Bonn M, Backus EHG. 2015. Two Types of Water at the Water-Surfactant Interface Revealed by Time-Resolved Vibrational Spectroscopy. *J. Am. Chem. Soc.* 137(47):14912–19

160. Zhang Z, Piatkowski L, Bakker HJ, Bonn M. 2011. Ultrafast vibrational energy transfer at the water/air interface revealed by two-dimensional surface vibrational spectroscopy. *Nat. Chem.* 3(11):888–93

161. Bonn M, Bakker HJ, Ghosh A, Yamamoto S, Sovago M, Campen RK. 2010. Structural inhomogeneity of interfacial water at lipid monolayers revealed by surface-specific vibrational pump-probe spectroscopy. *J. Am. Chem. Soc.* 132(42):14971–78

162. Woutersen S, Bakker HJ. 1999. Resonant intermolecular transfer of vibrational energy in liquid water. *Nature*. 402(6761):507–9

163. Timmer RLA, Bakker HJ. 2010. Vibrational förster transfer in ice ih. *J. Phys. Chem. A.* 114(12):4148–55

164. Ghosh A, Smits M, Bredenbeck J, Dijkhuizen N, Bonn M. 2008. Femtosecond time-resolved and two-dimensional vibrational sum frequency spectroscopic instrumentation to study structural dynamics at interfaces. *Rev. Sci. Instrum.* 79(9):

165. Van Der Post ST, Hsieh CS, Okuno M, Nagata Y, Bakker HJ, et al. 2015. Strong frequency dependence of vibrational relaxation in bulk and surface water reveals sub-picosecond structural heterogeneity. *Nat. Commun.* 6(May):1–7

166. Saenger W, Jacob J, Gessler K, Steiner T, Hoffmann D, et al. 1998. Structures of the common cyclodextrins and their larger analogues - beyond the doughnut. *Chem. Rev.* 98(5):1787–1802

167. Bonn M, Bakker HJ, Ghosh A, Yamamoto S, Sovago M, Campen RK. 2010. Structural inhomogeneity of interfacial water at lipid monolayers revealed by surface-specific vibrational pump-probe spectroscopy. *J. Am. Chem. Soc.* 132(42):14971–78

168. Stiopkin I V., Weeraman C, Pieniazek PA, Shalhout FY, Skinner JL, Benderskii A V. 2011. Hydrogen bonding at the water surface revealed by isotopic dilution spectroscopy. *Nature*. 474(7350):192–95

169. Lawrence CP, Skinner JL. 2003. Vibrational spectroscopy of HOD in liquid D2O. III. Spectral diffusion, and hydrogen-bonding and rotational dynamics. *J. Chem. Phys.* 118(1):264–72

170. Staib A, Hynes JT. 1993. Vibrational predissociation in hydrogen-bonded OH...O complexes via OH stretch-OO stretch energy transfer. *Chem. Phys. Lett.* 204(1–2):197–205

171. Fecko CJ. 2003. Ultrafast Hydrogen-Bond Dynamics in the Infrared Spectroscopy of Water. *Science*. 301(5640):1698–1702

172. Sofronov OO, Bakker HJ. 2019. Vibrational Relaxation Dynamics of the Core and Outer Part of Proton-Hydration Clusters. *J. Phys. Chem. B.* 123(29):6222–28

173. Piatkowski L, Eisenthal KB, Bakker HJ. 2009. Ultrafast intermolecular energy transfer in heavy water. *Phys. Chem. Chem. Phys.* 11(40):9033–38

174. Kang YK. 2000. Which functional form is appropriate for hydrogen bond of amides? *J. Phys. Chem. B.* 104(34):8321–26

175. Bruni F, Di Mino C, Imberti S, McLain SE, Rhys NH, Ricci MA. 2018. Hydrogen Bond Length as a Key to Understanding Sweetness. *J. Phys. Chem. Lett.* 9(13):3667–72

176. Cyran JD, Backus EHG, Nagata Y, Bonn M. 2018. Structure from Dynamics: Vibrational Dynamics of Interfacial Water as a Probe of Aqueous Heterogeneity. *J. Phys. Chem. B.* 122(14):3667–79

177. Nibbering ETJ, Elsaesser T. 2004. Ultrafast Vibrational Dynamics of Hydrogen Bonds in the Condensed Phase. *Chem. Rev.* 104(4):1887–1914

178. Fenn EE, Moilanen DE, Levinger NE, Fayer MD. 2009. Water dynamics and interactions in water-polyether binary mixtures. *J. Am. Chem. Soc.* 131(15):5530–39

179. Moilanen DE, Piletic IR, Fayer MD. 2007. Water dynamics in nafion fuel cell membranes: The effects of confinement and structural changes on the hydrogen bond network. *J. Phys. Chem. C.* 111(25):8884–91

180. Yan C, Kramer PL, Yuan R, Fayer MD. 2018. Water Dynamics in Polyacrylamide Hydrogels. *J. Am. Chem. Soc.* 140(30):9466–77

181. Kramer PL, Giammanco CH, Fayer MD. 2015. Dynamics of water, methanol, and ethanol in a room temperature ionic liquid. *J. Chem. Phys.* 142(21):

182. Park S, Fayer MD. 2007. Hydrogen bond dynamics in aqueous NaBr solutions. *Proc. Natl. Acad. Sci. U. S. A.* 104(43):16731–38

183. Bamford CH, Tipper CFH, Compton RG. 1985. Chapter 5 Rotational Diffusion Effects. In *Comprehensive Chemical Kinetics*. 25(C):105–17

184. Nelson DD, Schiffman A, Nesbitt DJ. 1989. The dipole moment function and vibrational transition intensities of OH. *J. Chem. Phys.* 90(10):5455–65

185. Kjaergaard HG, Howard DL, Schofield DP, Robinson TW, Ishiuchi SI, Fujii M. 2002. OH- and CH-stretching overtone spectra of catechol. *J. Phys. Chem. A.* 106(2):258–66

186. Ghosh PN, Deo MN, Kawaguchi K. 1999. Vibrational Transition Moment of the CH Radical Determined from the Herman-Wallis Effect. *Astrophys. J.* 525(1):539–42

187. Smits M, Ghosh A, Bredenbeck J, Yamamoto S, Müller M, Bonn M. 2007. Ultrafast energy flow in model biological membranes. *New J. Phys.* 9:0–20

188. Bredenbeck J, Ghosh A, Smits M, Bonn M. 2008. Ultrafast two dimensional-infrared spectroscopy of a molecular monolayer. *J. Am. Chem. Soc.* 130(7):2152–53

189. Shim S-H, Strasfeld DB, Fulmer EC, Zanni MT. 2006. Femtosecond pulse shaping directly in the mid-IR using acousto-optic modulation. *Opt. Lett.* 31(6):838–40